PEELING STRUCTURED SURFACES IN VISCOUS ENVIRONMENTS:

THE ROLE OF DEFORMATION AND DRAINAGE CHANNELS

by

Charles Dhong

A dissertation submitted to The Johns Hopkins University in conformity with the requirements for the degree of Doctor of Philosophy

Baltimore, Maryland
October 2016

Abstract

Tree frogs exhibit remarkable adhesion in completely flooded environments without the aid of chemical adhesives, interlocking supports, or capillary forces. This ability has been attributed to the specialized structures on their toe pads, which consist of a hexagonal array of hierarchical structures. The arrangement of these structures form drainage channels that aid in removing the fluid between the toe pad and surface to make rapid and reversible contact. While it has been shown that many animals, such as geckos, take advantage of patterned toe pads to enhance adhesion in dry and wet environments, less is known about how the drainage channels on the tree frog's toe pads are able to modulate its adhesion in completely flooded environments. These insights could be relevant to many natural and industrial processes including hydrofracture, micro-contact printing, self-assembly and soft robotics.

In addition to these structured surfaces, 1) their toe pads are highly deformable, 2) they approach a surface in the normal direction, but detach in a peeling mode, and 3) their toe pads are subject to both viscous forces and van der Waals interactions once in contact. To investigate this coupled phenomenon, we created a custom-made peeling apparatus to mimic the tree frog toe pad by using micro-patterned flexible plates (e.g. glass coverslips). We systematically deconstruct these coupled mechanisms by altering our samples or the fluid bath. By building the complexity methodically, we maintain a link between each new investigation and the results of the preceding study.

First, we chose materials that minimize van der Waals forces to isolate the coupling between the mechanical properties of unpatterned plates (the Young's modulus and the rigidity) and the viscous forces. We developed scaling arguments that explain how the peak force and work needed to separate the plate scale with the viscosity and rigidity. We also explain why deformable samples will further reduce the viscous forces compared to samples of the same rigidity.

We then micro-fabricated rigid structures on these plates that do not alter the bulk mechanical properties of the plates, but create drainage channels that alter their approach and detachment from a bottom surface. We have found that structured surfaces reduced forces compared to flat samples, but only in regimes where the fluid can enter channels. We are able to correlate these regimes to the structure geometry.

Finally, we fabricated the same structures out of a more deformable material which reduced the viscous forces further than their rigid counterparts. We attribute this reduction to the fluid flow around the pillars, as opposed to a mechanical response from the plate. Then, by coating these deformable structures in a silicate layer and changing the fluid, we amplify the van der Waals forces. We examine the competing effects of the structured surfaces, which reduce viscous forces, but enhance adhesion from van der Waals forces. We summarize how the mechanical properties of the plate, drainage channels and deformable structures alter the viscous forces and van der Waals forces associated with detaching in flooded environments.

Acknowledgements

I would like to thank my friends and family who have given me support, encouragement and guidance over the years. I'm so fortunate to have a dependable group of people who have been a comfortable reminder to keep the big picture in mind during the program. When I first moved here, it was hard to imagine I could discover meaningful relationships, but it has been rewarding being exposed to so many interesting people, whatever their story may be in Baltimore.

I am sincerely grateful to my advisor, Professor Joelle Frechette, for her guidance, patience and giving me a chance to work in her lab. Under her mentorship, I was introduced to an interesting observation, shown how to deconstruct it into manageable steps, and then extract something meaningful from all the clutter. I think science is one interesting and critical way to interpret the world and I feel lucky to have learned that from my advisor.

In addition to the current Frechette lab members, I'd like to acknowledge Dr. Christian Pick, Dr. David Broesch and Dr. Rohini Gupta; the lab members before me who offered guidance freely. In particular, I'd like to thank the Masters student, Arianne Sevilla who helped me get started off on the right foot in the Frechette lab. I'm also grateful for the talented and dedicated undergraduates I worked with, Chris Argento and Brian Ryu. I appreciate their patience with me when I was a new mentor, and I found the experience to be one of the most rewarding aspects of science. Finally I'd like to acknowledge Mr. Victor Martin, part of the support staff who unfortunately passed away during my time here. His easy friendliness and good-hearted nature are missed.

Table of Contents

List of Tables

List of Figures

Chapter 1

Introduction

1.1. Motivation

Tree frogs are able to adhere well in a variety of environments, whether they are dry, wet or flooded[1]. Tree frogs and related species can adhere to surfaces in flooded environments, even when they are suspended upside-down in flowing water[2]. This ability has been hypothesized to stem from the structure of their toe pads, which contain drainage channels that aid in removing fluid to facilitate contact with a surface. Understanding how structured surfaces alter the approach and detachment forces in a fluid can have widespread applications, including micro-contact printing[3], self-assembly[4], medical bandages[5], hydrofracturing[6] and cellular adhesion[7].

Despite the possibility of opening new avenues and techniques, there have been relatively few experimental studies on flooded adhesion. Many readers may be familiar with other biomimetic studies, such as studies on geckos[8] and mussels[9]. The mechanisms that allow geckos to stick to surfaces in air are not effective in fluid environments because they require direct contact between the toe pad and the surface[10]. Mussels and barnacles rely on specialized chemicals that work well in harsh, fluid environments[11], but these glues and other types of permanent bonds would significantly hinder tree frog movement as they prevent rapid detachment. The tree frogs' toe pads must be able to incorporate three important design criteria: 1) quickly remove the fluid between the toe pads and surface to prevent hydroplaning, 2) adhere securely once in contact, and 3) modulate this adhesion to detach quickly and easily.

Understanding the role of structured surfaces on tree frog adhesion in flooded environments is complicated by several concurrent phenomena. First, the tree frog's toe pads and their micro-structures are known to be highly deformable (E = 5-15 MPa[12]). Next, the toe pads approach the surface in an approximately normal direction, but then detach in a peeling motion[13]. Finally, the toe pad is exposed to a mixture of dissipative forces from the fluid environment and conservative forces from the van der Waals interactions between the toe pad, fluid and surface. These dissipative and conservative forces each couple with structured surfaces, deformation and detachment via a peeling mode in different ways that cannot be combined with a simple superposition of these effects. While some of these combinations have been studied extensively, such as conservative forces and peeling[14-16], many of them have not, such as the effect of structured surfaces on dissipative forces. We have systematically looked at these phenomena individually to determine the role of each component, and then combined these into a system that mimics the complexity of tree frog attachment.

These studies are inspired by the flooded adhesion of tree frogs and create a foundation to examine how surface structure and deformation can alter approach and detachment forces, and how this picture changes when these forces originate purely from viscous forces, or coupled with van der Waals forces. With these insights, we help clarify mechanisms often found in biological systems that combine deformation, viscous forces and structured surfaces, and offer new tools for fabrication, especially in fluid environments.

1.2. Thesis overview

This thesis summarizes results from a novel peeling device used to test micro-fabricated samples in submerged environments, under controlled loading conditions. The peeling device was used to investigate the phenomena behind the approach and detachment of a tree frog toe pad mimic in flooded environments. The samples and fluid environments have been carefully chosen to isolate individual mechanisms, and then these are all brought together in the final study. First we examined the bending mechanics of unpatterned samples in viscous fluids, then the role of drainage channels in viscous fluids (rigid structures), and finally we examine the role of deformable structures in viscous fluids. We culminate by examining deformable structures in viscous fluids with non-negligible van der Waals forces The appendix covers two side projects that involved different experimental systems and a review paper.

Chapter 2 provides a brief background on the mathematical foundations relevant to peeling flexible samples in viscous fluids. These include applications of the Navier-Stokes equations in the lubrication limit. We use this to scale the onset of fluid drainage through structured surfaces, and describe the applied fluid forces as they couple to an Euler-Bernoulli bending beam. We also describe how to account for the effect of compliant load cells in force measuring devices.

Chapter 3 provides an overview of the custom-made peeling device for peeling samples in fluid environment. It gives details on how samples were created, and how they were chosen to isolate the effect of sample deformation and surface structure in a peeling mode. Characterization of the surfaces is also included in this chapter.

Chapter 4 discusses experiments and analysis of samples with different rigidities peeled in Newtonian fluids of different viscosities. We also explored samples with the same rigidity but different Young's (elastic) moduli. By doing so, we can isolate the effect of bending compliance (rigidity) from the extensional compliance (elasticity), which affect the peeling forces through separate mechanisms. We extended a theory developed for peeling in dry environments to explain our results in flooded environments. We also developed scaling arguments to predict how the forces and work scale with rigidity and viscosity, as well as how far a motor must displace vertically to detach a sample.

Chapter 5 (peer reviewed publication[17], reprinted with permission) discusses the role of drainage channels when peeling in fluid environments. The structured surfaces influence both the approach and detachment dynamics, so we have carefully varied the approach dynamics to determine the role of structured surfaces. We used two different geometries of structures and fabricated them out of SU-8, a rigid photopolymer. We have confirmed that three regimes exist for structured surfaces. At low loading conditions (large separations) structured surfaces and flat surfaces are identical. At intermediate loading conditions (around the critical separation, as determined via scaling arguments), structured and flat samples diverge in their peeling forces. Finally at long loading times, we see that structured samples no longer increase in detachment force for longer loading times, presumably by reaching boundary contact.

Chapter 6 examines the role of deformation and van der Waals forces when peeling samples. We compare a flat and structured surface that has been fabricated out of entirely PDMS, a relatively deformable (E ~ 3 MPa) polymer. As a point of comparison, we also fabricated a PDMS structures on coverslip, to exactly mirror the structured surface in Chapter 5, but with PDMS instead of SU-8. We first examine the role of deformation on viscous forces alone on flat and structured samples and vary the peel velocity. We find that deformation reduces the viscous even further than structured surfaces do on their own and we identify that this probably occurs because of the fluid flow around the pillars, as opposed to additional sources of compliance from either the compressible pillars, the pillars bending, or the substrate deforming. We then alter the chemistry of our system by switching the fluid from silicone oil to a glycerol-water mixture (both fluids have been matched for viscosity), and applying a TEOS coat which creates a glass-like surface on PDMS. This amplifies the van der Waals forces in our system and we see evidence that this enhancement increases the adhesion for our patterned surfaces which more than compensates for the reduction in the purely viscous systems of the previous chapters.

Chapter 7 summarizes the results of this thesis and the contributions we have made to understanding how structured surfaces affect detaching surfaces via a peeling mode in fluid environments. It also discusses future directions that this thesis could contribute to.

In Appendix A, (peer reviewed publication[18], reprinted with permission) we discuss successful efforts of a numerical solution to the normal approach of a deformable sphere to a flat rigid wall, which is relevant to the Surfaces Forces Apparatus. The elastohydrodynamic model in this case has been complicated by the addition of a compliant load cell, which means the approach velocity of the sphere is not defined *a priori*. We are able to match data to experimental results and discuss how deformable surfaces affect making contact in a fluid and the presence of interesting morphologies, such as formation of dimples on the deformable sphere.

In Appendix B, (manuscript under review), we have examined the rolling of a non-colloidal sphere down patterned substrates. We compare pillars and wells. Wells are the negative of pillars and are similar in every way (diameter, areal coverage, material properties) but do not contain any drainage channels. We have systematically varied the patterns to encompass a wide range of diameters and spacing. By doing so, not only do we cover a range of area fractions of patterns, we also have substrates with the same area fraction with different size diameters. We have found that pillars significantly increase the coefficient of friction, presumably because the presence of drainage channels facilitates contact between the sphere and substrate. However the difference between patterns and wells disappears as the areal coverage of patterns increases.

In Appendix C (invited review[19]), we reviewed the role of elastic deformation in viscous fluids and their relevance to force measuring devices. We include basic theory, experimental validation and current challenges in elastohydrodynamics.

Theoretical Background

We overview some of the theoretical background behind the experimental setup discussed in Chapter 3. Our studies are primarily conducted in fluid environments but we still introduce some of the basics behind peel tests in dry environments. Although we do not form or break bonds, overcome van der Waals forces (until the very last portion of Chapter 6), or form any electrostatic interactions, a brief overview of the peel test can help explain why we use a similar device to investigate detachment in fluids.

2.1. Measuring Adhesion via a Peel Test

Adhesives are materials that permit two different objects to be joined together. These adhesive forces could be from conservative interactions, such as van der Waals forces or chemical bonds, or from dissipative forces, such as viscous drag[20]. There are many different techniques to measure adhesion because a test is usually developed with a certain application in mind, either to optimize an adhesive for some end-use product, or to quickly evaluate a wide range of adhesive through simple, repeatable tests.[21] One commonly used class of tests that are relevant to this study are the peel tests. In a peel test, an adhesive (for example, a viscoelastic polymer) is mounted to a backing (which can be very flexible polymer, or more rigid like a glass plate) and this combination is considered a "sample". This sample is brought into contact to a surface and then a force is applied to one end of the sample to remove it from the other surface. This will cause the sample to detach, but because the force is applied to one end of the sample and the backing is flexible, it will induce a bending motion into the sample as it peels.

Some peel tests fix the angle[22-24] at which the sample peels (90° or 180° are some common ones), or can have variable angles[25,26,9,10] during the test (usually <10° for rigid plates). The fixed angle is typically better for studying the steady propagation of a crack between the sample and bottom surface, since this velocity is well controlled. With the variable (small) angle test, the sample can start flush at 0° to the bottom surface, and this is advantageous for studying detachment, because it is focused on the very onset of forming a crack (known as crack initiation). The test described here is considered part of the latter, and could be called a "small angle peel test", or a "beam-bending test".

There are several advantages using a peel test. First, the sample fabrication is relatively straightforward and we can make surfaces with microfabricated patterns without extensive modification. We can also change the sample's environments easily. Second, there have been many quantitative studies on the peel test to help analyze results, the first of these studies were pioneered by Kaelble and Bikerman.[27, 28] Finally, the peel test reasonably mimics the detachment of animals[29] and because it is sensitive to the flexibility of the backing on adhesion, instead of testing the adhesive alone.

However, the majority of the work in this thesis is done on purely dissipative forces – where instead of traditional adhesive we have a viscous liquid film. This means that there is no critical fracture force[30] required to initiate the separation process in our surfaces. In fact, any applied force will begin separating the sample, since the viscous forces are dependent on the velocity at which the sample separates from the bottom surface. While in many adhesives, the peak force will correspond to a molecular property of the adhesive itself, the peak force from a system with purely viscous drag is not linked to a material-dependent, micro-scale event.[31] Furthermore, in dry systems the interface at which the sample, surface and outside environment coexist is usually considered the "peeling front" and closely related to the thermodynamic properties of the system. In our case, the peeling front is a balance between the elasticity of the substrate, the viscous forces and the bending forces[32].

2.1.1. The Viscous Forces between Two Flat Plates

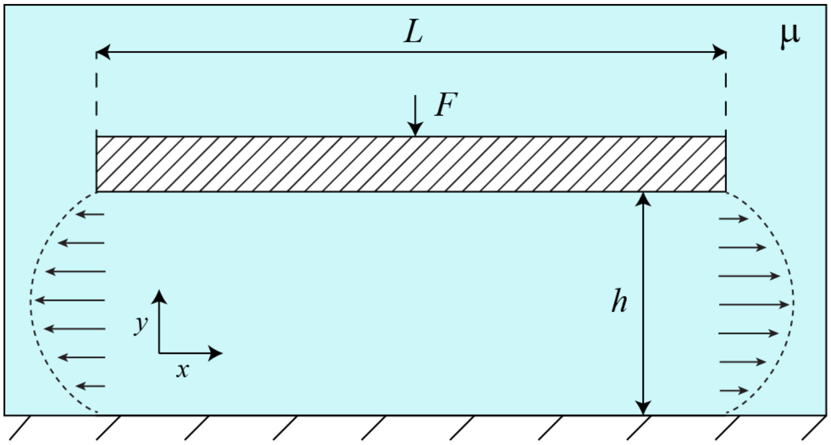

Figure 2.1: Schematic of a flat plate approaching a bottom surface in a viscous fluid. An evenly distributed force, *F*, is applied to a plate of length L in a viscous fluid with viscosity *μ*. This drives the square plate of length *L* closer to the bottom substrate and squeezes out the fluid within the gap between the two surfaces, which are at a separation *h*.

During the approach phase of our experiments, a flat plate is brought towards a bottom surface in a viscous fluid as shown in Figure 2.1. Given the applied force, viscosity, time, initial separation and dimensions, it is possible to calculate the separation between two smooth plates by using the Navier-Stokes equations in the lubrication limit.

The Navier-Stokes equation for an incompressible fluid is given as[33]:

$$\rho(\frac{\partial \boldsymbol{v}}{\partial t} + \boldsymbol{v} \cdot \nabla \boldsymbol{v}) = \mu \nabla^2 \boldsymbol{v} - \boldsymbol{\nabla} P + \rho \boldsymbol{g} \tag{2.1}$$

Where ρ is the density of the fluid, $\boldsymbol{v}$ is the fluid velocity (3D vector), μ is the viscosity, P is the pressure and g is the gravitational constant. Note that a bold symbol indicates a vector.

Due to the high viscosity and relatively low fluid velocities, the viscous terms are dominant over the inertial terms. This regime can be described as low Reynolds number flow (Re). The Reynolds number is a balance of the inertial forces over the viscous forces and given as: $Re = \frac{\rho v D}{\mu}$, where D is the relevant length scale of interest in which the fluid flows over. Ignoring the inertial terms and body forces, we arrive at:

$$0 = \mu \nabla^2 \boldsymbol{v} - \boldsymbol{\nabla} P \tag{2.2}$$

The above equation describes *Stokes* flow, which is a simplification of the Navier-Stokes equation for Re → 0.

We examine the case of two-dimensional flow in Cartesian coordinates and in confined geometries. In this case, the fluid flow is primarily in one axis, in this case v_x and this v_x varies primarily along the y-axis We adopt the notation where v_i is the fluid velocity field along the i-axis. This occurs due to a separation of length scales between the length of the surfaces (~mm) and the comparatively small separation (~µm) between the two surfaces. If we consider the x and y components of the velocity field we find that:

$$\frac{\partial P}{\partial x} = \mu\left(\frac{\partial^2 v_x}{\partial y^2} + \frac{\partial^2 v_x}{\partial x^2}\right) \tag{2.3}$$

$$\frac{\partial P}{\partial y} = \mu\left(\frac{\partial^2 v_y}{\partial x^2} + \frac{\partial^2 v_y}{\partial y^2}\right) \tag{2.4}$$

We non-dimensionalize using the following scheme:

$$x = Lx^*, y = Hy^*, P = \phi P^*, v_y = Vv_y^*, v_x = Uv_x^* \tag{2.5}$$

We can determine the relationship between V and U using the continuity equation (in 2D):

$$\frac{\partial v_x}{\partial x} + \frac{\partial v_y}{\partial y} = 0 \tag{2.6}$$

Rendering the above equation non-dimensional, and rearranging the above equation, we arrive at:

$$\frac{U}{L}\frac{\partial v_x^*}{\partial x^*} = -\frac{V}{H}\frac{\partial v_y^*}{\partial y^*} \tag{2.7}$$

Then the relationship between U and V is given as $V \sim \frac{H}{L}U$:

We can use this to compare the Navier-Stokes equations in the v_y direction by non-dimensionalizing, and substituting V ~ U*H/L:

$$\frac{\phi}{H}\frac{\partial P^*}{\partial y^*} = \mu U\left(\frac{H}{L}\right)\left(\frac{1}{L^2}\frac{\partial^2 v_y^*}{\partial x^{*2}} + \frac{1}{H^2}\frac{\partial^2 v_y^*}{\partial y^{*2}}\right) \tag{2.8}$$

Since the separation between the plates is micron scale and the plates are millimeter scale, $H \ll L$, and it follows that $U^*H/L \gg U$ and thus the contributions of v_y (of order μ U*(H/L)) is negligible compared to v_x (of order μU) in the Navier-Stokes equations. Since $V \sim 0$, $\frac{\phi}{H} \sim 0$, and $\frac{\partial P}{\partial y} = 0$ from equation (2.4) and that $P = P(x)$ only.

Converting equation (2.3) into non-dimensional variables:

$$\frac{\phi}{L}\frac{\partial P^*}{\partial x^*} = \mu\left(\frac{U}{H^2}\frac{\partial v_x^*}{\partial y^{*2}} + \frac{U}{L^2}\frac{\partial^2 v_x^*}{\partial x^{*2}}\right) \tag{2.9}$$

Since $H \ll L$, we can ignore the last term in equation (2.9) since U/H^2 is much larger than U/L^2. This simplifies the original expression in equation (2.3) to:

$$\frac{\partial P}{\partial x} = \mu\frac{\partial^2 v_x}{\partial y^2} \tag{2.10}$$

We can solve equation (2.10) using the following boundary conditions, at $y = 0$, $v_x = 0$ and at $y = h(t)$, $v_x = 0$. Integrating twice and solving for constants, we arrive at:

$$v_x = \frac{1}{\mu}\frac{\partial P}{\partial x}\frac{1}{2}y(y - h) \tag{2.11}$$

From here, using the equation of continuity (equation (2.6)), we can solve for the fluid pressure in terms of the plate velocity.

$$\frac{\partial v_y}{\partial} = \frac{\partial}{\partial x}\frac{1}{\mu}\frac{\partial P}{\partial x}\frac{1}{2}y\,(y - h) \tag{2.12}$$

At $y = h$, the fluid moves at the same velocity as the plate, or $v_y = \frac{\partial h}{\partial t}$

$$12\frac{\partial h}{\partial t} = \frac{\partial}{\partial x}\frac{h^3}{\mu}\frac{\partial P}{\partial x} \tag{2.13}$$

The above is a simplified version of the Reynolds equation[34]. To find the relationship between separation, applied force and time, we solve equation (2.13) for the force, F, by integrating the pressure, and then solving for h as a function of t and F. We assume here that the plate does not vary in the x-axis, or that $h \neq h(x)$.

$$\frac{\partial h}{\partial t} = -\frac{h^3}{\mu L^4}F \tag{2.14}$$

$$F = -\frac{\mu L^4}{2}\left(\frac{1}{h^2} - \frac{1}{h_i^2}\right) \tag{2.15}$$

Where h_i is the initial separation of the plates. For the approach, the separation between the plate and surface is large at $t = 0$ and $\frac{1}{h_i^2}$ is usually considered negligible.

2.1.2. Drainage Channels on Viscous Forces

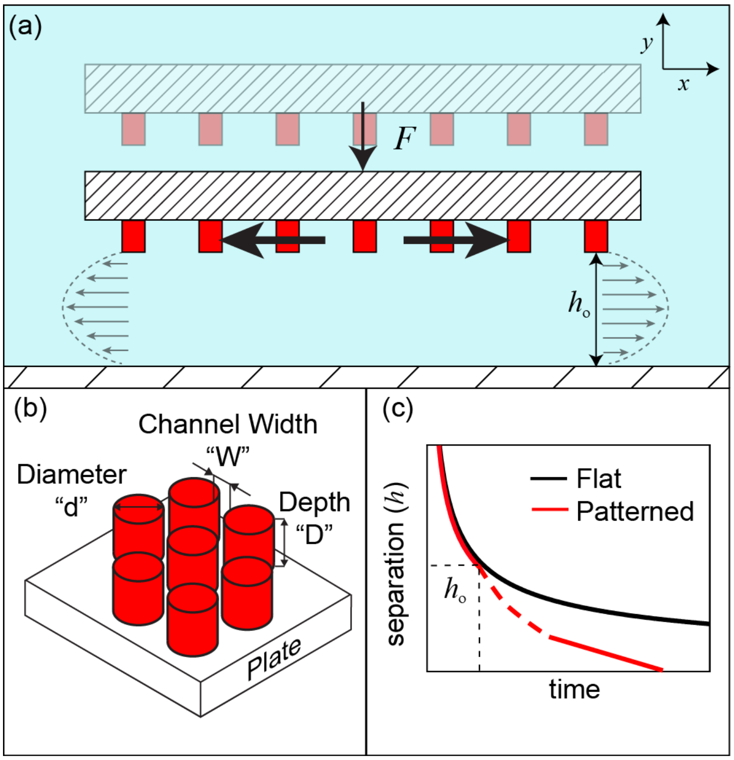

Figure 2.2: Schematic of a patterned plate (red) approaching a bottom surface. In (a), a structured surface shows drainage through the patterns at a separation ~ h_o. The dimensions of the patterns are shown in (b). A schematic illustration showing the difference in separation (*h*) versus time of a flat versus patterned sample. Deviation begins at a separation of h ~ h_o.

The section before derived an expression for the viscous force when bringing two flat surfaces into contact in a fluid. However if one the surfaces is textured, the drainage rate can be altered if the fluid enters into the space between the structures as shown in

Figure 2.2. Due to the complexity of the periodic boundary condition, no analytical expression exist for the effect of drainage channels. However a scaling argument by Persson[35] has been validated and serves as an approximate method to account for the depth, height and spacing of structured surfaces. A structured surface will deviate from a smooth surface at separation length scales of $\sim h_o$ and once a structured surface is at or smaller than this length scale, they will drain faster than their flat counterparts.

Persson's scaling argument[35] is derived as such. Let us assume that we are at separations when the fluid flows into the channels and that this occurs because a plate of diameter Do is approaching a bottom surface. In the limit that the structure depth D, is much larger than the width (W), the largest velocity gradient occurs along the width. Then the Navier-Stokes in 2D (equation 2.2), scales as:

$$\frac{P}{D_o} \sim \mu \frac{v}{W^2} \tag{2.16}$$

Where v is the velocity of the fluid in the x-direction and P is the pressure. The cross-sectional area of this channel is $\sim WD$, and the total number of channels on the surface is $N*WD$, where N is the number of structures on a surface and approximated as the entire diameter of the surface divided by the diameter of a single structure and the spacing over the entire diameter of the surface ($D_o/(d+W)$). If the rate of change in separation between the plate and surface is given by $\frac{\partial h}{\partial t}$, then the total mass of fluid entering the channels (assuming it is completely draining through the channels) is given by:

$$\frac{\partial h}{\partial t} D_o^2 \sim v \frac{D_o}{d+W} WD \tag{2.17}$$

Combing equations (2.16) and (2.17) by substituting v, we arrive at:

$$\frac{\partial h}{\partial t} \sim -\frac{PW^3D}{\mu D_o^2(d+W)} \tag{2.18}$$

We have postulated that the plate is moving at an instantaneous velocity of $\frac{\partial h}{\partial t}$. Using the results from lubrication theory, we can estimate what separation this drainage rate and pressure would correspond. Ignoring constants, we scale the Reynolds equation for flat plates from the previous section (equation (2.13)).

$$\frac{\partial h}{\partial t} \sim -\frac{Ph^3}{\mu D_o^2} \tag{2.19}$$

Combining equations (2.18) and (2.19) and solving for h, we find an expression for h_o, the separation (approximate) at which fluid flow through drainage channels becomes relevant.

$$h_o = W\left(\frac{D}{d+W}\right)^{\frac{1}{3}} \tag{2.20}$$

Drainage channels imply that structured surfaces will reach very small separations (considered contact for the scale of roughness in our system) much quicker than flat surfaces. This is because the drainage rate (equation (2.18)) no longer depends on the separation as $1/h^3$, and is linear with time at separations where drainage through the channels dominates (this represented by linear portion of the patterned surface in panel c of Figure 2.2). This expression is only valid for the normal approach of two surfaces.

2.2. Elastic Deformation

2.2.1. Bending a Beam in a Fluid

We model the detachment of the plate as a bending beam that deflects in one axis only.

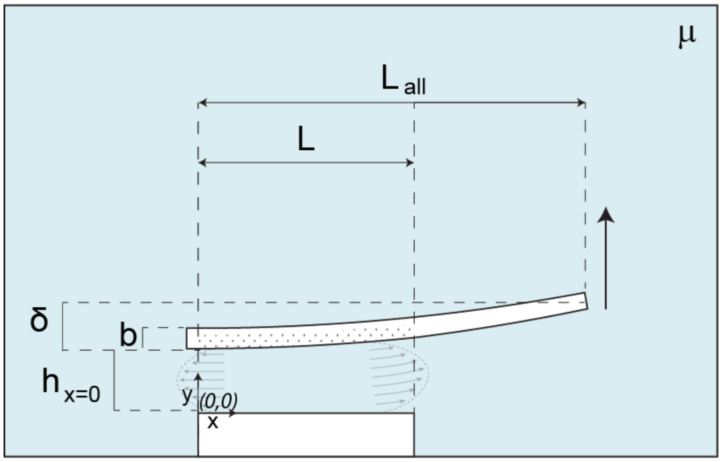

Figure 2.3. Bending during detachment. As the plate is detached (represented by the arrow on the right), the viscous forces cause the plate to bend. The plate is a length L_{all}, is a thickness b and is distance δ+h from the bottom surface. The viscous force (fluid viscosity μ) only occurs where the plate overlaps with the bottom surface, over a length L.

Although the beam is not static during the experiment, the shape of a beam in response to the load is quasi-static which we justify below.

The Euler-Lagrange equation for a prismatic beam is given as[36]:

$$EI\,\frac{\partial^4 w}{\partial x^4} + \lambda\frac{\partial^2 w}{\partial t^2} = q(x) \tag{2.21}$$

Where E is the Young's modulus, I is the second moment of inertia (for a rectangular plate, given as $\frac{L_{all}}{3d^3}$), w is the deflection of the beam, λ is the mass per unit length of the beam and q(x) is the distributed load on the beam.

We compare the two terms on the left-hand side of equation (2.21). Relevant time scales of peeling occur over a time of ~ 2 seconds. The rigidity of a 2 mm x 22 mm x 0.13 mm glass coverslip is 1.2 x 10^{-3} Nm^2 and the mass per unit length of a coverslip is around 6 x 10^{-3} kg/m. The length of the coverslip is 22 mm. Ignoring the scaling of w, which is present in both terms, the first term scales as 5.1 x 10^6. The second inertial term scales as 1.5 x 10^{-3}, which demonstrates that we can safely ignore inertial terms.

Thus equation (2.21) simplifies to the Euler-Bernoulli bending beam equation:

$$EI\,\frac{\partial^4 w}{\partial x^4} = q(x) \tag{2.22}$$

Since the applied force on the beam is from the viscous forces, we can substitute the hydrodynamic force (equation (2.14) into *q(x)*), which is the force per unit length. Doing so, we arrive at:

$$EI\,\frac{\partial^4 h}{\partial x^4} = \frac{\mu L^3}{h^3}\frac{\partial h}{\partial t} \tag{2.23}$$

We have transformed w adding the initial height (a constant) to match the height of the plate h.

Chapter 3

Experimental Background

3.1. **Peeling Apparatus**

To understand how structured surfaces detach in fluid environments, we have constructed a custom peeling apparatus. A schematic and a picture of the device are shown in Figure 2.1. The test consists of two distinct phases, an approach phase – where samples are brought closer to the bottom surface and a detachment phase – where the force versus motor displacement is recorded as the sample is detached from the bottom surface. The fluid can be changed easily and we use either silicone oil or a glycerol-water mixture in our experiments.

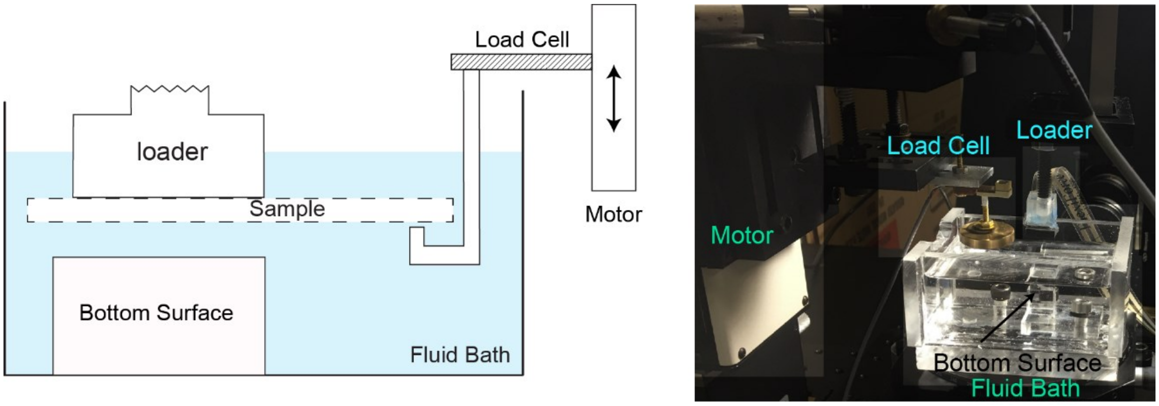

Figure 3.1. Schematic and picture of peeling apparatus. The peeling apparatus consists of a loader, which brings a sample (not pictured) to a bottom surface in fluid bath. During detachment, a motor is moved upward and the load cell records the forces required to

detach the sample. No sample is present in the picture. The loader also has a sensor attached to measure the applied force.

3.1.1. Approach

During the approach phase, a sample is brought closer to the bottom surface because of the force applied by the loader. The theoretical separation between the sample and the bottom surface is given by solving the Reynolds equation (Equation (2.15)), provided below), assuming the sample is flat and remains parallel during the approach.

$$F = -\frac{\mu L^4}{2} \left(\frac{1}{h^2} - \frac{1}{h_i^2}\right) \tag{2.15}$$

A study by our group has examined the effect of drainage channels during the approach, but no analytical expression exists outside of the simple scaling argument by Persson[35] detailed in Chapter 2. We do not measure the separation between the sample and substrate, and factors such as tilt, roughness, or attractive interactions (such as van der Waals forces) can accelerate drainage[37]. Since the approach is not usually shown in the later chapters, a typical completely data output from the device is shown below.

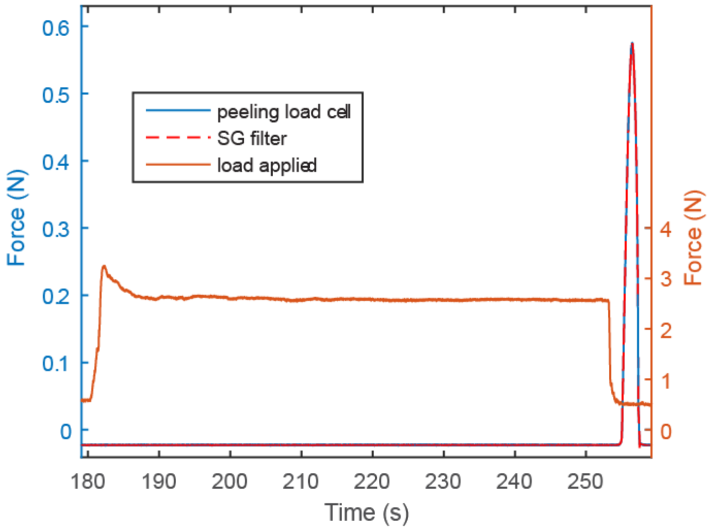

Figure 3.2. Typical MATLAB output from peeling experiment. The approach (orange) and detachment (blue + red) force versus time is shown. These outputs are from two different sensors. The peeling data appears (spike on right at time ~ 260 s) compressed due to the relatively longer time spent in the approach phase.

For the studies that minimize van der Waals forces, bottom surfaces consists of a glass coverslip onto which a thin fluoropolymer layer of 1.55% CyTop (Bellex International Corporation) is spin coated at 5000 rpm for one minute and then annealed in an oven for 15 minutes at 180°C. For studies with van der Waals forces, the CyTop is omitted.

3.1.2. Detachment

[This section has been reprinted with minor modifications with permission from: Dhong, C., & Fréchette, J. (2015). Coupled effects of applied load and surface structure on the viscous forces during peeling. *Soft matter*, *11*(10), 1901-1910.]

Once the loader is pulled away from the back of the coverslip, the peeling phase starts. In the peeling phase, the flexible sample is peeled off the substrate by a rigid contactor moving at a constant drive velocity of 300 μm/s and connected to a load cell (k=6.3 x 10^3 N/m, Omega LCL-816G). As viscous forces scale with the velocity, we selected velocities from 200-600 μm/s as the drive velocity to exploit the full range of the load cell) while remaining in the lubrication regime. While the drive velocity is constant, the actual velocity at which the sample and substrate separates is less than the drive velocity because of the hydrodynamic drag, and varies both with time and position.[31] As an upper bound, we estimate the Reynolds number to be Re <1 based on a film thickness of order microns, a length of 12 mm, and a peeling velocity less than 1mm/s. Throughout the peeling process the bending of the coverslip remains in the small angle limit (<5°). In this limit we do not have to consider the potential energy from the movement of an inextensible film with an applied force.[38] Additional possible contributions to the forces measured are the elasticity of the coverslip during bending, the viscous forces from the fluid film, the compliance of the polymer film, and the conservative surface forces (such as van der Waals interactions)[38-41]. In most of these studies, there is negligible contribution from conservative surface forces (e.g. electrostatic or van der Waals interactions). By using a rigid backing[23] the elastic work term is much smaller than the viscous work[38]. An estimate of the bending contribution is ≪1% of the entire work (since the elastic stress term is usually much smaller than the Young's modulus) and is thus negligible.[25, 39]

3.2. **Samples**

The rationale behind our design was to incrementally increase the complexity of the sample and experimental system to understand how viscous forces interact with 1) a peeling sample, 2) drainage channels 3) deformable structured surfaces and 4) deformable structured surfaces with van der Waals forces. This is reflected in the figure below.

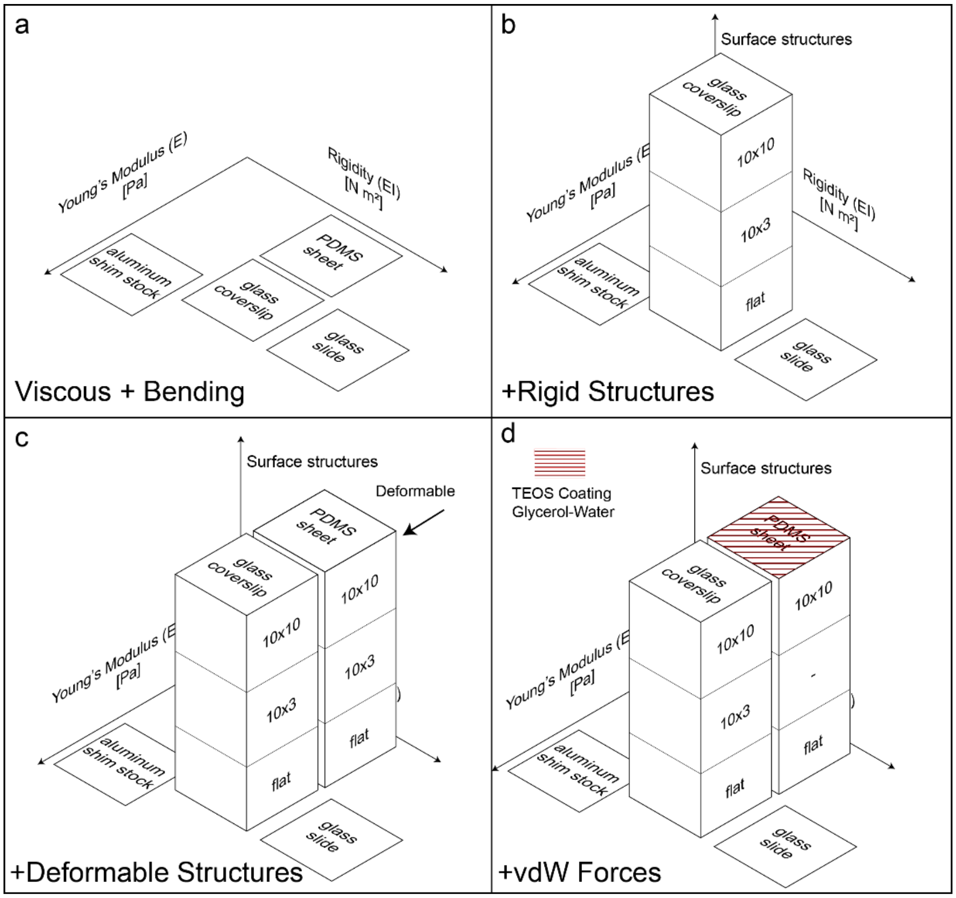

Figure 3.3. Schematic of Sample Design and Progression. The samples have been designed and tested with increasing complexity. In a), samples vary in rigidity, as well as the Young's modulus (compared to another sample with the same rigidity). In b), the sample has been micropatterned with rigid SU-8 to create drainage channels. In c), the sample has been changed from a coverslip to a PDMS sheet to create deformable structures as well as a coverslip with PDMS structures for comparison. In d) the sample has been coated with a glass-like TEOS (silicate) layer and the fluid replaced from silicone oil to glyercol-water to amplify van der Waals forces.

All samples in this study are square and were chosen to be the same areal size so that we could compare samples across different studies (see **Table 3.1**). In Chapter 4, we examine the role of rigidity and extensional compliance, but in the remaining studies of Chapter 5 and 6, we keep the sample rigidity the same to isolate the effect of structures. The samples in Chapter 5 are backed only on coverslips, while Chapter 6 consists of one sample set made from coverslips, to draw comparisons to Chapter 5, but then the rest of the samples are made from PDMS sheets. These PDMS sheets however, have the same rigidity as the coverslips used. The length (L) is different than the total length of the sample (L_{all}) because the sample interacts with the bottom surface over an area of LxL.

Table 3.1 Sample geometry and rigidity.

Sample	Young's Modulus **E** (MPa)	Total Length **L_{all}** (mm)	Length **L** (mm)	Thickness **d** (mm)	Rigidity **EI** (Nm^2)
Glass slide	67×10^3	22	12	1.0	0.56
Glass coverslip	67×10^3	22	12	.13	1.2×10^{-3}
Aluminum shim	69×10^3	22	12	80×10^{-3}	3.0×10^{-4}
PDMS slab	3.0	22	12	3.8	1.2×10^{-3}

3.2.1. Fabrication

Samples were made using traditional microfabrication techniques. These allowed us to add microfabricated structures on top of the sample substrate. Since the layer with the patterns is relatively thin (20 μm), we can alter the surface topology while preserving the mechanical properties of the sample substrate.

3.2.1.1. SU-8 Structures

[This section has been reprinted with minor modifications with permission from: Dhong, C., & Fréchette, J. (2015). Coupled effects of applied load and surface structure on the viscous forces during peeling. *Soft matter*, *11*(10), 1901-1910.]

SU-8 coated samples consist of a 20 μm layer of SU-8 2007 (MicroChem) supported by a glass coverslip (Schott D263M, 22x22 mm, 0.13-0.16 mm thickness). The structured surfaces have features only on the top 10 μm that consist of cylindrical pillars in a hexagonal array. For all the samples the final SU-8 thickness is achieved in two sequential 10 μm coatings on coverslips. Traditional microfabrication techniques are used to pattern the surface features. First, square glass coverslips are cleaned using an isopropyl alcohol/ethanol rinse followed by a dehydration bake at 200° C for 10 minutes. Then a layer of SU-8 2007 is spin coated at 1700 rpm for one minute to produce a 10 μm thick layer. The square substrate requires manual edge bead removal with a razor blade, which is followed by a pre-exposure bake on a hot plate at 95° C for 3 minutes and then exposure to a UV light at 140 mJ/cm^2. The base layer requires no mask or chemical developing and the sample is hard-baked at 200° C for 10 minutes immediately after exposure. After cooling, a second layer of SU-8 is deposited using the same steps as the initial layer, but a chrome mask is used during the exposure step to create the surface patterns and a simple transparency mask is used for the smooth surface. For all the samples, the feature area is 12 mm x 12 mm and thus does not cover the entire coverslip substrate surface. Effort was made to manually center the mask with the coverslip, but there is sample-to-sample variation of order 1 mm from the edge of the patterned region to the edge of the coverslip. UV exposure is followed by a post-exposure bake at 95° C for 5 minutes and then immersion in SU-8 developer for 3 minutes with gentle manual agitation. Samples are then rinsed in isopropyl alcohol and hard baked at 200° C for 10 minutes. Pattern formation and layer thicknesses are verified using confocal imaging and profilometry.

3.2.1.2. PDMS Structures

Sample Fabrication of PDMS Sheets. PDMS sheets (22 x 22 x 3.8 mm) are fabricated by using two molds. The strategy is to create a template of SU-8 pillars on a silicon wafer is molded by PDMS, and then that PDMS mold is treated with a trichloro(1,H,1H,2H,2Hperfluorooctyl) silane to make a mold for the final sample. The template was created by two-layer photolithography. A silicon wafer was cleaned with isopropyl alcohol/ethanol and then hard baked at 200^o C for 10 minutes. Then, for the first layer, a 10 μm thick layer of SU-8 was created by spin coating SU-8 2007 (MicroChem) at 1700 r.p.m for one minute. This was pre-exposure baked on a hot plate at 95^o C for 3 minutes and then exposed to a UV source (i-line) at 140 mJ/cm^2. This layer required no mask. After UV exposure, the samples were baked again in a post-exposure bake for 3 minutes at 95^o C. After the sample cooled, the same procedure as before was done again, but during UV exposure, a chrome mask was used to develop the hexagonal array of 10 μm diameter, 10 μm channel width (20 μm center-to-center distance) pillars. Then after the post-exposure bake, samples were developed in SU-8 developer (MicroChem).

With the SU-8 template ready, we created a PDMS mold from this by casting a 10:1 PDMS elastomer mix (Sylgard 184, Dow Corning) onto the wafer. The 10:1 PDMS mixture has been degassed before use. We use a large weigh boat to enclose the wafer and tape it to the bottom to ensure that the wafer remains stationary. We pour a 1 mm thick layer and then degas again to ensure the PDMS infiltrates into the pillars. This is then cured at 100^o C for 5 hrs. Once cured, the PDMS is gently peeled away from the wafer. Finally, to prepare a mold made from PDMS for use in casting the same material, it is necessary to silanize the mold thoroughly[42]. The PDMS mold was placed inside a desiccator with 20 μL of trichloro(1,H,1H,2H,2H-perfluorooctyl) silane (97%, Sigma Aldrich) placed on a glass dish. The desiccator was then evacuated under coarse vacuum and incubated for 12 hrs. Then the sample was placed in an oven at 100^o C for one hour to anneal the silane.

With the mold ready, samples were made by pouring uncured PDMS (10:1 ratio) to a 3.8 mm thickness, degassing to ensure infiltration into the patterns, and then baking at 100^{o} C for 5 hrs. and removing the samples carefully after curing. Flat samples are made by casting PDMS onto a silicon wafer for flatness.

Sample Fabrication of PDMS Pillars on Glass Coverslips. PDMS pillars on glass coverslips were created by casting PDMS into an SU-8 mold on silicon and then carefully removing the PDMS layer and bonding it to a glass coverslip via oxygen plasma. The SU-8 mold is fabricated exactly as described before, but instead of pillars, the opposite – wells, were fabricated. Then a 20 µm thick layer of PDMS was cast into the SU-8 wells by spin coating at 1150 r.p.m for 1 minute. Due to the difficulty in peeling 20 µm thin PDMS layers from a mold, thicker portions of PDMS elastomer were painted outside the desired feature to aid in handling. The 20 µm thick PDMS layer was then treated on the unpatterned side with a handheld tesla coil for 40 seconds and then pressed firmly onto a clean glass coverslip. This was then heated on a hot plate for 2 hrs. at 100^{o} C.

3.2.1.3. TEOS Coating

The TEOS coating procedure was taken from the method described by Abate et al.[43] but adapted to coat planar substrate, instead of the inside of a microfluidic channel. It was also adapted to ensure the coating is thin enough to preserve the patterns. As described by Abate et al., we prepared a 1:1:1:1 solution of TEOS (tetraethyl orthosilicate, reagent grade 98% Sigma Aldrich), MTES (triethoxymethylsilane 99%, Sigma Aldrich), HCl adjusted to pH 4.5 with D.I. water, and ethanol. This solution was stirred gently on a hot plate at 65^{o} C for 12 hrs. After a brief nitrogen air clean on the PDMS sample, it was exposed to oxygen plasma for 30 seconds at 50W and the TEOS solution was spin coated onto the PDMS surface by spinning on a spin coater at 1000 r.p.m. for 30 seconds. This was then cured on a hot plate at 100^{o} C for 2 minutes. This resulted in a layer approximately 500 nm verified by profilometry. We estimate the Hamaker constant for this system to be of the same as a system made from SiO_2-Water-SiO_2 , which is equal to 0.63 x 10^{-20} J[44].

3.2.1. Characterization

Sample characterization included the contact angle hysteresis using DI water over time for the TEOS coating layer and the roughness of each surface across the various treatment methods. We also verified the sample fabrication with confocal microscopy and pictures can be found in the relevant experimental chapters.

Table 3.2 Contact angle hysteresis of TEOS treated PDMS samples using DI water.

Time (hrs.)	Hysteresis (°)	Advancing (°)	Receding (°)
1	N/A	16-23	N/A
3	8-11	28-64	20-53
20	7-18	38-49	30-35
48	7-17	56-73	27-65
120	18-20	77-81	59-61

The sample roughness is tabulated below, measured via profilometry and an arithmetic average roughness was taken (R_a). There does not seem to be a large change in the roughness from the thin coating, which suggests it applies conformal to the substrate.

The effect of roughness on adhesion and contact is a well-studied phenomenon that is still active and is not covered in this work, but some of the classical references, especially in the context of fluids, is provided in these references.[45-47]

Table 3.3 Sample and bottom surface roughness. *refers to materials used as the bottom surface.

Sample	Young's Modulus **E** (MPa)	Coating Material	Roughness **Ra** (nm)
Glass slide	67×10^{3}	SU-8	9.1 ± 4.8
Glass coverslip	67×10^{3}	PDMS	17 ± 5.5
		SU-8	5.4 ± 2.0
Aluminum shim	69×10^{3}	SU-8	38 ± 7.7
PDMS sheet	3.0	PDMS	410 ± 41
Glass slide*	67×10^{3}	CyTop	8.4 ± 4.3
Acrylic*	3.1×10^{3}	CyTop	59 ± 41

Chapter 4

The Role of Rigidity and Compliance when Peeling Flexible Beams in Viscous Fluids

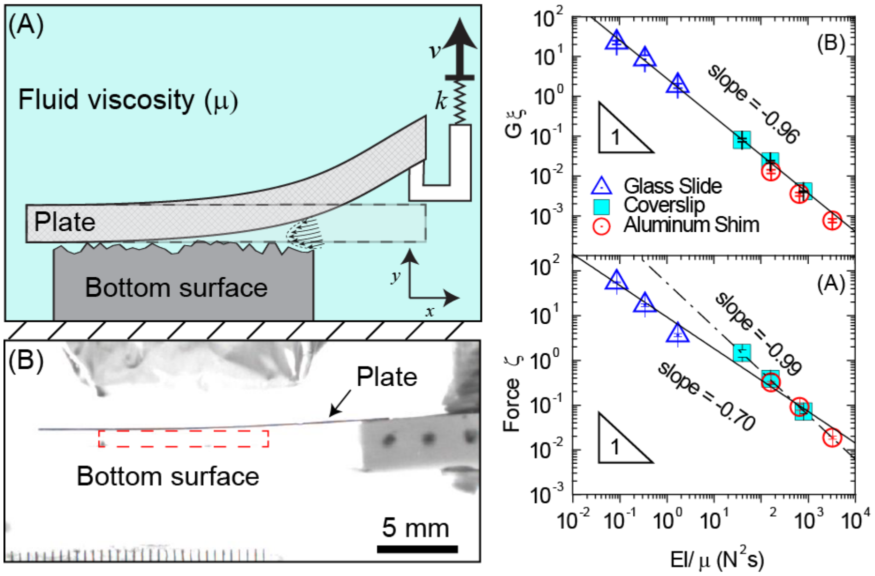

4.1. **Introduction**

Consider two plates in contact in a viscous fluid where the top plate peels from one end away from the bottom plate, as shown in Figure 1. In the absence of surface forces (such as capillary or van der Waals interactions), only the lubrication forces hold the surfaces together as the plates separate via peeling. This peeling motion is very common in animal locomotion[1, 29], printing[48], blister formation[40], or adhesion[23, 49-51]. In all these settings, the mechanical properties of the material being peeled dictate its performance by controlling either (or both) the detachment forces or the velocity of the peeling front. For instance, the growth rate of a liquid blister caused by liquid injection under a flexible sheet is slower when only considering the deformation due to the fluid pressure.[40] The locomotion of tree frogs on wet or submerged surfaces involves a peeling motion analogous to the one illustrated in Figure 1[1]. In dry environments, the wide range of adhesion properties observed with different species correlates strongly with the compliance of their toe pads[12], and in wet environments, tree frogs have been shown to rely on a mixture of viscous and capillary for adhesion[52]. Insects have also been shown to secrete adhesive fluids that aid in their attachment to smooth surfaces, whether or not their attachment pads are smooth or textured.[53] The detachment of a stamp during micro-contact printing also occurs by peeling surfaces that were initially in full contact, and the effectiveness of ink transfer depends strongly with the mechanical properties of the stamp[54, 55]. Viscous fluids also often act as model systems for more complex viscoelastic adhesives, such as pressure sensitive adhesives (PSAs), for which detachment via peeling is the most common mode of separation,[23, 27, 56-58]. Therefore, the broad technological relevance related to peeling of flexible sheets in viscous fluids makes understanding the coupling between the mechanical properties of the bending plate and the viscous forces generated during the detachment particularly important.

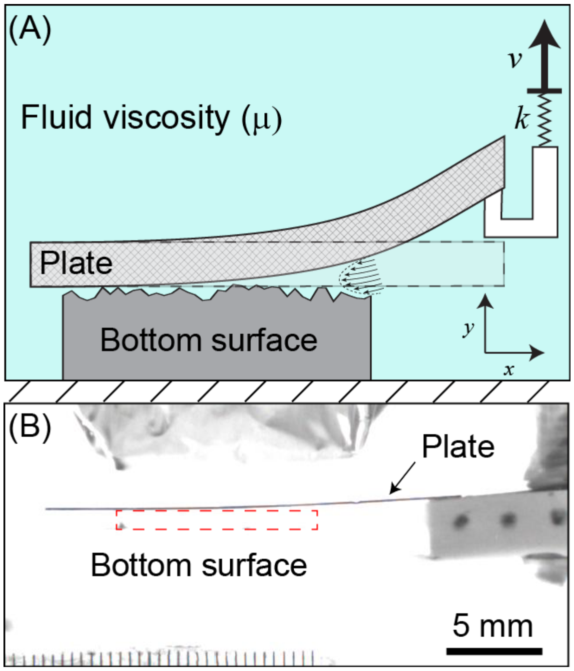

Figure 4.1. Schematic and image of detachment via peeling in a fluid. In the schematic in (A), a plate is peeled from a bottom surface by a contactor (far right) inside a bath filled with a Newtonian fluid with a viscosity of μ. The contactor is mounted on a load cell (spring constant, k) driven by a motor at constant velocity v. During the detachment the plate deforms due to the lubrication forces originating from the infusion of fluid within the gap formed by the plate and the bottom surface. In (B) a typical detachment is shown for a coverslip in 200 cSt silicone oil. The bottom surface is not visible in the high contrast and is outlined with a red dashed box. The bending plate (colored with a permanent marker) is clearly visible. Scale bar corresponds to 5 mm, and each tick on the bottom left of the image is 0.5 mm. The loader is visible (aluminum box near top) but does not interfere with detachment.

The detachment process illustrated in Figure 1 also bears significant resemblance to crack initiation and peeling of reversible dry adhesives[15, 21, 25, 59]. Reversible dry adhesives are materials that can adhere to other surfaces in the absence of glue or other mediating fluids[20], for example surfaces designed to mimic the microstructures found on the Gecko toe pads[10, 29, 60]. The role played by mechanical compliance on the performance of reversible dry adhesives has been studied extensively[61, 62]. As a result, there is a consensus that minimizing the overall compliance of the adhesive maximizes adhesion.[30, 63-65] In the context of detachment via peeling, minimizing compliance requires maximizing the flexural rigidity (controlled by EI) and the extensional rigidity (controlled by E), where E is the Young's modulus and I is the second moment of inertia of the bending plate. While the effect of compliance on adhesion has been predicted and demonstrated for dry adhesion[66-68], its extension to adhesion in fluid environments has been investigated to a much lower extent. In particular, studies of peeling in fluids have mainly focused on the steady-state regime (i.e. constant peel angle), where the bending of the plate is set by the desired peel angle.[23, 56] It is unclear if the initial phase of peeling, when the peeling front is first created, follows a similar dependence on the compliance of the plate than its steady-state counterpart. As a result, a better understanding of the role of compliance for peeling in fluids, and how it compares to the more common case of steady-state peeling, could help incorporate the role of fluid viscosity to the design of materials and surface structures with optimal reversible adhesion that can operate in fluid environments.

Related studies on the bending and oscillation of flexible sheets caused by fluid flow also highlight the coupling between viscous forces and the bending rigidity of the plates. Work by the Mahadevan group, for instance, describes the change in shape of a flexible sheet as fluid flows between the thin gap that separates it from an underlying surface.[69, 70] In particular they observed that increasing the flow rate can lead to shorter propagating waves across the flexible sheet, but increases the frequency of these bursting events. Along the same lines, Lister et al.[40] studied the growth of a fluid blister in radial geometry in the presence of viscous, van der Waals and gravitational forces and showed that blister growth was dominated by peeling at short time regimes but then growth became a mixture of peeling and pulling via tension in the sheet as the blister grew. While these studies successfully characterized how morphologies such as blistering or propagating waves occur at different flow rates, part of the part of the model development is simplified because either the flow rate of the fluid or the shape of the flexible beam is specified. The case of the peeling of a flexible sheet is not as well specified. The force-displacement curves are measured but the fluid flow rate, the shape of the plate, or the peel velocity are not set *a priori*. In particular, the presence of a load cell to measure the detachment force leads to a discrepancy between the motor and contactor displacement[31] and needs to be incorporated in the analysis.

Here, we characterize systematically the effect of the compliance (flexural or extensional) of the top plate on the force required to separate it from a bottom surface in completely submerged environments. We also investigate how the detachment forces depend on the peeling velocity and fluid viscosity. In particular, we aim to isolate the contribution of the extensional compliance from that of the flexural compliance by comparing the detachment of plates with the same bending rigidity but different Young's modulus. The role of the flexural compliance on the detachment forces is compared to predictions based on treating the plates as an Euler-Bernoulli beam with a distributed load originating from the lubrication forces. Additional contributions to the detachment forces originating from the extensional compliance are analyzed based on stress decay length arguments developed by Ghatak *et al* [71].

4.2. **Materials and Methods**

All the experiments described here are performed in a custom peeling apparatus similar to the one developed by Chaudhury[26, 72]. One key difference is that the contact formation (initial loading) and detachment are performed under completely submerged conditions (see Figure 2). Initial boundary contact between the two plates is achieved prior to peeling by applying a constant normal load on the top plate (minimum of 2N for 180 seconds). After loading, a contactor lifts the sample from one end and separates it from the lower surface. This contactor is mounted onto a compliant load cell ($k = 6.3\text{x}10^3$ N/m) and is driven by a motor at constant velocity ($v = 200\text{-}600$ μm/s). All the experiments are performed in a fluid bath filled with Newtonian silicone oils of varying viscosities (50 cSt, 200 cSt and 1000 cSt). We showed previously that the detachment forces have a non-linear dependence on the loading conditions.[73] For short dwell time, the applied load drains fluid from the gap between the plate and the bottom surface. In this regime, the detachment forces increase with dwell time because the decrease in the thickness of the fluid film trapped between the two surfaces leads to an increase in the lubrication forces during detachment. Then, for longer dwell times, the detachment force no longer depends on time, likely because boundary contact at asperities has been reached.[17] All the peeling measurements performed here fall within the long dwell time limit (see supporting information for more details on the effect of dwell time). Note also that the plates are coated with a non-polar film and the experiments are performed in silicone oils to minimize (or eliminate) the contribution of van der Waals interactions in the forces measured.

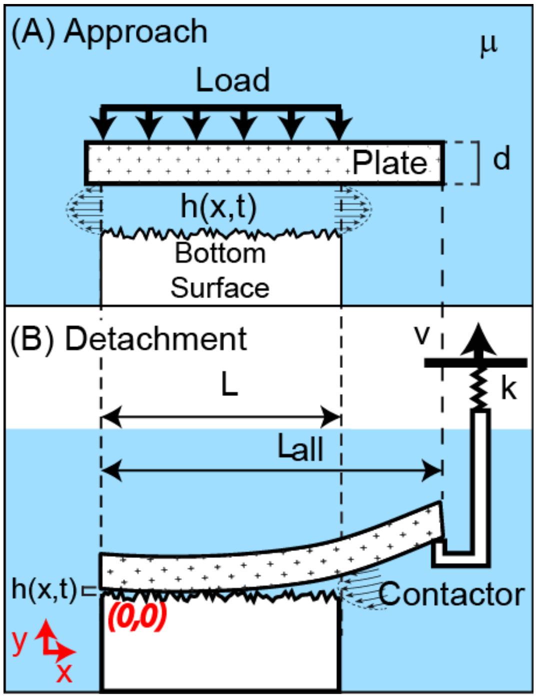

Figure 4.2. Schematic of peeling experiments where contact and detachment occurs under completely submerged conditions. (a) Loading to bring the plate into boundary contact with the lower surface. (b) For peeling, a rigid contactor lifts one end of the top plate, causing detachment with a small (<5o) peel angle. The contactor is mounted on a load cell (with spring constant k) driven at a constant velocity v.

4.3. **Results and Discussion**

The detachment forces during the peeling of plates made of glass (slides and coverslips) as well as aluminum is shown in Figure 3. All the plates have the same nominal contact area with the lower surface and were selected to span a broad range of flexural rigidities while maintaining a relatively high (and constant) Young's modulus. For each plate, we measured the detachment forces in Newtonian silicone oils with viscosities of 50 cSt, 200 cSt, and 1000 cSt. All the force-displacement curves have the same general qualitative features where the forces increase initially, reach a peak and then go to zero. The forces we measure are mainly lubrication forces, therefore once the fluid film between the plates is large enough the lubrication forces no longer act, and the forces reach zero (i.e. in the absence of lubrication interactions the drag force of the plate is below our resolution limit). For any given plate (within a single panel in Figure 3), increasing the viscosity increases the peak force and motor displacement necessary to separate the plates. In addition, we observe that for a given plate increasing the viscosity leads to the same initial slopes and the same general shape of the force-displacement curves. Finally, we also find that increasing the rigidity the plates (aluminum to glass slides in Figure 3) and keeping the viscosity constant (e.g., the first curve in each panel) leads to an increase in the magnitude of the forces. Increasing both the rigidity and viscosity increases the detachment forces, a trend also observed during steady-state peel tests[23].

In contrast to increasing the viscosity, increasing the rigidity of the plates reduces the motor displacement necessary for the detachment. Since the motor is driven at constant velocity, the narrowing force-displacement curves with increasing rigidity means the detachment occurs faster. A higher bending rigidity has been shown to correspond to a faster radial growth of liquid blisters and has also been shown to correlate with a faster propagating bursts in a pinned elastic sheet for a given flow rate.[40 69] Finally, we observe that the initial increase in the detachment force for the glass slide is relatively linear than for the other two plates and once it reaches a peak the forces for the glass slides decrease much more abruptly than for the other two plates. In our experiments, we visually observe (see supporting information for images) that the glass slide does not appear to bend visibly throughout the peeling process, even though the forces are increasing due to its high rigidity. In contrast, we observe that for the glass coverslip and aluminum shim, the section of the sample between the bottom surface and the contact are visibly bent before the samples begin to peel off the bottom surface. This suggests that the glass slide detaches in a lifting motion, instead of peeling and the force curve of the glass slide is more visually similar to experiments in detaching rigid substrates in a probe-tack geometry of viscous liquids.[74]

The slope of the force-displacement curves before the peak force is reached increases with rigidity, and for a given plate, material is independent of viscosity (see Figure 3). For normal displacement, such as in probe tack tests, the slope of the force-displacement curves is determined by the compliance of the load cell[66] (constant throughout all experiments). We see here that for a peeling motion the bending compliance of the plate also plays a role (along with the compliance of the load cell) in determining the initial slope of the force-displacement curves. The initial slope has been shown to depend on the total compliance in other experimental system as well. This dependence was demonstrated for peeling viscoelastic adhesives[39] and also in more complex composite adhesive that were detached in a variety of modes, not limited to peeling[61, 64].

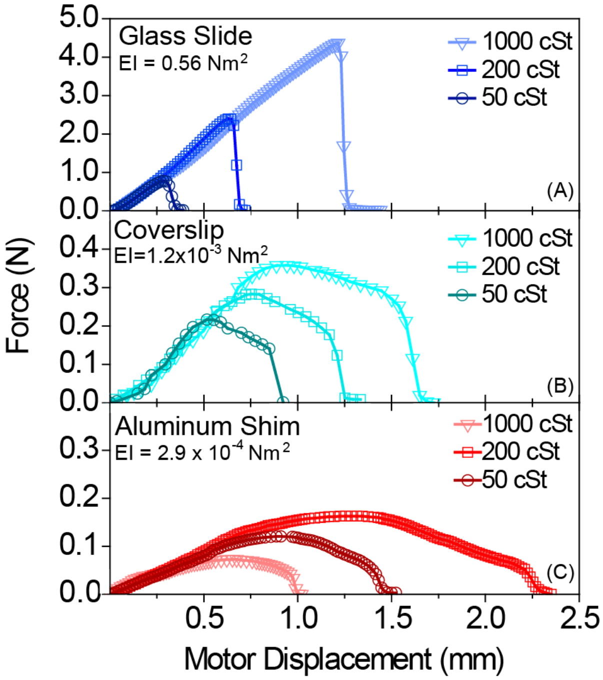

Figure 4.3. Curves showing the detachment force as a function of motor displacement during the peeling of plates of different flexural rigidities (decreasing from top to bottom). For each plate the detachment forces is measured in Newtonian fluids of three different viscosities (50, 200, and 1000 cSt). The range for the y-axis is different for (a). Prior to detachment the plates were brought in contact with the lower surface using a force of 2N for 600 seconds in the same fluid as for the detachment. All samples are coated with a 20

μm layer of SU-8 photopolymer and bottom surfaces with CyTop flouropolymer to reduce adhesion caused by van der Waals forces.

We can use simple scaling arguments to relate the forces measured to the balance between flexural rigidity (EI) and viscosity (μ). We treat the top plates as Euler-Bernoulli beams where the lubrication forces (F_h) act as the distributed load, q(x,t) to obtain:

$$EI\frac{d^4h}{dx^4}=\mathrm{q}(\mathrm{x},\mathrm{t}) \ , \qquad (1)$$

$$\frac{F_h}{L}=-\frac{\mu L^3}{h^3}\frac{dh}{dt}=q(\mathrm{x},\mathrm{t}) \ , \qquad (2)$$

Where h is the fluid film thickness between the plate and the bottom surface, t is the time, and L is the nominal length of the sample in contact with the bottom surface (see Figure 2). We neglect inertial effects, assume initial boundary contact, small (<5°) deflection of the plate, and small deflection with the length of the plates throughout the detachment process. These assumptions allow us to use the local fluid film thickness as the beam deflection on the right hand side of Eq. (1), and to neglect the x-dependence of the lubrication forces in Eq. (2). In our experiments, the lubrication forces are measured via the deflection of a compliant load cell with an effective spring constant, k. Since the load cell is part of the mechanical loop, we need to introduce this force balance to describe our experimental system, as shown in Eq. (3):

$$F_H=k(vt-\Delta) \ , \qquad (3)$$

Where Δ is the displacement of the contactor at a given time such that the bracketed term in Eq. (3) is the deflection of the load cell. Instead of solving Eqns. (1)-(3) using an initial and four boundary conditions we perform dimensional analysis to extract characteristic time scales for the bending beam of Eq. (1) and for the lifting of the contactor in Eq. (3). If we use the fluid film thickness as the characteristic deflection in Eq. (1) we obtain a characteristic bending time ($\tau_{bending}$) from Eq. (1) given by:

$$\tau_{bending} = \frac{L^7 \mu}{EIh^3} \quad . \qquad (4)$$

Similarly, we can extract a characteristic time for lifting, $\tau_{lifting}$ the contactor from Eq. (3) as:

$$\boldsymbol{\tau}_{lifting} = \frac{\left(\frac{\Delta}{v} \pm \sqrt{\frac{\Delta}{v}^2 + 4\frac{\mu L^4}{kh^2 v}}\right)}{2} \qquad (5)$$

The total peeling time is the sum of these two processes $\tau_{peeling} = \tau_{bending} + \tau_{lifting}$, because the bending beam and the load cell are subjected to the same lubrication forces. However, the load cell and the portion of the plate interacting with the bottom surface move at different velocities so we relate both processes to the sample velocity using τ_{peeling}. Using this scaling argument we can relate the motor displacement ($v * \tau_{lifting}$) to the effective motion of the plate in the region where it is interacting with the bottom surface ($h / \tau_{peeling}$) by combining Eqns. (4) – (5).

Figure 4a shows the characteristic velocity of the plate in the region where it interacts with the bottom surface as a function of the motor displacement, calculated for the three bending rigidities studied here. As a point of reference and upper bound, the constant drive velocity of the motor is also shown in Figure 4a. For the three curves, we see that initially the plates move much slower than the motor and that the velocity increases until it reaches the motor velocity, at which point the plates are considered detached. As with the experiments, we observe the motor displacement necessary to separate a plate decreases with an increase in bending rigidity. For a given viscosity and drive velocity, the ability of the plate to bend will reduce the hydrodynamic force during detachment by facilitating a more gradual infusion of fluid during the opening of the gap between the plate and the bottom surface. The glass slide is almost a limiting case where detachment mainly occur via lifting (rotation with respect of the end of the pate) where final detachment occurs very abruptly (almost via snapping) once the force reaches its peak value. We can compare directly the dependence of the total motor displacement on bending rigidity using Eqns. (4)-(5) for the three fluid viscosities investigated here (Figure 4b). Generally, we find good agreement between the scaling argument and the experimental data except for the case of the glass slide. We suspect that the glass slide has a spring constant that exceeds that of the load cell and that due to its very high bending rigidity the glass slide cannot bend. It could probably be described better as a rigid rotating arm instead of a bending beam.

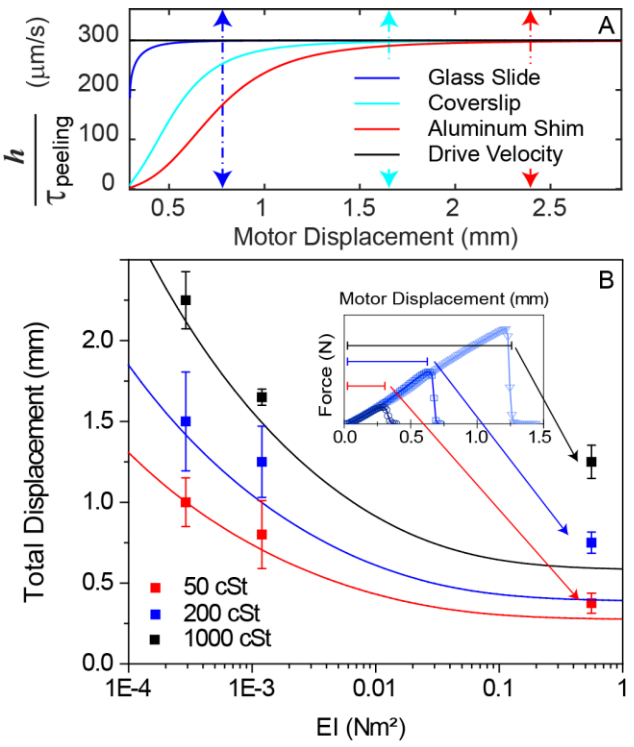

Figure 4.4. A) Characteristic velocity, $h/\tau_{peeling}$ of plates as a function of the motor displacement calculated for a viscosity of 1000 cSt, motor drive of 300 μm/s, with initial separation of 50 nm. Black line represents the constant motor drive velocity at 300 μm/s. The arrows represent the motor displacement where plates reach 99% of the motor velocity at which we consider the plates to be detached. B) Comparison of displacement required to detach plates (based on reaching zero forces in the force-displacement curves)

Using $\tau_{peeling}$, we can estimate the characteristic velocity of the sample as $dh/dt \sim h/\tau_{peeling}$. The lubrication force on a sample moving at this velocity is estimated as:

$$F \approx \frac{\mu L^4}{h^2} \frac{1}{\tau_{peeling}} , \qquad (6)$$

Since the force and motor displacement are linked spatially by h, instead of temporally, to find an experimentally relevant force versus displacement curve, we convert h to a motor displacement using equation 5.

The force-displacement curves can be evaluated for a range of $\tau_{peeling}$ to find the maximum force (F_{peak}), and the associated energy release rate, G for the detachment. We can then evaluate numerically, based on these scaling arguments, how the peak force and energy release depend on the balance between bending rigidity and viscosity. We find that the peak force scales as: $F_{peak} \propto \mu^{0.25}(EI)^{0.73}$ and the energy release rate as: $G \propto \mu^{0.5} EI^{0.28}$. F_{peak} and G can be linearized to EI/μ by multiplying by a scaling factor. For F_{peak}, we choose ζ = $EI^{0.27}/\mu^{1.25}$ such that F_{peak} ζ ∝ EI/μ and for G, we choose ξ = $EI^{0.72}/\mu^{1.5}$ such that Gξ ∝ EI/μ. These relationships can be compared to predictions for steady-state 90° peel tests. For example, Piau et al.[23] developed a full model and predicted that the energy release rate scales as $\mu^{4/7}$ $(EI)^{3/7}$ at a fixed peel angle of 90°. The work by Piau was a modification of the work by Kaelble[27] and Bikerman[28] that predicted a scaling as $\mu^{1/2}$ and $(EI)^{1/2}$ for variable peel angles, which include any realized peel angle that occurs during detachment from 0°. We see that for our small angle peel test the dependence of the energy release rate on the bending rigidity is weaker than for steady-state 90° peel tests, although the relationship between energy release rate in the 90° peel test is F/b, where b is the width of the sample. This difference occurs because the total sample displacement also depends on the rigidity, whereas the 90° test is peeled at a constant velocity and the displacement is not a function of the sample. Figure 5 compares our measurements of the peak forces and energy release rates to the predictions based on the scaling arguments. We see that the energy release rate follows $G \propto \mu^{0.5} EI^{0.28}$ for EI/μ spanning six orders of magnitude (Figure 5a). On the other hand, the peak forces do not follow the predicted scaling (the best-fit slope in Figure 5b is not 1.0). However, if we exclude the data for the glass slide (triangles in Figure 5b) the remaining data follows the predicted relationship.

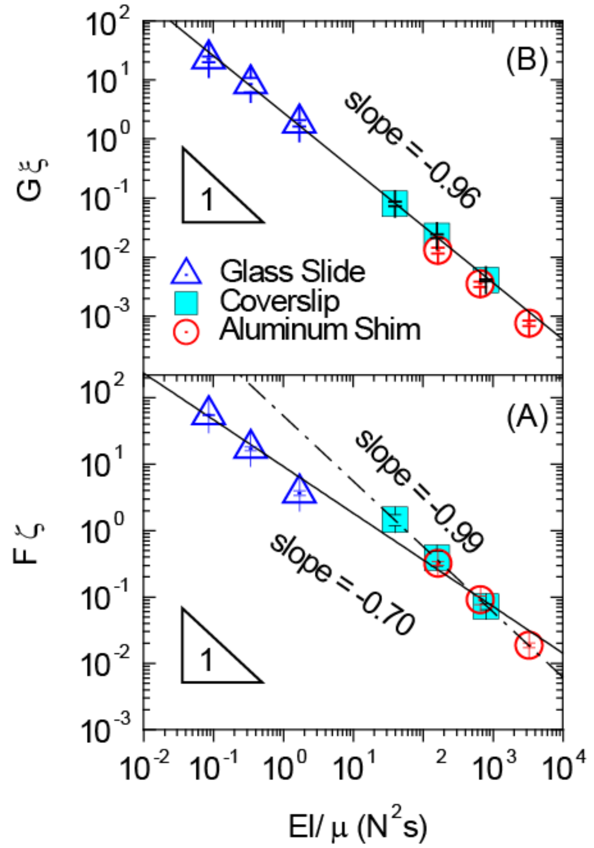

Figure 4.5. Scaled force and work versus EI/μ. The top graph (A) shows the scaled peak force in the force-displacement curves. (B) Shows the scaled entire work of separation from the integrated force-displacement curves. Dashed lines in (A) indicate slope with the glass slide data omitted. Samples repeated in triplicate and n ≥3. In both cases, the line represents the average scaling calculated from nine points (three rigidities at three viscosities).

To contrast the effect of the extensional compliance from that of the bending compliance we measured the forces to peel off plates with the same flexural rigidity but with different extensional compliance. To do this we created thick blocks of PDMS (4mm) such that their flexural rigidity ($EI = ELd^3/3$), where d is the thickness of the sheet and L is its full length) are the same as the one of a glass coverslip (middle panel in Figure 3). Shown in Figure 6 are the force-detachment curves for these two different plates taken at three drive velocities. We readily see that, for any drive velocity, the magnitude of the forces to peel the PDMS blocks (open symbols) are always smaller than the one required to peel the glass coverslips (filled symbols). We also find that for all drive velocities, the peak force is always larger for the glass coverslip than for the PDMS sheet, although it is only slightly higher at 600 μm/s. If we integrate the force-displacement curves to get a work of separation, or an effective energy release rate, G (see Figure 6b) we see that the work to detach the glass coverslips is always significantly larger than the one required to detach the PDMS sheet. Also shown in Figure 6b is the work of separation of glass coverslip with a thin (10μm) layer of SU-8. The data for this additional sample is presented to demonstrate that the presence of a thin (10um) layer of the photoresist SU-8 or PDMS on top of the glass coverslip is not sufficient to alter the detachment forces measured, even if the Young's modulus of SU-8 is significantly higher than the one for PDMS. In both cases the polymer films are too thin to deform[75] due to a normal load and they do not significantly alter the mechanical properties of the glass coverslip underneath.

Nearly all samples here share the same initial slope on the force-displacement plot. This is because these samples, even under different peel velocities, share the same system compliance (load cell compliance and bending compliance) during this portion of detachment. During the initial portions of the peeling process, the bending compliance is dominant over the extensional compliance, and since the rigidity of all these samples have been kept the same, the slope of the force-displacement curve is also the same. The peeling curve at 200 μm/s for the PDMS block, however, has a lower slope than the other force curves in Figure 6A. The PDMS block peels differently at 200 μm/s because the viscous forces are too low to bend the sample significantly compared to detaching by being simply lifted off the substrate. In another test, Patil et al. [39] have reported results where they were peeling glass plates adhered with semi-cured PDMS liquid to several different patterned PDMS substrates. They also found that for samples with very low adhesion, the force-displacement curve would exhibit a smaller initial slope, even though glass plates with a single rigidity were used across their experiments. It would seem that the extensional compliance has a conditional effect on the initial slope – if there is sufficient viscous force then it will not alter the initial slope and the slope will depend on the bending compliance and load cell compliance alone.

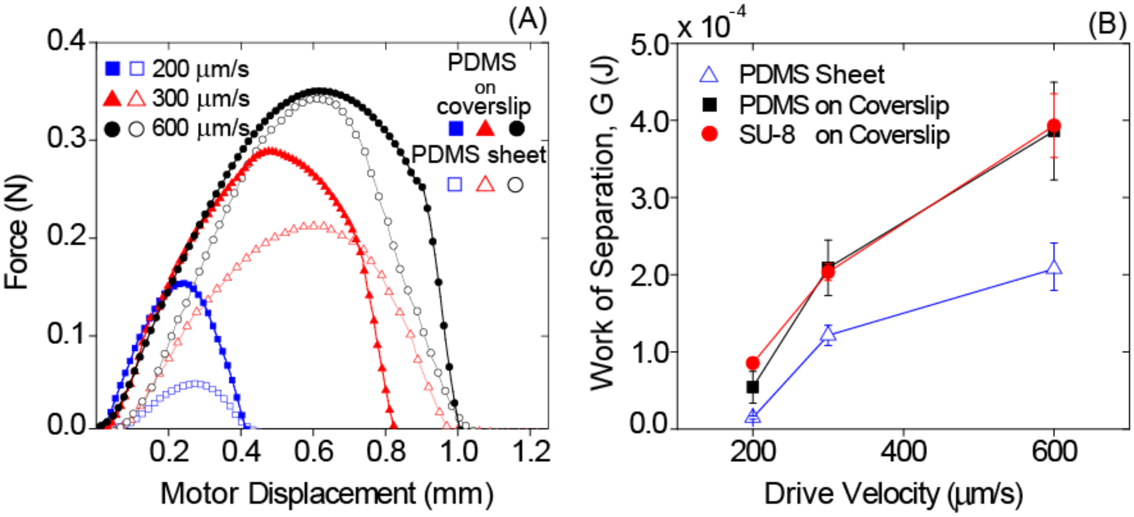

Figure 4.6. Force-displacement curves (A) and work of separation, G, (B) obtained from peeling samples with the same flexural rigidity (EI = 1.2x10^{-3} Nm^2) but different Young's moduli (PDMS Slab – 3.0 MPa[76], glass coverslip – 67 GPa[77]) and sample thickness (PDMS Slab – 3.8 mm, glass coverslip – 0.13 mm). The forces were measured in a Newtonian silicone oil with a viscosity of 200 cSt. The different symbols in (A) are for different drive velocities (200, 300 and 600 μm/s). Legend refers to the motor velocity in μm/s. Open symbols represent the PDMS sheets and the filled symbols are the coverslips coated with a 20-μm layer of PDMS. In (B) an additional set of data for the peeling of coverslips with a 20-μm coating of the photopolymer SU-8 is also shown to demonstrate that the modulus of the top layer on the coverslip does not affect the forces measured. Sample size on right is n = three, with each sample tested in triplicate.

We attribute this reduction to the extensional compliance, which was investigated in a similar system by Ghatak et al.[71] They developed an expression for the work required to lift a glass plate from an elastic substrate. To adapt their system, we make two assumptions. First, we assume that we can combine the elastic deformation and bending into our plate alone, instead of two separate elements. Second, since we measure purely viscous forces, instead of any conservative interactions, we apply this effect across the entire length of our sample, instead of only at the point of crack initiation.

They found that the elasticity of the substrate dissipates energy and reduces the forces by a factor *g*(aK) given as:

$$g(aK) = \frac{8(aK)^4(12 + 46(aK) + 72(aK)^2 + 56(aK)^3 + 21(aK)^4 + 3(aK)^5)}{3(6 + 12(aK) + 9(aK)^2 + 2(aK)^3)^3} \quad (7)$$

Where *a* is the distance from the contactor to the edge of the crack and K is the inverse of the stress decay length. The stress decay length is calculated as:

$$K^{-1} = \left(\frac{(EI)d^3}{12\, S_{shear}}\right)^{\frac{1}{6}} \quad (8)$$

Where S_{shear} is the shear modulus of the elastic film. The stress decay length corresponds to the area over which the stress is applied from the flexible beam onto the elastic film. Using Equation 8, the PDMS slab has a shear modulus of 0.25 GPa[78] while the PDMS coverslip has a shear modulus (Schott D263 glass) of 30 GPa [77] results in a stress decay length of 3.2 mm for PDMS sheet while the PDMS-coated coverslip is 0.26 mm. Since the PDMS layer on the coverslip is very thin, it does not contribute to the elastic deformation of the coverslip.[75] g(aK) must be evaluated for all values of a as the sample peels for both the PDMS sheet and coverslip to get an average $\bar{g}$(aK) (see Figure 7). Then we can relate the G between the two samples as:

$$\frac{G_{PDMS\ Sheet}}{G_{PDMS\ Coverslip}} \sim \frac{g(a * K_{PDMS\ Sheet})}{g(a * K_{PDMS\ Coverslip})} \quad (9)$$

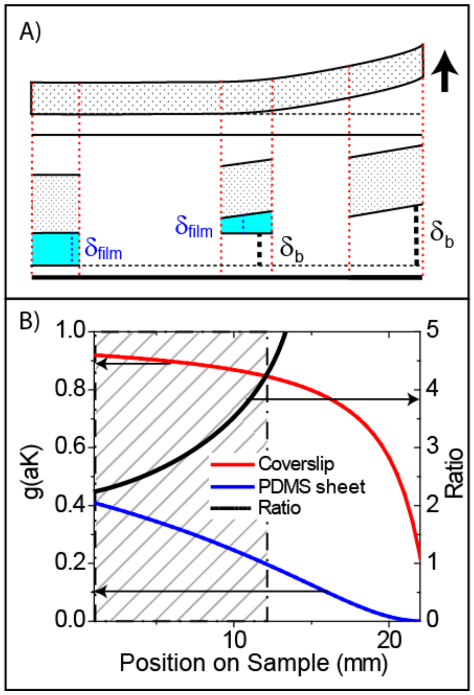

Figure 4.7. Effect of bending and extensional compliance through stress concentration. A) Schematic of the difference in compliance which arises due to the ability of the PDMS slab to indent or extend (extensional compliance) further than the PDMS-coated coverslip. The deformation due to bending is denoted as δ_b and the deformation from the extensional compliance is shown as δ_{film}. B) The effect of a multiplying factor, g(aK), on the overall work is shown as given by Ghatak et al..[71] The X-axis is schematically the same as in sample A) with the location of the contactor on the far right (at sample = 22 mm). The shaded region represents the portion of the sample that interacts with the bottom substrate and thus the unshaded region from 12 mm to 22 mm does not contribute to the adhesion.

The approach of Ghatak et al. is compatible with work taken in dry adhesive systems by Bartlett et al.[63] and Shull et al.[65] to selectively tune adhesive pads by altering their size and thickness. As seen in Figure 7B, the portion of the sample that interacts with the bottom surface is from 0 to 12 mm and the average value of the ratio between g(aK) of a PDMS sheet and the g(aK) PDMS-coated coverslip in this portion is 2.7. This compares relatively well to our average ratio of 2.8, as seen from Figure 4.6B, (across all velocities and comparing the PDMS slab to both the PDMS and SU-8 coated coverslips)

4.4. Conclusions

Within this paper, we have investigate the role of sample rigidity and compliance on viscous forces during peeling. We first examine how the sample rigidity and bath viscosity changes the detachment forces and G. We scale the peak force and G and find reasonable agreement, as long as the sample is not overly rigid. We were also able to predict the motor displacement required to detach the sample fully, which was complicated by the presence of a load cell. Again, these predictions were more accurate when the samples were not excessively rigid.

We then isolated the role of extensional compliance separately from the bending compliance by testing two samples with the same rigidity but different Young's modulus. We found that our results were explained by adapting a theory by Ghatak et al.[71] which was originally used to describe dry adhesives, even though our samples were only subject to purely viscous forces.

4.5. Supplemental Information

Achieving Boundary Contact

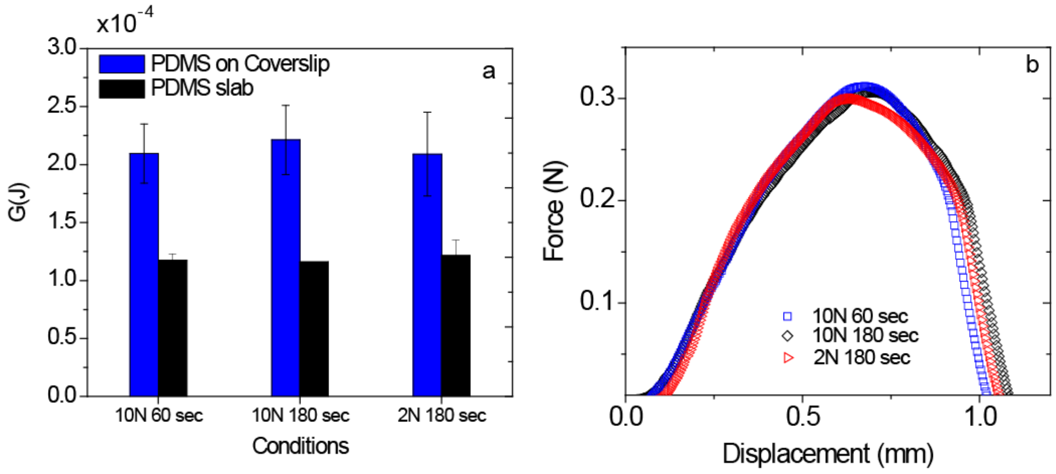

Figure 4.7. Work and forces with increased load during loading phase. Peel velocity is 300 µm/s and fluid viscosity is 200 cSt. These samples have been loaded at 10N (a 5x increase over the typical experimental conditions). In panel a, the work is shown and neither backing is statistically different between 60 and 180 seconds of loading. Representative force curves of a PDMS-coated coverslip are in panel b.

The loading conditions in the paper have been considered to be *plateaued* when they no longer increase with increased dwell time. The plateau occurs because the samples have reached boundary contact and can no longer reduce the film thickness between the sample and substrate. The relationship between film thickness and load, dwell time and viscosity is given as (assuming the surfaces start far apart):

$$h = \sqrt{\frac{\mu L^4}{2Ft}} \qquad (7)$$

Where *h* is the separation between the sample and bottom substrate, μ is the viscosity, L is the interacting length of the two square surfaces, *F* is the applied load and *t* is the dwell time.

We have established for this system, boundary contact occurs at 2 N/180 seconds. This can be seen in Figure 4.7. where we have dramatically increased the load to 10 N and loaded at 60 and 180 seconds. In panel a, we see the same work because the samples can no longer get closer to each other. As shown in Equation 1, increasing the load by a factor of five should be the same effect as loading for 5 times longer. Thus, the fact that 2N at 180 seconds gives the same results as 10N at 60 seconds and 10N at 180 seconds suggests that we are in boundary contact. However while 2 N and 180 seconds would yield a separation in 200 cSt (0.05 Pa*s) of 1.2 microns, even slighted tilted plates can accelerate the thinning of the gap.[37]

Panel b shows that the force-displacement curves are essentially identical between the three different conditions, confirming the trends in panel a.

Approximating the Hydrodynamic Drag as Parallel Plates

$$F_h = \frac{\mu L^4}{h^3}\frac{dh}{dt} \tag{8}$$

We look at the expression for the force to separate two parallel plates, which we have adapted to describe a bending plate. Although h is a function of x, we justify that h(x,t) ≅ h(t) in this equation.

As mentioned in the main text, h is the separation between the sample and the substrate, t is time, μ is the viscosity, and L is the length of the sample that overlaps with the substrate.

A Taylor series expansion shows that Equation 2 is justified when the separation, h (sub-micron to microns), divided by the L (12 mm) vanishes quickly for derivatives that scale as $(h/L)^2$ or $(h/L)^3$, and given that $L \gg h$.

Equation 25 is derived from the Reynolds equation (provided below)[79]:

$$\frac{dP}{dx} = L\frac{12\,\mu}{h^3}\frac{dh}{dt} \tag{9}$$

Where P is the pressure.

Substituting $h \cong h + dh/dx$

$$\frac{dP}{dx} = L * \frac{12\mu}{\left(h + h\frac{dh}{dx}\right)^3}\frac{d(h + \frac{dh}{dx})}{dt} \tag{10}$$

Terms $\left(\frac{dh}{dx}\right)^n$ for n=2, 3 can be ignored because they scale as H/L. H is at sub-micron lengths and L is 12 mm. Thus, H/L 1 and $(H/L)^n$ will be $\ll 1$.

Simplifying, we get

$$P\,dt = L * \frac{12\mu}{h^3} * d\left(h + h\frac{dh}{dx}\right)dx \tag{11}$$

The right hand side then simplifies further to:

$$\mathrm{P\,dt} = 12\mathrm{L}\mu\left(\frac{\mathrm{L}}{3\mathrm{h}^2} + \frac{\mathrm{h}}{3\mathrm{h}^2}\right). \tag{24}$$

Since we know that L≫h, the expansion simplifies to the expression for flat plates, $\mathrm{Pt} = \frac{4\mu \mathrm{L}^2}{\mathrm{h}^2}$ and further to $\frac{\mathrm{dh}}{\mathrm{dt}} = -\frac{\mathrm{Fh}^3}{\mu \mathrm{L}^4}$

Visualization of Detachment

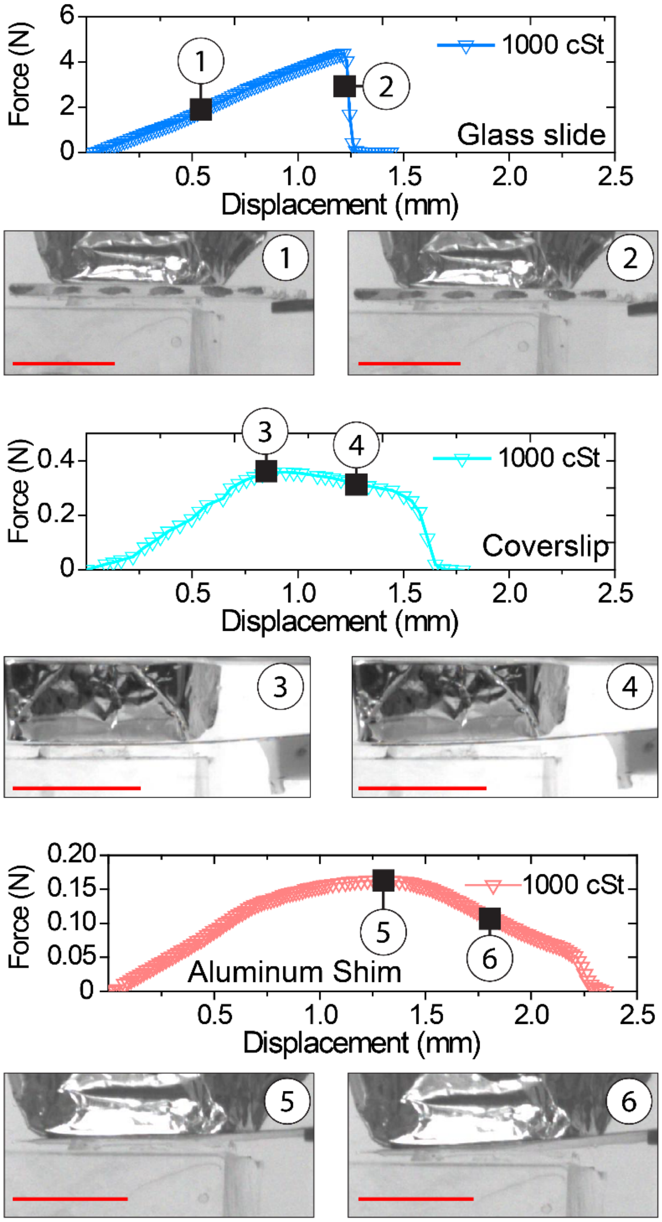

Figure 4.8. Visualization of peeling samples. The three different samples tested in this are shown in decreasing rigidity from top to bottom (glass slide, coverslip, and aluminum shim). Select images from the force displacement curves are shown to highlight near the peak force (when the sample begins to detach) and in between the peak force and complete detachment (to showcase crack propagation).

Chapter 5

Coupling between Surface Structure and Loading Conditions in the Viscous Contribution of Peeling

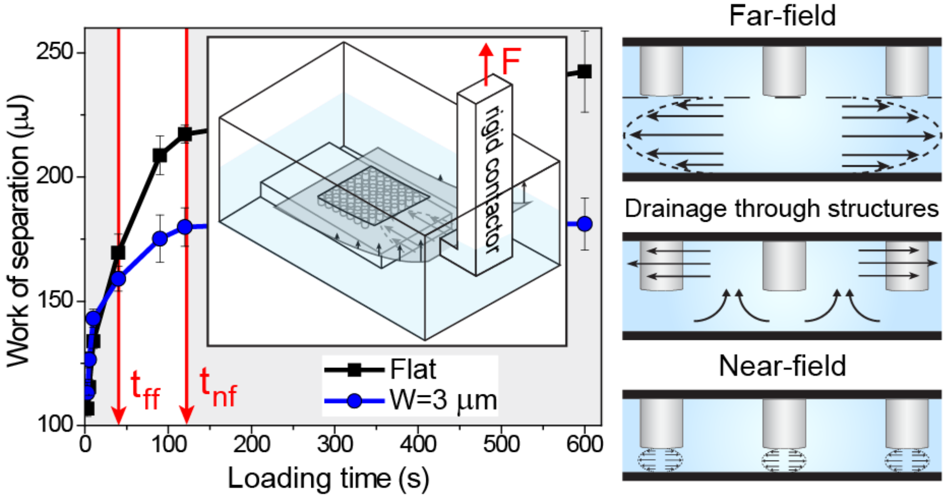

[This section has been reprinted with minor modifications with permission from: Dhong, C., & Fréchette, J. (2015). Coupled effects of applied load and surface structure on the viscous forces during peeling. *Soft matter*, *11*(10), 1901-1910.]

5.1. **Introduction**

Throughout nature, animals have taken advantage of structured surfaces to mediate their adhesion in dry, wet, and flooded environments. Tree frogs are an interesting case because they display good adhesion in all these conditions. In a completely flooded environment tree frogs have been shown to exhibit strong control over their locomotion, for example being able to move without slipping without interlocking supports.[2, 13, 52, 80, 81]

They have also been shown to adhere upside-down under flowing (5 mL/min to 4L/min) water.[2] A key feature that enables this control is suspected to be the structured hexagonal array of epithelial cells on their toe pads. The epithelial cells have a soft (5-15 MPa), keratinized outer layer[12] and form pillars on the toe pads that are approximately 10 μm in diameter, 10 μm deep and are separated by 1 μm, and mucus is secreted through these channels to enhance adhesion.[82, 83] The role of the channels in completely flooded environment, however, is not well-understood. The spacing between the epithelial cells creates an interconnected network of channels that has been hypothesized to aid in the removal of fluid from the toe pad, reducing the hydrodynamic repulsion and as a consequence reduce the time necessary to make contact.[13, 81] The interplay between surface structure and hydrodynamic interactions has implications in several fields[53] beyond the understanding of tree frog adhesion. For example, in the design of structured surfaces for drag reduction in underwater propulsion[84], for the flow and solute transport through cracks in hydrofracturing[85], in the design of tire treads to prevent hydroplaning[86, 87], or to minimize viscous losses in micro- and nanoscale resonators that operate in fluid environments[88, 89]. Micro- and nanoscale roughness or structure also dictate slip at the solid-liquid interface.[90, 91]

To understand how topography can modulate the force to separate surfaces in flooded environments, it is important to consider a peeling motion during detachment since many animals, including tree frogs, detach in a peeling mode.[1] During peeling, the detachment occurs by gradually increasing the peeling angle as a crack propagates across the toe pad. Structured surfaces offer multiple advantages when trying to modulate peeling forces, they can blunt the crack front[92] or force the arrest of crack propagation at feature boundaries[26]. Detachment via peeling is also desirable because the adhesion force can be modulated by varying the peel angle.[29, 93-95] Geckos[8] and tree frogs[80] have both been shown to splay their limbs to control their adhesion to surfaces where the peel angle is kept low to maintain contact and increased to pull out. In biomimetic systems, the effect of structured surfaces on peeling has been well-studied in dry[25, 71, 72] and wet[39, 72] environments, but less so in completely flooded conditions.

The coupling between approach and pull out is another important characteristic that needs to be considered to understand detachment between surfaces under flooded conditions. In contrast to the adhesion force measured in air where there is negligible work necessary to make contact, viscous forces are present when submerged in fluid and affect both approach and pull out, especially if it is necessary to make contact rapidly. For example, significant viscous drag can prevent surfaces from reaching contact quickly or would require a significant applied load.[79] The viscous force required to move two flat surfaces in a fluid is described by the Stefan equation (Eqn. 1)[96], which can be derived from Reynolds' theory[34] and has been solved for several plate geometries[79], including in the presence of misalignment such as tilt[37]. In the context of work required to separate surfaces in flooded environments, the initial loading sets the fluid film thickness prior to pull out, and as a consequence influences whether or not conservative contact forces are present and the magnitude of the viscous forces during pull out. Therefore, when investigating the role of surface structure on the work required to separate surfaces, it is important to control for the loading conditions to decouple its effect from that of the surface structure.

Under flooded conditions, the presence of surface structure can have profound effects on the work and time required to make contact. For instance, the spacing between surface features can facilitate drainage and reduce the repulsive hydrodynamic forces present when two surfaces are brought together in a viscous fluid.[35,97] A scaling argument, initially proposed by Persson[35], relates the decrease in time to contact to the feature sizes via a single length scale (h_o), a parameter that captures the key dimensions of the surface features. A similar argument can be reached from an effective permittivity and Darcy's law using a porous media analysis.[98-100] According to this limiting scaling argument (see Section 2), if the fluid film thickness is larger than h_o the fluid drainage is radial, there is no flow through the surface features, and the viscous forces are the same as the ones for flat surfaces. For fluid film thickness smaller than h_o, the fluid drainage goes through the surface features and the viscous forces are lower than the ones for smooth surfaces. We previously verified experimentally this scaling argument for the cross-cylinder geometry via the direct measurement of the hydrodynamic force between a flat and a structured surfaces in the surface forces apparatus (SFA).[97]

There are multiple reports on the role of surface structure on the detachment forces in viscous fluids. An enhancement in the detachment force was observed when peeling a surface patterned with an array of PDMS posts in a viscoelastic fluid.[39] It was suggested that the origin of the enhancement in adhesion energy was due either to viscous dissipation, crack blunting, or anchoring of the fluid to the structure. Measurement by Drotlef et al. [101] of the adhesion and friction forces of elastic micro-structured surfaces in fluids showed that the presence of surface features increased the friction forces, possibly due to boundary contact being facilitated by drainage through the surface structure. They also observed that an increase in fluid viscosity had no effect on the force and concluded that there were no viscous contributions to the peak in the adhesion force. In the case of oil capillary bridges on top of micro-pillars, it has been predicted that for pillars larger than 10 μm the major contribution to the adhesive force should be both viscous and the contribution from the Laplace pressure in the liquid bridge.[102] There have been many instances when investigating structured surfaces where viscous contributions have been considered[39, 101-103] but there is a need to isolate the viscous contributions from other effects such as capillary or van der Waals interactions, and elasticity of the surfaces[104]. Moreover, one common features of the previous reports is that the detachment force is tested after the sample has been brought into contact with a substrate without control for the loading conditions or the time necessary to make contact. The loading conditions (viscosity, applied load, and loading time) dictate the fluid film thickness prior to pull out and, in turn, the work required to separate the surfaces.

Here we detail our investigation of how the interplay between surface structure and loading conditions affect the viscous contribution in a peeling mode. We use rigid structured surfaces in Newtonian fluids and control the fluid film thickness prior to pull out by varying the viscosity, applied load, and loading time during approach. By following this protocol we can compare the work of separation for identical loading conditions to isolate the effect of surface structure. We observe that the presence of surface features facilitate contact and decrease the work of separation. We discuss our results in the context of the scaling of the lubrication approximation for structured surfaces.

Effect of surface structure on the fluid film thickness during approach.

Consider the approach between a surface with a periodic array of pillars and a smooth wall in the lubrication limit, where the fluid film thickness can be described by the Reynolds equation. We assume that the surfaces are rigid, that inertial effects are negligible ($Re < 1$), and that the plate area is much larger than the fluid film thickness. We follow the analysis of Persson[35] and hypothesize the presence of three different limiting regimes for fluid flow, illustrated in Figure 1. First, at large separations (short times) there is a far-field regime where the fluid flows radially and not through the structure. Second, as the separation decreases further the pressure in the gap increases and becomes sufficiently large to favor fluid flow through the structure instead of radially. As a consequence, preferential drainage of fluid through the structure yields smaller fluid film thickness for a given loading time than predictions based on smooth surfaces. Finally at small separations the hydrodynamic interactions with individual pillars dominate, and we recover the Reynolds equation but for an array of individual pillars (effective lower surface area). We denote this final stage the near-field regime. Therefore, as a fluid film thickness decreases during approach there should be a transition between radial flow and flow through the surface features. In the limit where the pillar height is much greater than the channel width ($D>>W$ in Figure 3) the thickness of the fluid film thickness necessary for this transition can be estimated as $h_o = W\left(\frac{D}{W+d}\right)^{1/3}$, see Table 1. We previously characterized this transition[97, 105] and its relationship with h_o for the hydrodynamic force present in the approach between a surface with a hexagonal array of cylindrical posts and a smooth surface. The experiments were performed in the Surface Forces Apparatus with curved surfaces in the cross-cylinder geometry.

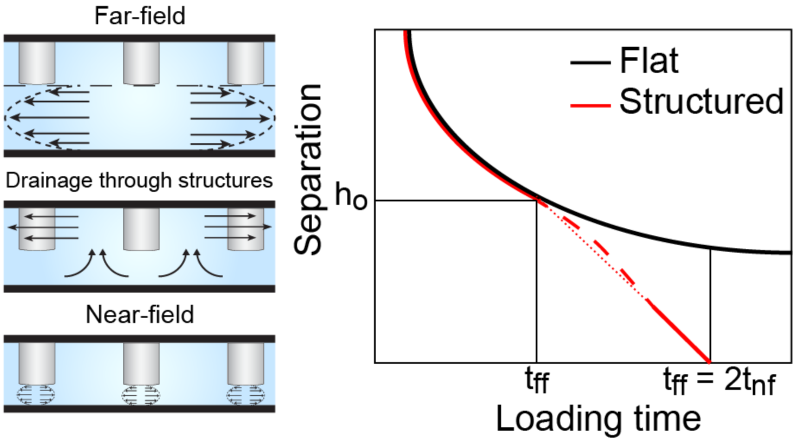

Figure 5.1. Schematic of the change in separation with loading time for a smooth and structured surface. The dashed line represents an interpolation between two regimes.

The scaling arguments derived in Ref [35] relates the characteristic times for the different flow regimes illustrated in Figure 1 to the surface features and loading conditions. First in the far-field regime the fluid flow conditions are the same as for a smooth surface with the fluid film thickness determined from the top of the posts. The change in the fluid film thickness is then obtained from the Stefan equation (Eqn. 1). The Stefan equation describes the instantaneous velocity (dh/dt) when two flat plates of area A separated by a fluid film of thickness h are brought closer under an applied load (F_N) in a fluid of viscosity μ.[35, 96] We hypothesize that the change in separation can be described by Eqn. 1 until the film thickness reaches h_o at the end of the far-field regime (at t = t_{ff}). We obtain t_{ff} by solving Eqn. 1 for the case of a constant F_N and plates that are initially very far apart to obtain a relationship between the loading time, t, and the instantaneous surface separation, fluid film thickness h, and then set the separation to h_o to find the limit of the far-field regime (t_{ff}), see Eqn. 2.

$$\frac{dh}{dt} = -\frac{F_N}{2\mu A} h^3 \quad (1)$$

$$t_{ff} \cong \mu \frac{A^2}{F_N} \frac{1}{h_o^2} \quad (2)$$

We can predict the onset of the near-field regime (t_{nf}), with the assumption that once h_o is reached the fluid flow is only through the structure and independent on the fluid film thickness. By using Eqn. 1 with a constant $h = h_o$ at all times on the right hand side and with the boundary condition that at $t=t_{ff}$, $h=h_o$ we can find the time necessary to reach boundary contact (in the limit where $t=t_{nf}$ at $h=0$), given by Eqn. 3. However, more realistically in the near-field regime the hydrodynamic interactions between individual posts and the surface would dominate at small separation and lead to dh/dt to decrease asymptotically as the fluid film thickness decreases, preventing boundary contact.

$$t_{nf} \cong \mu \frac{A^2}{F_N} \frac{1}{h_o^2} + t_{ff} = 2t_{ff} \quad (3)$$

Therefore based on Eqns. 2-3 we would predict that 1) the limit of the far-field regime is inversely proportional to h_o^2, and 2) the time to reach boundary contact (t_{nf}) should be twice the time spent in the far-field regime for any surface structure.

5.2. Experimental Details.

Sample Preparation. All the samples investigated consist of 20 μm of SU-8 2007 (MicroChem) supported by a glass coverslip (Schott D263M, 22x22 mm, 0.13-0.16 mm thickness). The structured surfaces have features only on the top 10 μm that consist of cylindrical pillars in a hexagonal array (see Figure 3 and Table 1). For all the samples the final SU-8 thickness is achieved in two sequential 10 μm coatings on coverslips. Traditional microfabrication techniques are used to pattern the surface features. First, square glass coverslips are cleaned using an isopropyl alcohol/ethanol rinse followed by a dehydration bake at 200° C for 10 minutes. Then a layer of SU-8 2007 is spin coated at 1700 rpm for one minute to produce a 10 μm thick layer. The square substrate requires manual edge bead removal with a razor blade, which is followed by a pre-exposure bake on a hot plate at 95° C for 3 minutes and then exposure to a UV light at 140 mJ/cm^2. The base layer requires no mask or developing and the sample is hard-baked at 200° C for 10 minutes immediately after exposure. After cooling, a second layer of SU-8 is deposited using the same steps as the initial layer, but a chrome mask is used during the exposure step to create the surface patterns and a simple transparency mask is used for the smooth surface. For all the samples, the feature area is 14 mm x 14 mm and thus does not cover the entire coverslip substrate surface. Effort was made to manually center the mask with the coverslip, but there is sample-to-sample variation of order 1 mm from the edge of the patterned region to the edge of the coverslip. UV exposure is followed by a post-exposure bake at 95° C for 5 minutes and then immersion in SU-8 developer for 3 minutes with gentle manual agitation. Samples are then rinsed in isopropyl alcohol and hard baked at 200° C for 10 minutes. Pattern formation and layer thicknesses are verified using confocal imaging and profilometry. The bottom surface in the peeling experiments consists of a glass coverslip onto which a thin fluoropolymer layer of 1.55% CyTop (Bellex International Corporation) is spin coated at 5000 rpm for one minute and then annealed in an oven for 15 minutes at 180°C.

Materials. The fluids in the bath are Newtonian silicone oils (PMX-200, Xiameter). Two viscosities are investigated, 200 cSt (0.965 g/mL) and 1000 cSt (0.968 g/mL). The silicone oils were used as received. The combination of rigid SU-8 as the surfaces and silicone oils as the fluid, along with working under completely flooded conditions allow us to neglect other type of interactions such as van der Waals, electrostatic, capillary. The Hamaker constant a SU-8 – Silicone Oil – CyTop system is negligible, see ESI for estimates of the Hamaker constant and interfacial energy.

Peeling Apparatus. A custom-built peeling apparatus, illustrated in Figure 2, was designed to measure the force required to peel the samples in a completely flooded environment for different loading conditions. The apparatus is based on the designs of Ghatak et al.[25]. The experiments are performed in two distinct, but continuous, phases inside a bath filled with fluid. An overview of the key features of the apparatus and experimental protocol is described here, with additional details available in the ESI.

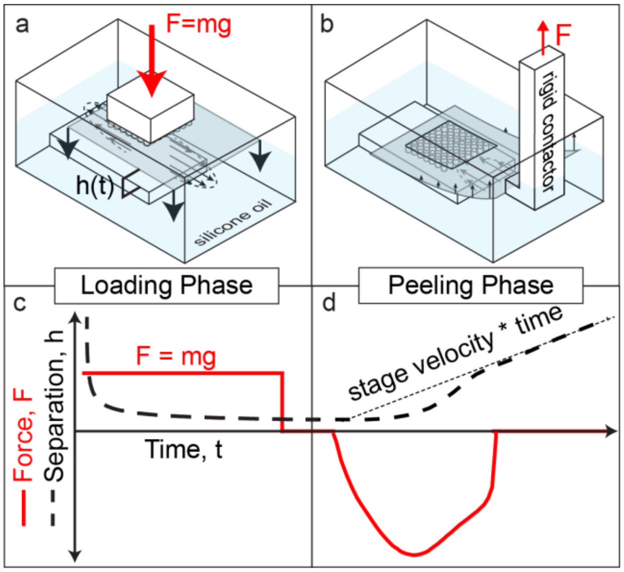

Figure 5.2. Schematic of the peeling apparatus. (a) Loading phase where a normal load is applied to decrease the fluid film thickness between the sample and bottom substrate. (b) Peeling phase where one side of the sample is moved upward by a rigid contactor driven by a motorized stage and mounted onto a load cell. (c) Illustration of the change in the fluid film thickness (separation) due to the applied load as a function of time during the loading phase. (d) Illustration of the change in separation[31] (fluid film thickness) and measured force during the peeling process. The difference in the contactor velocity and the motor velocity gives rise to a force measured by the load cell. The fluid film thickness (separation) in (d) varies spatially and is largest on the side near the contactor.

Loading phase. First, in the loading phase the surfaces are initially far apart (approx. ~500 μm) and a fixed mass (0.05kg or 0.208kg) is applied on the top surface as a weight for a set amount of time (Fig. 1a, c). The constant load brings the top surface closer to the bottom surface and sets the fluid film thickness prior to the peeling phase. Therefore we control the sample-to-substrate separation prior to pull-out by changing the viscosity, the applied load, and the loading time. In the current experiments the separation between the sample and the bottom surface cannot be measured directly. There is also always a small tilt present between the two surfaces, even after careful effort to align the surfaces. A small tilt can significantly decrease the fluid film thickness from that predicted for a smooth falling plate in the lubrication limit.[37, 79] Therefore we report the loading conditions (viscosity, loading time, and applied load) as an indication for the fluid film thickness prior to measurement of pull out forces rather than absolute values of film thickness. The weight is lifted within three seconds after the end of the loading phase and the peeling measurements are performed (Figure 2b, d).

Peeling phase. Once the weight is pulled away from the back of the coverslip, the peeling phase starts. In the peeling phase, the flexible coverslip (flexural rigidity = 0.03 Nm) is peeled off the substrate by a rigid contactor moving at a constant drive velocity of 300 µm/s and connected to a load cell. As viscous forces scale with the velocity, we selected 300 µm/s as the drive velocity to exploit the full range of the load cell while remaining in the lubrication regime. While the drive velocity is constant, the actual velocity at which the sample and substrate separates is less than the drive velocity because of the hydrodynamic drag, and varies both with time and position. As an upper bound, we estimate the Reynolds number to be Re <1 based on a film thickness of order microns, a length of 14 mm, and a peeling velocity less than 1mm/s. Throughout the peeling process the bending of the coverslip remains in the small angle limit (<5°). In this limit we do not have to consider the potential energy from the movement of an inextensible film with an applied force.[38]

Additional possible contributions to the forces measured are the elasticity of the coverslip during bending, the viscous forces from the fluid film, the compliance of the polymer film, and the conservative surface forces (such as van der Waals interactions)[38-41]. In our system there is negligible contribution from conservative surface forces (e.g. electrostatic or van der Waals interactions), and the SU-8 polymer film employed here is non-compliant (E=5.6 GPa)[106]. If we consider the two remaining contributions: the elasticity of the coverslip and the viscous contributions, we find that by using a rigid backing[23] the elastic work term is much smaller than the viscous work[38]. An estimate of the bending contribution is ≪1% of the entire work (since the elastic stress term is usually much smaller than the Young's modulus) and is thus negligible.[25, 39]

5.3. **Results and Discussion**

We conducted the peeling measurements in fluids of two viscosities, two masses acting as weights for a range of loading time that vary between 5-800 s. We therefore explore a range of loading conditions of viscosity/(mass ∗ loading time) that spans over three orders of magnitude (from $2x10^{-2}$ to $6x10^{-6}$ cSt/kg*s). This quantity is proportional to the square of the predicted film thickness for a flat surface. Since we expect the onset of different regime behaviors to depend on separation set by the substrate, we pick a maximum range of loads that can reliably be supported by our apparatus. The magnitude of the hydrodynamic forces will depend on the velocity, but based on our prior work[97] we would not expect the velocity to change the alter the contribution of the surface structure to the drag force in a low Reynolds number regime.

Three sets of samples were fabricated, the first two have surface features consisting of a hexagonal array of cylindrical pillars and the third is a flat surface that acts as a reference and control (see Fig. 3). The two structures investigated are identical in all dimensions except for their channel width (3µm and 10µm), the dimensions of the surface features are listed in Table 1. Also listed in Table 1 is h_o, which represents predictions for the fluid film thickness at the transition between radial fluid and drainage through the structure (see Section 2). This parameter is derived from a scaling argument in the lubrication limit (inherently 2D), and as such assumes a limiting geometry in the remaining dimension[35]. Our structures are not in such limiting geometries so we give a range of h_o in Table 1 – one determined by the width of the channels and one by the diameter of the posts.

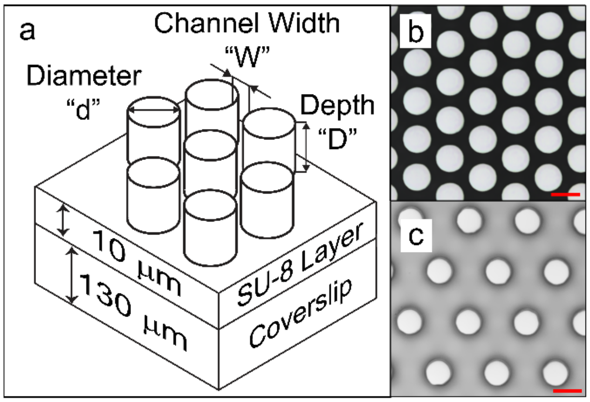

Figure 5.3. (a) Schematic and (b,c) optical microscopy images of the structured surfaces investigated. The scale bar corresponds to 10 µm. In (b) d=D=10 µm, and W=3 µm, in (c) W=D=d=10 µm.

Table 5.1. Feature sizes and estimates of h_o for the samples investigated.

Sample	Thickness (µm)	Diameter, d (µm)	Depth, D (µm)	Width, W (µm)	$h_o=W\left(\frac{D}{W+d}\right)^{1/3}$ (µm)	$h_o=D\left(\frac{W}{W+d}\right)^{1/3}$ (µm)
Flat	20	N/A	N/A	N/A	N/A	N/A
W=3 µm	20	10	10	3	2.8	6.1
W=10 µm	20	10	10	10	8.0	7.9

Force Curves. Representative force curves for the range of loading conditions investigated here are shown in Figure 4. We see that for all loading conditions and samples, the measured forces display the same qualitative features: the forces rise rapidly, reach a peak, and drop abruptly. These general features are qualitatively similar to the ones observed for other peeling[39, 107] and normal force measurements[31, 74] in viscous fluids with smooth surfaces. In the force curves, the position and magnitude of the peak forces are instrument specific and characteristic of the load cell employed. The effect of a compliant load cell on the measurements of a viscous force has been studied in multiple systems before, including probe tack measurements[74] and the surface force apparatus[31].

Introducing structured surfaces tends to decrease the magnitude of the force measured. This observation is in sharp contrast to previous work reported in the literature for the peeling force in the presence of a structured surface in fluid environments. It has been suggested that surface features could enhance the peeling force through increased viscous dissipation or by anchoring liquid bridges.[39] Our experiments with rigid structured surfaces rule out the viscous flow hypothesis and suggest that either anchoring of the fluid or elasticity of the structured surface is necessary for the enhancement of peeling force. For the portion of the force curves past the force peak, we observe an abrupt decrease in the measured force.

This portion of the force curve is attributed to crack propagation (see ESI). For soft patterned surfaces it has been observed that the force decreases and then reaches a plateau, which has been attributed to cavitation[108] or fingering instability (Saffman-Taylor[39] or elastic[14]).[109] Here we do not clearly see such features because no interface with a different viscosity is present in a completely flooded environment (no Saffman-Taylor type instability) and the high modulus of the SU-8 also hinders the formation of elastic instabilities. We also do not observe features that are consistent with cavitation because either the stress on the fluid film is not sufficient to induce cavitation or we are unable to resolve cavitation in our force curves. Finally, we do not observe a characteristic sequence of peaks that is typical for a series of crack arrest and propagation events caused by the surface features that have been observed in the absence of fluid.[16, 25, 110, 111] In most cases investigated here the two surfaces are not in contact; second we are working in a non-adhesive system (SU-8/silicone oil/fluoropolymer) and the stress decay length in fluids would be essentially zero and these peaks are visible when the spacing of patterns is of order the stress decay length[111]. Our observations are in agreement with the work of Patil et al.[39], where no sequence of crack arrest peaks are observed in a similar fluid experimental system.

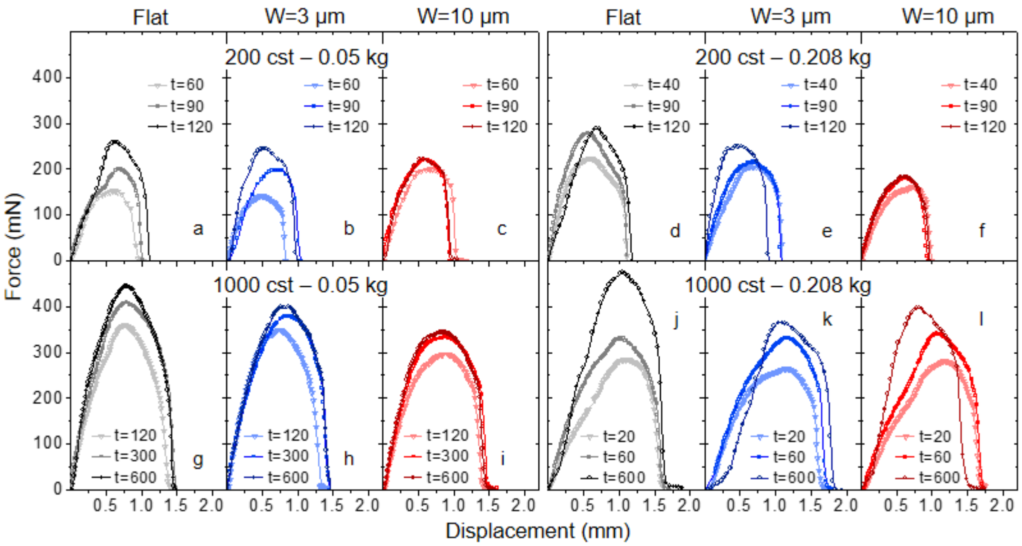

Figure 5.4. Representative force curves for the different loading conditions investigated. The structures investigated are the same for each columns. Time represents the loading

time (in seconds) from the loading phase. The displacement refers to the motor displacement during the peeling phase.

Several features in the force curves, such as the effect of the load, loading time and viscosity, are self-consistent and in agreement from predictions in the lubrication limit. In all samples, the magnitude of the force increases with increasing applied load and loading time, except for the W=10μm surface in 200 cSt - 0.208 kg (Fig. 4f), where increasing the loading time has a very small effect on the force curves. The intial increase in the force before the peak is reached has been shown to depend both on the rigidity of the system and the moment arm from the rigid contactor to the structures.[71, 112] The rigidity of all our samples is the same, but the structures have slight (~ 1 mm ≅ <5%) variation in positioning from the edge of the coverslip. This misalignment, combined with slight variations in apparatus placement of the rigid contactor, alters the moment arm and leads to sample-to-sample variations in the force curves. For example, in Figure 4g-i, the force curves are all from a single sample within an individual panel, illustrating the similarity in the force profile when the alignment is the same. In contrast, the force curves in Fig. 4j-l, come from two different samples, illustrating the effect of different moment arms and sample-to-sample variations.

Work of Separation. For all the force curves we integrate the force versus motor displacement to obtain a work of separation for the two interacting surfaces (Figure 5). Studying the work of separation is convenient because 1) in contrast to the force curves it is not instrument dependent, the work is unaffected by the compliance of the load cell[31], 2) it captures the viscous forces for the whole separation process and not only the initiation or propagation of a crack, and finally 3) it is unaffected by small differences in the moment arm. We want to distinguish this work of separation from the work of adhesion, the latter being a thermodynamic quantity based on conservative forces, whereas the viscous forces investigated here are dissipative.

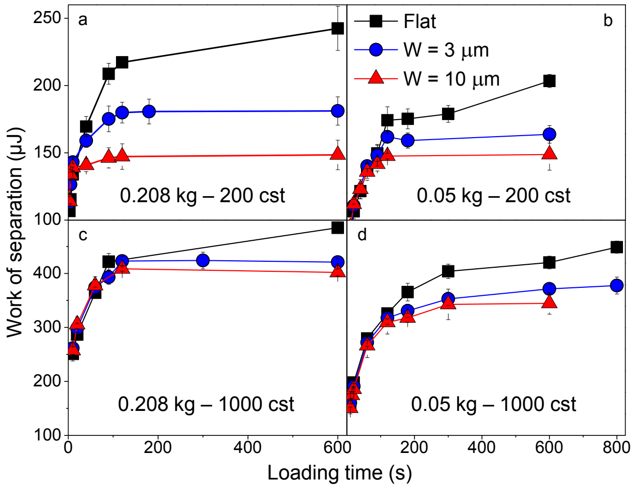

Figure 5.5. Work of separation as a function of loading times. Each panel corresponds to a different combination of viscosity and applied load. Each data point represents at least three different samples tested in triplicate.

In Figure 5 the work of separation is plotted as a function of the loading time. For an individual panel an increase in loading time should lead to a decrease in the fluid film thickness prior to pull out. We observe that increasing the viscosity, for the same applied load and loading time, leads to an increase in the work of separation. Two factors have to be taken into consideration to explain this observation: 1) the effect of viscosity in setting the fluid film thickness prior to peeling, and 2) the differences between normal and peeling motion. First, if we only consider normal motion for both approach and retraction, there should be no effect of viscosity on the work of separation for the same loading conditions.

This is because the viscosity dependence of both the drag force that sets the fluid film thickness prior to pull out and for the drag force during retraction cancels out for normal motion. The same is expected if we take into account the compliance of the load cell and model our system as a spring (the load cell) in series with a dashpot (the hydrodynamic force of the interacting surfaces).[31] In the case of peeling, previous theoretical work[23,27,28] predicted that the drag force depends on $\mu^{1/4}$ compared to being proportional to μ for normal motion. This weaker dependence of the drag force on viscosity when going from a normal to a peeling motion can therefore explain the increase in the work of separation with viscosity for the same applied load and loading time. The approach-detachment cycle is no longer reversible due to the difference in the mode of motion. This leads to a lower work of separation required to separate surfaces via peeling.

For a given fluid viscosity and applied load, the work of separation initially increases rapidly with loading time and then slows down or even reaches a plateau at long times. In the case of the flat surface a plateau in the work of separation is not typically observed (see Fig. 5d). In contrast, for the two structured samples, the work of separation reaches a plateau. For W=10 μm, the plateau is first observed at shorter loading times than for the W=3 μm surface. We also see that for each panel, the work of separation at long times decreases when going from a flat surface to the W=3 μm surface, and then to the W=10 μm surface. Another clear feature is that for a given viscosity and applied load the work of separation at short loading times is the same for the three surfaces investigated.

We describe the dependence of the work of separation on loading time for the structured surfaces based on the two characteristic times introduced in section 2 (t_{ff} and t_{nf})

and illustrated in Figure 1. First, for a given viscosity and applied load we find the longest loading time for which a structured surface has the same work of separation as the flat surface, which we denote t_{ff}, the limit of the far-field regime. Second, for a given structured surface we find the loading time at which the plateau in the work of separation is first observed and denote it t_{nf}, the onset of the near-field regime. The values for t_{ff} and t_{nf} are listed in Table 2 and were determined for each panel in Figure 5. For a quantitative determination of the two characteristic times, we employed the Wilcoxon rank sum method[113] (threshold of P=0.05 in all cases except P=.06 for t_{ff} of W= 10 μm 1000 cst 0.05 kg). To determine t_{ff} the method was employed to find significant differences between the work of separation between a flat and a structured surface. To determine the onset of the plateau region, i.e. t_{nf}, the method was employed to find the loading time at which an increase in loading time no longer leads to an increase in the work of separation.

Table 5.2. Values for t_{ff} and t_{nf} for the two structures.

Loading conditions		**W=10 μm**		**W=3 μm**	
viscosity	**mass**	**t_{ff} (s)**	**t_{nf} (s)**	**t_{ff} (s)**	**t_{nf} (s)**
1000 cSt	0.05 kg	120	300	180	300
	0.208 kg	60	120	60	120
200 cSt	0.05 kg	60	90	90	120
	0.208 kg	10	40	40	90

The presence of a plateau for structured surfaces at long loading times in Figures 5-6 suggests that boundary contact is reached in the near-field regime. In contrast to the structured surfaces, we did not observe a plateau in the work of separation as the loading time is increased for flat surfaces. For smooth surfaces and considering only hydrodynamics during approach, dh/dt asymptotically decreases as h decreases. Therefore, boundary contact should not be reached and the work of separation should keep increasing with loading time, which is what we observe for flat surfaces. It is found, however, that surface roughness[114], or certain geometries[115] are often sufficient for the fluid between two surfaces to squeeze-out and the surfaces to reach contact[114, 116,117, 118] in a finite amount of time. In the absence of surface deformation, if surfaces reach boundary contact, any longer loading should not change the work of separation. Therefore based on the fact that we observe a plateau in the work of separation we suspect that boundary contact is achieved at (or near) t_{nf} for the structured surfaces.

We aim to relate the characteristic loading times to the feature dimensions reported in Table 1 and to the flow regimes outlined in Section 2. We assign the characteristic times in Table 2 to the loading time spent in the far-field regime (t_{ff}) and to the onset of the near-field regime (t_{nf}), see Figure 6. The difference between the two loading times would represent drainage through the structure. By looking at the t_{ff} values in Table 2 we see that, for a given structure, increasing the load or decreasing the viscosity lead to shorter times in the far-field regime, consistent with reaching a fluid film thickness of h_o more quickly with larger applied load or lower viscosity. We also find that increasing the load and decreasing the viscosity leads to shorter time to contact, consistent with contact facilitated by drainage through the structures. If the structured surfaces reach contact while the flat ones do not could also explain why the work of separation is less for the structured surfaces. Finally, we also observe instances where the work of separation for a structured surface has not yet reached a plateau, is still increasing with loading time, but is less than that of a smooth sample (see the drainage region of Figure 6). We suggest that the presence of this region could imply that the drag reduction due to surface structure is more significant in the peeling mode than that in the normal mode, consistent with flow perpendicular or parallel to cylinders.[119, 120]

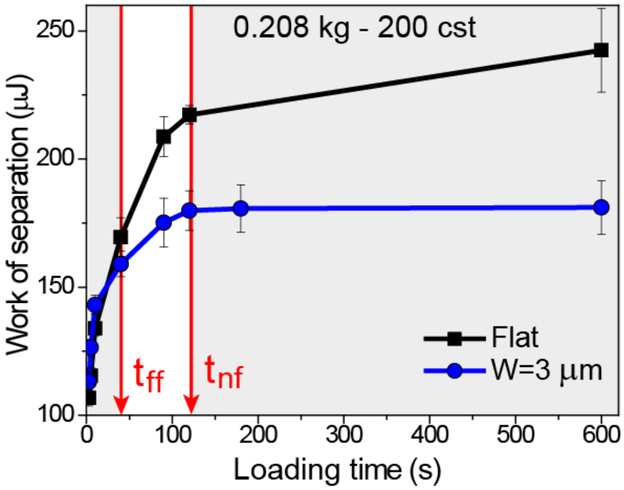

Figure 5.6. Identification of the three regimes from the work of separation as a function of loading time. A schematic of the fluid flow characteristics in each regime is shown on the right. Note that the t_{nf} and t_{ff} are not an interpolated value but determined based on statistical significance.

Based on the scaling argument introduced in Section 2, we predicted that for a given structured surface: 1) $t_{ff} \propto \frac{\mu}{F_N}$, and 2) t_{ff} should be inversely proportional to h_o^2. The proportionality between t_{ff} and the ratio μ/F_N for the two structured surfaces is shown in Figure 7a by using the data for all the loading conditions investigated. For the second prediction we first observe that, as expected, the slope for the data of the W=10μm surface in Figure 7a is less than the one obtained for data coming from the W=3μm surface, consistent with the larger h_o of the W=10μm surface (see Table 1). Finally, we can take the ratio of slopes for the t_{ff} vs μ/F_N data for the two structured surfaces investigated. Based on Eqn 2, this ratio should be equal to the inverse ratio of h_o^2, which is close to what we observe (see Table 3). The range in the calculated values for h_o comes from the fact that it cannot readily be determined for the W=10μm surface because there is not a dominant length scale on the surface features that simplifies the analysis in Refs [35, 97], the same is true for the W=3 μm since the feature sizes are not firmly in the D>>W limit. The relatively good agreement between predictions from Eqn 2 and our measurements indicate that t_{ff} might be a signature for the onset of the drainage through the structures. Finally, based on Eqn 3 we predict that the time to reach boundary contact (t_{nf}) should be twice the time spent in the far-field regime, independent of the surface structure. This prediction is confirmed in Figure 7b where t_{nf} is plotted as a function of t_{ff} for the two surfaces investigated and for all the loading conditions. As seen in Figure 7b all the data collapse into a single line of a slope of 1.7. Note here that h_o is calculated based on normal loading (and unloading) and not peeling.

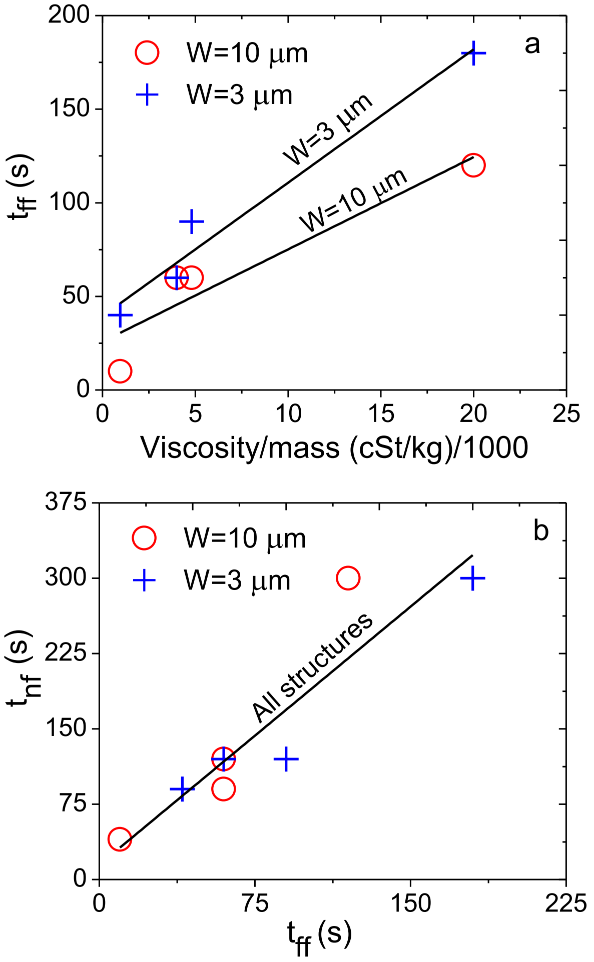

Figure 5.7. (a) Dependence of the far-field limit on the ratio of the ratio of ν/F_N, based on Eqn 1 we expect the slope to be linear and to be proportional to a length scale unique to each structure geometry. (b) Relationship between the far-field and near-field times, based on Eqn 3 we expect a linear relationship with a slope of 2. Linear least squares fits giving (a) W=3 µm: slope = 0.0071 and $r^2 = 0.97$ and, W=10 µm: slope=0.0049 and $r^2 = 0.87$, and for (b) slope = 1.7 and $r^2 = 0.85$.

Table 5.3. Values extracted from the slopes in Figure 7.

	Measured	**Predictions**
W=10 μm	h_o = 12.0 μm	h_o=7.9 μm
W=3μm	h_o = 8.1 μm	h_o= 2.8-6.1 μm
h_o(W=3μm)/h_o(W=10μm)	0.69	0.34-0.77
t_{nf} vs t_{ff} (Fig 7b)	1.7	2.0

We see that estimates for an effective h_o based on our experiments overestimates the predictions of Ref. [35] (see Table 3). The discrepancy could come from the fact that we are using an analysis based on normal motion to describe detachment via small angle peeling measurements. However, in our previous experiments we characterized the normal hydrodynamic forces during approach using the Surface Forces Apparatus and also observed that the effect of the surface structure in reducing the hydrodynamic force during approach was significant for separations larger than h_o.[97] Therefore it is more likely that the transition between the different regimes is gradual and would occur at separations larger than h_o (or could depend on separation), which could explain why we obtain effective values for h_o that are larger than predicted ones. Also that these predictions are based on scaling arguments in limiting geometries and as such inherently bring uncertainties.

5.4. Conclusions

Smooth and structured surfaces were loaded normally towards a flat substrate and peeled off in a viscous Newtonian fluid. The experiments were designed to highlight the interplay between the surface structure and the loading conditions. The effect of structures on the peeling forces was investigated and evidence for three regimes for the work of separation were observed. 1) The far-field regime corresponds to large fluid film thickness prior to pull-out and in this regime there is no effect of surface structure on the work of separation. 2) The drainage through structures regime is very short and corresponds to fluid film thickness that are sufficiently small such that the fluid flows through the structure and, as a result, a decrease in the work of separation compared to flat surfaces is observed. 3) The near-field regime corresponds to interactions between individual pillars and the surface where boundary contact is likely to occur, this regime was characterized by a plateau in the work of separation with loading time. Using simple scaling arguments we found that the boundaries for the different regimes could be related to the surface features via a parameter h_o. We also found that the relationship between the loading times for the near-field and far-field was near 2, independent of structure and in agreement with predictions.

Implication of our results for the role of viscous contribution on detachment via peeling are the following. 1) The presence of drainage channels reduces the drag upon approach and allows surfaces to make boundary contact faster. 2) The reduction in drag that facilitates approach also allows the surfaces to come apart more easily, as indicated by a decrease in the work of separation with structured surfaces when the loading conditions are kept constant. 3) If the fluid film thickness is too large prior to pull out the surface structures have no influence on the work of separation and behave the same way as smooth surfaces.

It is interesting to compare our results to those of Patil et al.[39] where the role of surface structure on the viscous forces measured during peeling was investigated. In their work they observed an increase in the work of separation with structured surfaces. We suspect that we reach different conclusions here because our surface structures are rigid (E=5.6 GPa) while they had a very compliant system therefore surface compliance appears to play a very significant role in modulating the peeling force in viscous environments. Recently Drotlef et al.[101] investigated the effect of surface structure on the adhesion force via normal retraction and on the friction force. In their experiments they did not observe that the fluid viscosity had an effect on the adhesion force (measured by peak force during retraction), and observed that the viscous contribution did not play an important role in their measurements. For the hydrodynamic component, in a system with a normal retraction with a compliant load cell, increasing the viscosity would not change the magnitude of the peak force in pull out measurements if the loading conditions are kept constant. While our experimental system is quite different from the toe pads of tree frogs, our results isolate the contribution of drainage channels to the adhesion force in flooded conditions in a loading scheme that mirrors the mode of tree frog attachment and detachment. In a more realistic system drainage channel could facilitate contact, while in contact conservative forces such as van der Waals interactions would become relevant and surface deformation would play an important role.

5.5. **Supplemental Information**

Peeling phase.

The rigid contactor pulling on the edge of the coverslip is mounted onto a bending beam load cell (Model LCL-454, Omega Engineering with a DP7600 strain meter, Omega Engineering, 0.4 mN resolution, ~20 readings per second). The bending beam load cell is attached to a vertically translating motorized stage (NSL4 Precision Linear Stage with custom 10:1 planetary gear, Newmark Systems, 0.13 μm resolution). During the peeling phase, a CCD camera (AVT Stingray F-125, binned to 644x300, 70 FPS) was used to take images of the sample as shown in Figure 2. The motor, camera, and data acquisition are all controlled through LabVIEW (National Instruments).

A representative force curve obtained during the peeling phase is shown in Figure S1 along with snapshots of the surfaces taken at different times during the peeling process. The force is plotted as a function of the motor displacement. Based on the pictures, we see that initially the separation between the surfaces appears constant, and the section of the coverslip in the bulk of the fluid up to the contactor begins to bend (Figure S1a) until the force reaches a peak (Figure S1b). Right after the peak, as the contactor continues to move upward, a crack becomes clearly visible and propagates laterally (Figure S1c) as the force decreases abruptly and the contactor tilts upward.

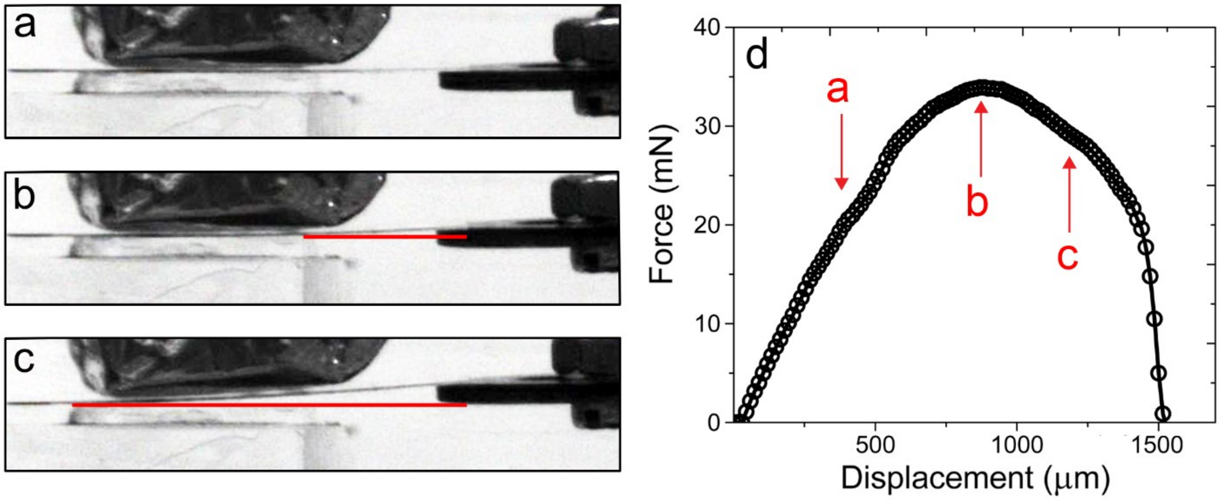

Figure 5.8. (a,b,c) Side view images taken during peeling. The sample is a smooth surface in 1000 cSt silicone oil brought near the lower surface with a 0.05 kg load during 180 seconds. The arrows on the force curve in (d) correspond to the images of (a-c). The red lines in (b,c) are a visual guide outlining the bottom substrate to show bending in the sample, which is slightly visible in (b) and more prominent in (c). The normal force applied by the aluminum foil is negligible during the peeling phase.

Calculation of the van der Waals interaction between two semi-infinite media

The non-retarded Hamaker constant[44] was calculated below, assuming a constant value for the dielectric constant.

$$A_{123} \approx \frac{3}{4}kT\left(\frac{\varepsilon_1-\varepsilon_3}{\varepsilon_1+\varepsilon_3}\right)\left(\frac{\varepsilon_2-\varepsilon_3}{\varepsilon_2+\varepsilon_3}\right) + \frac{3h\nu_e}{8\sqrt{2}}\frac{(n_1^2-n_3^2)(n_2^2-n_3^2)}{(n_1^2+n_3^2)^{\frac{1}{2}}(n_2^2+n_3^2)^{\frac{1}{2}}((n_1^2+n_3^2)^{\frac{1}{2}}+(n_2^2+n_3^2)^{\frac{1}{2}})}$$

Where 1 = CyTop, 2 = Silicone Oil (intervening medium) and 3 = SU-8, k is the Boltzmann constant, T is the temperature (298 K), h is the Planck constant and ν_e is the main electronic absorption frequency in the UV spectrum. This value, the dielectric constants and refractive indices can be found in table S1 below.

$$A_{CyTop-Silicone\ Oil-SU-8} = -8.0E - 23\ J$$

Table 5.4. Constants used for Hamaker constant calculations (all data from respective product data sheets)

Material	Dielectric Constant	Index of Refraction
CyTop	2[121]	1.34[121]
Silicone Oil	2.74[122]	1.4[123]
SU-8	3.2[124]	1.39[124]
ν_e=3E15 s^{-1}		

The van der Waal interaction energy (per unit area) of two flat surfaces[44] was calculated using the following formula:

$$W = -\frac{A_{CyTop-Silicone\ Oil-SU-8}}{12\pi D^2}$$

At a separation D=2 nm,

$$W = 5.31\ \mathrm{E} - 7\ \frac{J}{m^2}$$

Considering the interacting area between the surface and substrate is a square with a 12 mm length, the van der Waals interaction energy between the two substrates would be 1.04 E-10 J, far below the typical work of separation measured in our system.

Chapter 6

Coupling Deformable Surface Structures with Viscous and Adhesive Forces in Submerged Environments when Peeling

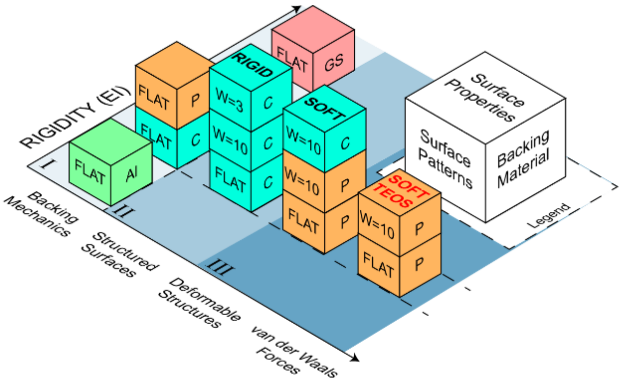

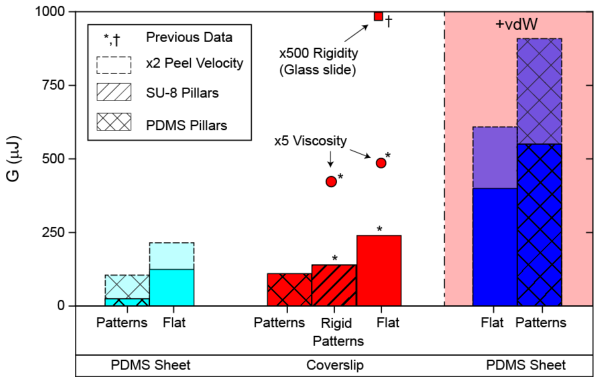

6.1. Introduction

Tree and torrent frogs are known to be able to adhere to completely flooded surfaces, without any interlocking supports[1], chemical based glues[1], nor capillary forces to aid them[125]. This ability has been attributed to the morphology of their toe pads, which contain a hexagonal array of hierarchical features[2,81]. These structured surfaces create drainage channels that aid in fluid removal so that their toe pads can make rapid contact to a surface, even under flooded conditions[126]. While many animals, especially geckos, have been shown to take advantage of patterns in their toe pads to enhance adhesion in dry[10] and wet conditions[127], less is understood about how these patterns might enable animals to adhere in completely flooded conditions. Understanding how these tree frogs take advantage of their patterned toe pads could open new avenues in understanding detachment in fluids, which is important in self-assembly[4], hydrofracture[6], micro-contact printing[3], the flow of red blood cells in capillaries[7], and medical robotics[5].

The role of structured surfaces and their drainage channels on tree frog adhesion is complicated by several factors: 1) the toe pad and the features on them are highly deformable (Outer layer, Young's modulus E= 5-15 MPa, effective E=4-25 KPa)[12], 2) the tree frogs are known to detach via a peeling type motion[1], and 3) the presence of both dissipative (viscous) and conservative (van der Waals) forces. In this study, 'dry' refers to situations where the adhesion derives from conservative forces such as van der Waals forces, without any contribution from viscous forces. These structured surfaces are a specialized type of surface roughness that permit drainage around structures. In the study here, we imitate this structure by creating a hexagonal array of pillars. In contrast, without the open spaces between the pillars, we would still have a surface that is described almost identically (in terms of area fraction), but the lack of drainage channels. (Appendix B is a related study that looks at this in depth in a different geometry)

Several of the previous phenomena have been discussed individually in the literature before. Tree frogs and many other animals detach using a peeling motion because it allows them to modulate the detachment force by simply changing the angle. [29] This important because strong attachment is important for keeping the animal in place, but a rapid detachment is also important to make locomotion efficient and quick. The role of structured surfaces on peeling has also been relatively well studied in dry environments.[25, 60, 92, 128-130] It has been shown that some of the key mechanisms responsible behind enhanced adhesion due to patterned substrates is that it impedes the progress of a crack by creating physical discontinuities.[26, 92] This requires that the crack be restarted at each discontinuity, which dramatically increases the adhesion. Furthermore, these patterns introduce additional compliance to the system which dissipations the peeling energy further and increases the adhesion forces.[128, 131]

There are considerably less studies on the effect of structured surfaces on adhesion in flooded environments, which specifically address the effect of drainage channels. In one study by Varenberg and Gorb.[110], the authors measured the friction of flat surfaces compared to patterned, hexagonal surfaces that contained drainage channels. In dry environments, they found that there was less friction on the micro-patterned surfaces. However, in wet environments, this trend reversed, and they observed increased friction on the patterned samples compared to flat. Furthermore, between the different types of patterns they tested, they found that the size of the drainage channels between the patterns had distinguishable effects on the friction, although the exact mechanisms are unclear. Studies by Drotlef and Iturri from the del Campo group have further demonstrated the importance of drainage channels. Drotlef et al.[101], focused on the chemical properties of the surfaces and fluids, and whether or not the wetting of structures was important. They found that, while viscous forces could be ignored in their system, the ability for the surface to drain away fluid had strong implications for making contact. Drainage determined whether the fluid wetted the structures and whether the structures would enhance or decrease friction. Iturri et al.[132] investigated the effect of anisotropic stretching of the hexagonal array, such that one axis is longer than the other is. This was inspired by recent studies on torrent frogs[2], which like tree frogs contain hexagonal patterned structures, but have been directionally elongated to adapt to higher fluid forces. They found significant changes in the friction force depending on the angle at which the force was applied over completely wetted surfaces for the elongated patterns. The effect of elongation was strongest for short patterns and disappeared at larger pillar heights.

In addition to the previous studies, within our group, we have studied the effect of drainage channels on hydrodynamic forces through two approaches. We have found that structured surfaces reduce the hydrodynamic repulsion when bringing two surfaces into contact, as verified by in a crossed-cylinder geometry in the Surfaces Forces Apparatus.[97] In another study examined structured surfaces by detaching patterned samples in a peeling apparatus, much like the one used in this paper.[73] During the approach phase, the structured surfaces were shown to be identical in detachment force from unpatterned features if the samples were not loaded sufficiently, but then would become lower than the flat counterparts would. Eventually the structured samples would not change in detachment force with increased loading due to boundary contact. The relevant results of that paper will be discussed more thoroughly throughout this text. In both cases, we found that the approach of the structured surfaces to a bottom surface differed than that from flat once the fluid film became sufficiently thin. First described by Persson[133], this deviation occurs on a length scale, h_o and accounts the spacing, diameter and height of the patterns into a single parameter. In both these papers, the structured were made from a rigid photo-patternable material (SU-8).

The interaction between viscous forces and deformable surfaces have been well studied, although usually for flat, unpatterned surfaces. There have been an increase in studies on the approach of soft materials to rigid substrates, or vice versa in viscous environments, which is an example of elastohydrodynamics.[18, 134-136].An earlier study in this group has considered the approach of a half-sphere to a soft substrate, but included the effect of a compliant load cell driving the sphere, instead directly by a motor, which complicates analysis and must be accounted for.[18] Furthermore, the geometry usually involves two surfaces approaching or retracting normal, or sliding across one another. There is relatively little literature that describe detaching a soft sample from a bottom surface via a peeling motion, but the general trend is that soft substrates cannot sustain the same fluid pressure as a rigid substrate, and thus elastohydrodynamics tends to reduce the viscous forces involved.

Even with those previous studies, there are still several unknown mechanisms. The first is an in-depth look at how viscous forces interact with peeling motions. The second is how drainage channels, alter viscous forces in a peeling motion. The third is how deformation affects peeling of both patterned and unpatterned surfaces. Finally, the coupling of van der Waals forces with viscous forces needs to be investigated, since it is unlikely that the effect of van der Waals can be accounted for by superposition of viscous and conservative forces. Our group has studied these systematically, leading up to this study. As seen in Figure 6.1, we have investigated how the changing the sample's mechanical properties alters the response to viscous forces in Chapter 5, in the first row, labeled 'backing mechanics'. Then (not chronologically), we take the samples with the same mechanical properties, but we have added rigid structures by fabricating a thin layer (20 μm total thickness) of 2 types different patterned surfaces.[73] Since those structured patterns were constructed from a rigid polymer and mounted on glass coverslips, we were able to exclude any effect of deformation and isolate how drainage channels affect the approach and detachment dynamics.

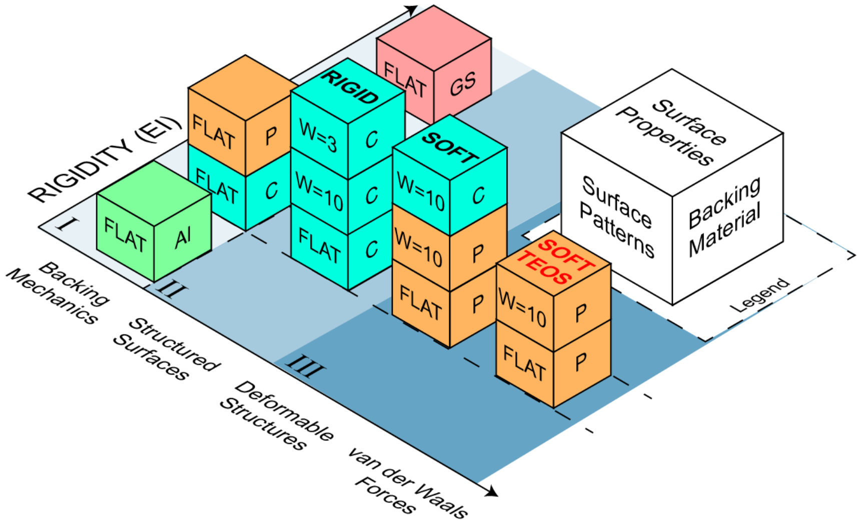

Figure 6.1. Overview of Sample Development. A summary of two previous related studies (I[Chapter 5], II[73]), as well as this one (III), denoted by roman numerals. The y-axis shows the rigidity, which is the same for nearly all samples, except for the first column. Stacked samples have the same rigidity but different Young's modulus (as in column I, for the stacked flat P and flat C), or some other different property. Each column (across the x-axis) represents the set of samples tested to isolate a single effect or mechanism. These effects

are from left to right: The effect of sample rigidity and Young's modulus (I), the effect of drainage channels in structured surfaces (II), the effect of deformable and patterned substrates (III) and finally, the competition between viscous and van der Waals interactions in submerged environments (III). The backing materials are Al – Aluminum Shim, GS – glass slide, P – PDMS sheet, and C – coverslip. All samples have been tested (but not limited to) at 300 µm/s drive velocity and 200 cSt for direct comparison.

In this paper, we investigate the remainder of unstudied mechanisms that we have identified – the effect of deformable structured surfaces on viscous forces. We then introduce the effect of van der Waals interactions by changing the chemistry of the system, but not changing any of the geometry or mechanical properties. We show how the deformation can introduce dramatic changes in the viscous forces, and we relate the results from our addition of van der Waals forces to results in the literature.

Peeling Apparatus

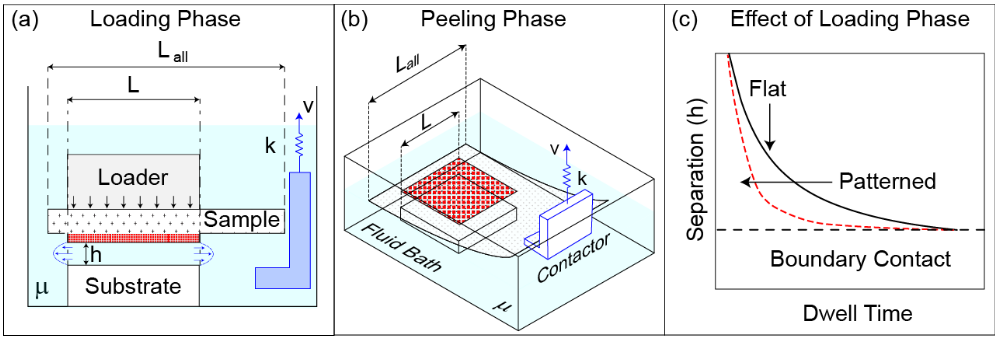

Figure 6.2. Schematic of peeling apparatus. The loading (panel a) and unloading (panel b) are shown schematically. In panel c, a schematic shows the change in fluid film thickness with increasing dwell times, and the effect that patterned samples can have on this.

Loading Phase. As schematically shown in panel a of Figure 6.2, the sample is gently placed into the fluid bath and aligned to the bottom substrate. At this point, the surfaces are far apart and the sample does not adhere to the substrate. Then a loader is brought downward onto the sample until a force sensor, attached to the tip of the loader, reads the desired load (2 N in most cases). The sample is square of side length L_{all} (22 mm) but interacts over an area of LxL (12 x 12 mm) to match the substrate. The loader is also 12 x 12 mm. The load remains constant and allows control over the film thickness between the sample and substrate by varying the duration the load is applied, known as the dwell time. The separation is a function of the load, dwell time, viscosity and sample area and is given by the Stefan equation for parallel plates.[79] Assuming the plates are far apart, it is determined by:

$$h = \sqrt{\frac{\mu L^4}{2Ft}} \tag{6.1}$$

Where h is the separation between the sample and substrate, μ is the viscosity, L is the area over which the two surfaces interact, F is the applied load and t is the duration of loading (dwell time).

We do not measure the separation between the sample and substrate, and factors such as tilt, roughness, or attractive interactions (such as van der Waals forces) can accelerate drainage[37]. It has been shown that when a structured sample is loaded for sufficient time, such that $h \sim h_o$, the fluid will drain around the structures and accelerate contact.[97] In this case, the structured sample investigated here deviates on a length scale of 8.0 μm.[73]

Unloading Phase. During the unloading phase, the weight is removed and shortly after (<2 seconds), the contactor begins peeling off a sample. The contactor is attached to a compliant load cell ($k = 6.3 \times 10^3$ N/m) and the load cell attached to a motor. This motor is driven at constant speed (*v*) ranging from 200 to 600 μm/s in a 200 cSt silicone oil bath. As seen in our earlier work, this combination keeps the Reynolds number <1 even at the 600 μm/s peel speed. During the peeling process, the angle varies but is within the small angle limit, below 5°. As further discussed throughout the paper, in the samples without the TEOS coating, the primary source of adhesion between the sample and substrate is from the viscous fluid. Additional sources include the flexure of the coverslip and the extensional compliance of the PDMS sheet samples. In the TEOS coated samples, the previous mentioned phenomena are still present, with the addition of van der Waals forces.

6.2. **Experimental Details**

Sample Geometry. Most the samples in this study consist of a 3.8 mm thick PDMS sheet that is a 22 x 22 mm sheet. This sample has been chosen to match the rigidity of a glass coverslip used in the previous studies (0.012 Nm^2). There are two different topographies, a flat surface and a hexagonal array of pillars (shown in Figure 6.3). The hexagonal array of pillars cover a 12x12 mm square area, mirror the dimensions of our earlier work[17] and are referred by the same notation as W=10. The pillars are 10 μm high, have a spacing of 10 μm, and a diameter of 10 μm. These patterns are located on the sheet, offset on one axis from the center so that the square array of patterns is 2 mm from one edge. For the coverslip samples, there is a base layer for uniformity (δ = 10 μm), and thus the PDMS on coverslip consists of a 20 μm high PDMS sample. We have demonstrated in an earlier paper that flat PDMS coatings on coverslips are indistinguishable in these experiments from SU-8 coated coverslips (Chapter 5), because the layer is so thin that it is essentially rigid[65].

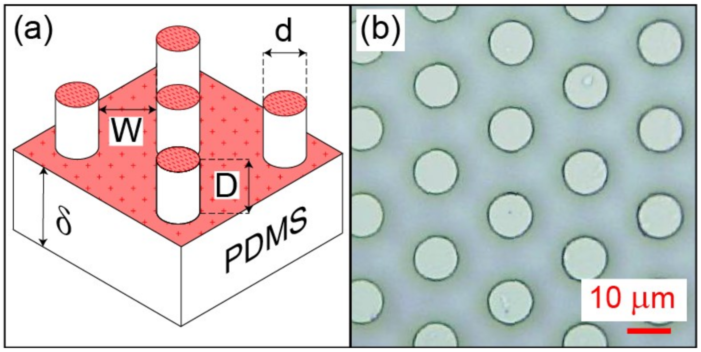

Figure 6.3. Sample Geometry. In panel a, a schematic of the sample is shown. Pillars are spaced a distance W, are D high and have a diameter of d. Patterned samples have

parameters W=D=d=10 μm. The PDMS has a base layer δ thick. In panel b, a picture of the PDMS pillars are shown. Red bar is 10 μm.

Contact Angle Hysteresis Results. The TEOS coating was tested using Millipore water for the advancing and receding contact angle to determine if the interfacial energy of the surface was appropriately altered. The results are tabulated in Table 6.1. Native PDMS is considered hydrophobic and has advancing and receding angles of ~115° and ~97° respectively[137] and the TEOS coating was tested to ensure the surface remained hydrophilic and did not recover its native hydrophobicity.

Table 6.1. Contact angle hysteresis of TEOS treated PDMS samples using water. N/A refers to very low (completely wetted) contact angles.

Time (hrs.)	Hysteresis (°)	Advancing (°)	Receding (°)
1	N/A	16-23	N/A
3	8-11	28-64	20-53
20	7-18	38-49	30-35
48	7-17	56-73	27-65
120	18-20	77-81	59-61

Sample Fabrication of PDMS Sheets. PDMS sheets (22 x 22 x 3.8 mm) are fabricated by using a two stage of molds. The strategy is to create a template of SU-8 pillars on a silicon wafer is molded by PDMS, and then that PDMS mold is treated with a trichloro(1,H,1H,2H,2H-perfluorooctyl) silane to make a mold for the final sample.

The template was created in a two-layer photolithography. A silicon wafer was cleaned with isopropyl alcohol/ethanol and then hard baked at 200° C for 10 minutes. Then, for the first layer, a 10 μm thick layer of SU-8 was created by spin coating SU-8 2007 (MicroChem) at 1700 r.p.m. for one minute. This was pre-exposure baked on a hot plate at 95° C for 3 minutes and then exposed to a UV source (i-line) at 140 mJ/cm^2. This layer required no mask. After UV exposure, the samples were baked again in a post-exposure bake for 3 minutes at 95° C. After the sample cooled, the same procedure as before was done again, but during UV exposure; a chrome mask was used to develop the hexagonal array of 10-μm diameter, 10 μm channel width (20-μm center-to-center distance) pillars. Then after the post-exposure bake, samples were developed in SU-8 developer (MicroChem).

With the SU-8 template ready, we created a PDMS mold from this by casting a 10:1 PDMS elastomer mix (Sylgard 184, Dow Corning) onto the wafer. The 10:1 PDMS mixture has been degassed before use. We use a large weigh boat to enclose the wafer and tape it to the bottom to ensure that the wafer remains stationary. We pour a 1 mm thick layer and then degas again to ensure the PDMS infiltrates into the pillars. This is then cured at 100° C for 5 hrs. Once cured, the PDMS is gently peeled away from the wafer. Finally, to prepare a mold made from PDMS for use in casting the same material, it is necessary to silanize the mold thoroughly[42]. The PDMS mold was placed inside a desiccator with 20 µL of trichloro(1,H,1H,2H,2H-perfluorooctyl) silane (97%, Sigma Aldrich) placed on a glass dish. The desiccator was then evacuated under coarse vacuum and incubated for 12 hrs. Then the sample was placed in an oven at 100° C for one hour to anneal the silane.

With the mold ready, samples were made by pouring uncured PDMS (10:1 ratio) to a 3.8 mm thickness, degassing to ensure infiltration into the patterns, and then baking at 100° C for 5 hrs. and removing the samples carefully after curing. Flat samples are made by casting PDMS onto a silicon wafer for flatness. The roughness of the flat samples have been tabulated in an earlier study by profilometry. (Chapter 5)

Sample Fabrication of PDMS Pillars on Glass Coverslips

PDMS pillars on glass coverslips were created by casting PDMS into an SU-8 mold on silicon and then carefully removing the PDMS layer and bonding it to a glass coverslip via oxygen plasma. The SU-8 mold is fabricated exactly as described before, but instead of pillars, the opposite – wells, were fabricated. Then a 20 µm thick layer of PDMS was cast into the SU-8 wells by spin coating at 1150 p.m. for 1 minute. Due to the difficulty in peeling 20 µm thin PDMS layers from a mold, thicker portions of PDMS elastomer were painted outside the desired feature to aid in handling. The 20 µm thick PDMS layer was then treated on the unpatterned side with a handheld tesla coil for 40 seconds and then pressed firmly onto a clean glass coverslip. This was then heated on a hot plate for 2 hrs at 100° C.

TEOS Coating Procedure

The TEOS coating procedure was taken from the method described by Abate et al.[43] but adapted to coat planar substrate, instead of the inside of a microfluidic channel. It was also adapted to ensure the coating is thin enough to preserve the patterns. As described by Abate et al., we prepared a 1:1:1:1 solution of TEOS (tetraethyl orthosilicate, reagent grade 98% Sigma Aldrich), MTES (Triethoxymethylsilane 99%,Sigma Aldrich), HCl adjusted to pH 4.5 with D.I. water, and ethanol. This solution was gently stirred on a hot plate at 65^o C for 12 hrs. After a brief nitrogen air clean on the PDMS sample, it was exposed to oxygen plasma for 30 seconds at 50W and the TEOS solution was spin coated onto the PDMS surface by spinning on a spin coater at 1000 r.p.m for 30 seconds. This was then cured on a hot plate at 100^o C for 2 minutes. This resulted in a layer approximately 500 nm verified by profilometry. We estimate the Hamaker constant for this system to be that of SiO_2-Water-SiO_2 and equal to 0.63×10^{-20} J[44].

6.3. Results and Discussion

Effect of Elasticity on Flat and Patterned Samples. In this study, a flat and a patterned PDMS sheets were tested in 200 cSt silicone oil across three different peel velocities (200, 300 and 600 μm/s). We also tested a thin layer of PDMS patterns mounted on a coverslip backing at 300 μm/s to draw direct comparisons to a previous study where the patterns were made of a rigid photopolymer, SU-8. As mentioned earlier, the sheet and coverslip are comparable because they have the same rigidity. Due to the materials used to fabricate the sample, the coating of the bottom surface, and the silicone oil bath, there are minimal van der Waals forces present which allows us to isolate how viscous forces interact with deformable structures.

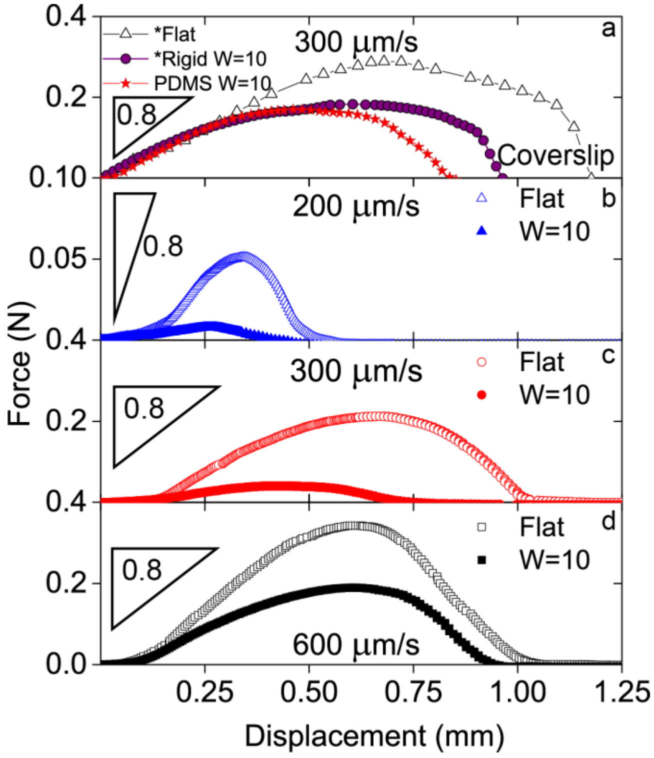

Figure 6.4. Representative Force Curves of Samples without TEOS coating. Panels a-d show representative force versus displacement curves of patterned (W=10 see text for dimensions) and flat samples on two different backings. In a), W=10 µm PDMS pillars (red stars) on a coverslip backing are compared to a previous study[17] (reprinted with permission) in the limit of long loading times with the same geometry as well as a flat sample. Rigid samples are made of SU-8 and the flat sample contained a 20 µm SU-8 layer. Panels b-d compare PDMS pillar samples to flat, featureless samples on a PDMS sheet (3.8 mm thick) at increasing peel velocities. Note the x-axis is the same on all panels, and the y-axis is

only different in panel b. All samples peeled in 200 cSt silicone oil. Slope of 0.8 is shown in each panel to visually compare the initial slope of each force curve.

Typical force curves from loading in the long time limit and peeling these samples are shown in Figure 6.4. Results from the PDMS patterns on coverslip are shown in panel a, as well as results from a previous study[17]. The force curves from the previous study have also been loaded in the long loading time limit. Immediately, we see that the force curves from the PDMS patterns are smaller than their SU-8 counterparts and detach at a smaller motor displacement (~ 0.8 mm versus ~0.95 mm). The initial slope on the force-displacement curves of the PDMS pillar and SU-8 pillar overlap, as well as the flat sample. Panels b-d shown the difference between flat PDMS sheets and patterned PDMS sheets. As the velocity increases, the forces increase for both the flat and the patterned sample. However the patterned sample appears to be increasing more, relative to the velocity at 200 μm/s, than the flat does with velocity. The initial slope on the force-displacement curve of the patterned samples is far less than the flat at 200 μm/s and at 300 μm/s, and somewhat lower in the 600 μm/s case. Furthermore, this slope seems to increase for the flat sample from 200 μm/s to 300 μm/s, but ceases to increase from 300 μm/s to 600 μm/s.

While soft, deformable patterns are typically known to increase adhesion[26, 128], we do not expect or observe enhancement of peel forces in any of these samples. Whether we compare the PDMS pillars to rigid pillars in panel a, or even compare the flat coverslip to the PDMS sheets at 300 μm/s (panels a and c), in a purely viscous system we do not see that deformation contributes to an increased peel adhesion. This is because there are no conservative forces, such as van der Waals interactions, and the patterns do not enhance the adhesion by creating physical discontinuities that halt the peeling front. Likewise, the flat samples do not benefit from additional conformal contact with the bottom surface (reported first by Dahlquist, recorded in Ref. [138]) because this enhanced contact would not lead to enhanced adhesion.

Instead of increasing the peel forces, the ability for patterns to deforms appears to lower forces in comparison to rigid patterns, as shown in panel a. When pillars are soft enough to deform, it introduces several factors which could decrease the forces. [128] First, the substrate could deform underneath the pillars, which is possible because a base layer of 10 μm of PDMS supports the PDMS pillars (10 μm high). Second, the pillars themselves could bend or stretch. Finally, the fluid forces could be altered due to the flow around the deformable surfaces. In the case of the flat samples, even with the same rigidity, we have shown that extensional compliance (Chapter 5), or the ability for the substrate to deform normal to the surface, can account for the lower forces when comparing coverslips to PDMS sheets. This role of compliance on adhesion has been explored in depth in dry adhesion.[61] It would seem unlikely that the pillars deform the substrate in addition to this effect and this substrate compliance has been accounted for in the flat PDMS sheets. In regards to the pillars deforming by bending or stretching, the compliance (0.05 m/N), has been measured by Crosby et al.[139] for PDMS pillars with an aspect ratio of 1 and a diameter of 20 μm. If the pillars were deforming or bending significantly, it would lower the forces far more than what we see since the compliance of a single pillar loaded on its circular plane surface would be relatively high. In fact, the compliance of the pillars is higher than the compliance of a flat sheet[131], but the reduction in forces between the pillars and sheet is not consistent with the difference in compliance between pillars and flat samples. This is confirmed if we consider the large difference in sample compliance between the coverslip-backed data, which would estimate around a 100-fold decrease between the flat SU-8 and patterned PDMS. This all suggests that the viscous force on the pillar is not applied in the same mode as many dry systems and instead the fluid applies a force on the pillars by flowing around it.[140] Finally, the difference between patterned and flat PDMS sheets appears to decrease with increasing velocity, instead of staying at a constant factor.

This leaves us with the effect of hydrodynamic flow around soft surfaces. When comparing the SU-8 and patterned PDMS on coverslips, we see a noticeable but modest reduction, which is in line with the magnitude of many elastohydrodynamic systems using PDMS.[18, 141] For the PDMS sheets, the force curves show that the patterned samples increase relative to the flat samples at higher velocities. This velocity dependence gives additional support that the reduction in force between a rigid and deformable patterned sample is related to the reduced drag around a soft, deformable pillar.

Finally, if the adhesion between the sample and bottom surface is not sufficient to bend the sample, such as the case at 200 μm/s peel velocity, the forces will be very low since the sample is being lifted off instead of peeled. This can be seen by the difference in initial slope, which is a function of the system compliance, which has been demonstrated in other adhesion tests in dry environments mentioned earlier.

For further comparisons, it is helpful to integrate the force-displacement curves to obtain a total energy required to separate the samples, referred to as “G”. In the absence of any conservative forces, this means that G will represent purely dissipative processes only, such as the hydrodynamic force and elastic dissipation.

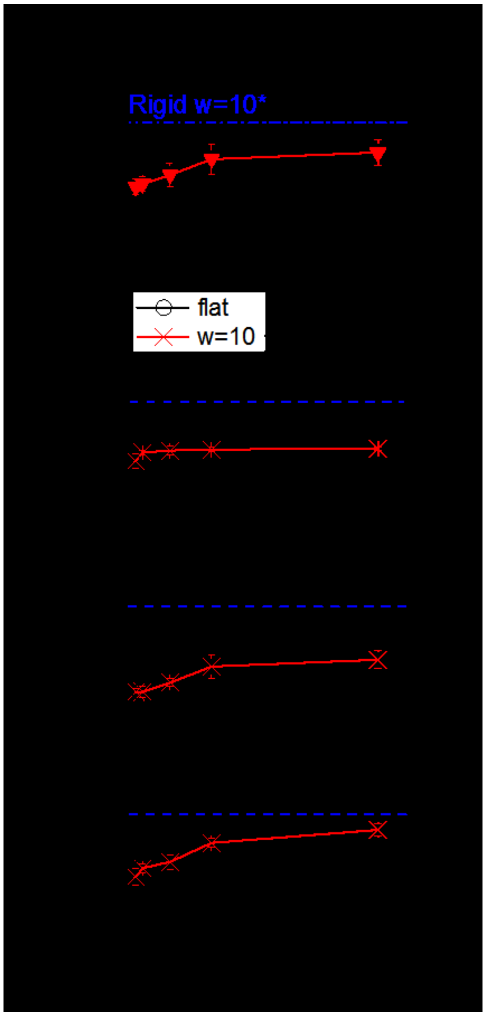

Figure 6.5. Comparison of Work (G) to Separate Samples (without TEOS) versus loading time. Samples mirror the conditions in the previous force-displacement figure: Panel a shows the integrated force-displacement curve of patterned PDMS on coverslips and is compared to previous data in the long-loading time limit (the rigid SU-8 samples are noted as black – flat sample, blue – rigid patterns, reprinted with permission). Panels b-d show 3 different peel velocities of patterned and smooth PDMS sheets. Black lines in b-d show the long time limit at 180 seconds of loading. Unlike in panel a, the blue dashed lines in panel b-d are at 61% of the black dashed lines at each velocity. Samples in 200 cSt silicone oil.

These results are plotted in Figure 6.5 and mirrored the conditions of the force curves in Figure 6.4. Different loading times have also been tested and the integrated force-displacement curves. Panels a show the data from PDMS patterns on coverslips from this paper for different loading times, with the long loading times of flat samples (black lines) and SU-8 patterns (blue lines) from a previous study[17]. Panels b-d show G from different loading times of the patterned and flat PDMS sheets at different peel velocities. In these panels, the black dashed line represents the long loading limit of the flat sample. The blue dashed lines are 61% of this long loading limit. This 61% represents the same ratio of the SU-8 patterns on coverslip to the flat coverslip and serves as a reference line.

For the PDMS sheets in panel b-d, we see several trends between the flat and patterned samples. As seen in a previous study, at low loading times the patterned and flat samples have similar values. We also see that the PDMS patterns reach a plateau value, where it no longer increases with increasing dwell time. However, the flat samples still increase with increasing dwell time, in the dwell times tested. In a previous paper, we determined that flat samples no longer increased after 180 seconds.

As the peel velocity increases, we also see that the PDMS patterns reach closer to the blue line. Since the blue line is a proportion of the flat sample at each velocity, the PDMS patterns are a larger proportion of the flat sample at increasing velocity, instead of a constant percentage.

In panel a, the PDMS pillars on coverslip are lower than their SU-8 counterparts. They also show many similarities however. They plateau at long dwell loading times.

It appears that the ratio of patterned PDMS to flat PDMS increases with velocity for both the forces and the integrated force-displacement curves (G), as highlighted in Figure 6.5 (b-d). The blue dashed line in each panel represents the ratio of the rigid patterns to the flat coverslip, could be thought of an upper limit on the G in the limit of a rigid material with no deformation. We see that the patterned samples approach this line at higher velocities, and the ratio of the PDMS pillars on coverslip at 300 μm/s is very similar to the PDMS pillars on a sheet at 600 μm/s. This velocity dependent contribution suggests viscous interactions. The data does not seem to support that the reduction in forces in viscous environments are from the dissipation in the deformation of the pillars. This effect, which can be accounted for as an additional source of compliance, and thus energy dissipation, would be a correction factor, independent of the applied force and would be constant across all velocities. Especially the difference between patterned PDMS and SU-8 pillars on coverslips is relatively small (Panel a in both Figure 6.4 and Figure 6.5). Again, we do not observe radical departures in force at all velocities between flat and PDMS pillars, whether on a coverslip or PDMS sheet backing and confirm our findings based on the force curves with G.

Effect of van der Waals Interactions. The same experiments were conducted on patterned and flat PDMS sheets, but with amplified van der Waals interactions, such that they are no longer negligible compared to the viscous forces. This was done by coating the PDMS in a thin (<500 nm) TEOS coating and replacing the silicone oil with 200 cSt glycerol-water mixture (~95/5 glycerol-water mixture, determined by rheometer).

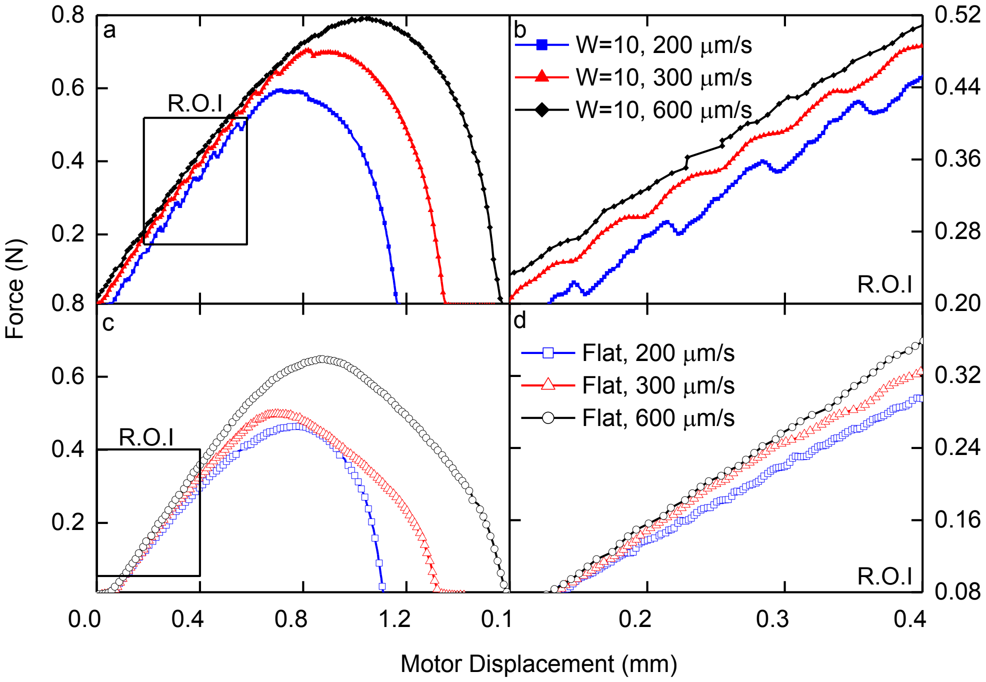

Figure 6.6. Representative force curves of TEOS treated PDMS samples. Unlike the previous force displacement figure, panels either contain patterned or flat samples at all

three tested velocities. Panels a-b are the patterned samples, and b is the enlarged region of interested (R.O.I) of the force-displacement curve in panel a. Likewise panel c-d are representative force-displacement curves of flat samples, and d is the enlarged ROI section in panel c. Samples loaded in 200 cSt glycerol-water mixture.

In these force-displacement curves, we see several differences that occur from adding a TEOS coating on the samples and replacing the silicone oil bath with a glycerol-water mixture of the same viscosity. In Figure 6.6, both the patterned (panel a) and flat samples (panel c) show much higher forces than without the TEOS coating at all velocities. Unlike the previous, purely viscous case, the initial slope of the force-displacement curve is consistent across all velocities, suggesting there is enough adhesive (both viscous and conservative in origin) to cause the sample to bend.

Notably, the initial portion of the patterned samples (zoom in on R.O.I in panel b) show a saw-toothed as the force reaches a local peak, drops, and then rises again. This is most prominent in the 200 μm/s samples. The periodicity increases, while the amplitude decreases when peeled at 300 μm/s and the saw-tooth pattern is not readily visible at 600 μm/s. This can be compared to the flat force curves in panel d that seem to show much smaller, random variations in the forces. Overall, even the flat force curves of TEOS samples seem to show more noise than any of the previous samples, in this study or previous studies. This increased noise is not present in systems with only hydrodynamic drag, and the noise could be a result of friction or some intermittent stick-slip behavior.

There has extensive literature exploring the mechanics how patterns in systems with conservative forces enhancing forces while peeling. Saw-tooth patterns are commonly seen in the force-displacement plots when peeling patterned surfaces. This occurs because patterns serve as physical barriers to crack propagation and when a peeling front encounters a gap, the crack stops propagating and must be reinitiated. When this occurs, the peeling front must reinitiate a crack to continue peeling apart the surfaces. Reinitiating a crack requires an increased application of force, but once the new threshold in force is met, it rapidly propagates until the next discontinuity. In a completely dry system, the periodicity of these cracks has been straightforwardly related to the geometry of the sample by correlating the spacing of patterns to the saw-tooth patterning in the force-displacement curves.[25, 26, 111] However this is difficult to correlate in this case because the peeler is connected by a compliant load cell to the sample, so the actual velocity that the peel front propagates is not straightforward to calculate, since it does not necessarily match the motor velocity. (See Chapter 5) Secondly, the peel front in this viscous system is unlikely to be a sharply defined interface that peels a perfect row of patterns at a given moment**.** With these caveats aside, the patterned surfaces show a periodic undulation in forces, most pronounced at 200 μm/s and less so at 300 μm/s, which we do not observe without the TEOS coating, nor in the flat surfaces with a TEOS coating. Furthermore, the 200 μm/s has a larger periodicity than the 300 μm/s samples, which is consistent with how often a peeling front would encounter a patterned feature for identical samples. To see if the patterns are the appropriate dimensions to have an enhancement effect, the patterns must be smaller than the length across which a peeling front applies a force.[71] This length is called the stress decay length and for our samples, the stress decay length is 0.53 mm, which is larger than the lateral spacing of the patterns at 10 μm.

When looking at the flat samples, we can compare to studies done on the adhesion between a flexible plate and elastic films through a similar device.[25] We can compare the change in peak force between the TEOS and non-TEOS coated samples to estimate the effect of changing the Hamaker constant of the samples. Based on the work by Ghatak et al.[25], we can relate the change in max force to the Hamaker constant by:

$$F_{peak} = \frac{A_{Hamaker}}{6\pi d_o^3}\frac{3h * Area}{a}\left(\frac{D}{12S}\right)^{\frac{1}{3}} \qquad (6.2)$$

Where a is the lever arm – the distance from the contactor to the portion of the sample adhered, d_o is the initial separation, h is the sample thickness, D is the sample rigidity, S is the shear modulus and $A_{Hamaker}$ is the Hamaker constant. For the area, we estimate as the stress decay length times the width of the contacting area (L). To a first approximation, we consider the increase of peak forces between the TEOS and non-TEOS coated samples using Equation (6.2). Using relevant experimental values (h = 3.8 mm, Area = 12 mm * 0.53 mm, D = 0.0012 Nm^2, S = 2.5E5 MPa, $A_{Hamaker} = 0.63 \times 10^{-20}$), we can calculate the initial separation between the TEOS surfaces. For comparison, we take the values at the long dwell time limit (180 seconds) of the flat non-TEOS and TEOS samples. The results are tabulated in Table 6.2.

Table 6.2. Calculated initial separation from differences in peak forces of TEOS and non-TEOS flat samples in the long dwell time limit.

Peel Velocity v (μm/s)	Difference in Peak Force ΔF (N)	Initial Separation d_o (nm)
200	0.53	0.20
300	0.14	0.32
600	0.35	0.24

As we see from Table 6.2, we arrive at values of the initial separation comparable with the roughness of the samples. However, it is difficult to draw concrete conclusions from these calculations. These could compare favorably with the roughness due to canceling errors, or it could be that making contact in a submerged environment can smooth out roughness.[46] In the previous study by Ghatak et al. [25], they found about a 10x difference in their calculations for surface separations compared to their surface roughness. Ultimately, we find that the TEOS coating has enhanced the peel forces from an effect consistent with van der Waals interactions. We also do not see a dependence on the difference in peak force with velocity. While at first glance, it would appear intuitive that these van der Waals forces, which are a path-independent conservative force, should not depend on the peel velocity, it is well established in the literature that peeling samples will exhibit velocity dependence, even with purely conservative forces. [49, 142]

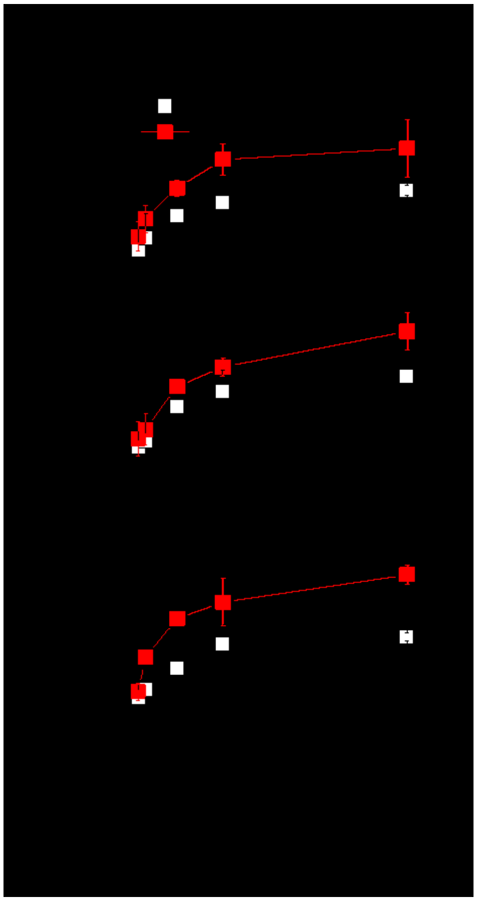

Figure 6.7. Comparison of Work (G) to Separate Surfaces with TEOS coatings versus loading time. Panels a-c compare patterned samples to flat samples at three different velocities. The black dashed lines are the same dashed lines in Figure 6.5 that represent the work in the long-term loading time without the TEOS coatings. Samples are peeled in 200 cSt glycerol-water mixture.

At lower dwell times, where the separation between the sample and bottom surface should be large, we still see enhancement from the TEOS coating. This is somewhat surprising because the previous studies have established that the surface and bottom surface separation are further than the critical separation[17, 35, 97] required for fluid to drain into the structures, which is of order microns. It is unlikely that van der Waals interactions act across such a large distance. To reconcile this, portions of the sample during the loading phase must reach the bottom surface sooner than other portions of the sample. In other words, the approach is not perfectly parallel. In this case, the portions of the sample in contact would aid in accelerating drainage between the sample and the bottom surface, which could account for the enhancement at even low dwell times. If drainage through the structures is occurring, it might not be a strong enough to be different from flat samples in the peel test until enough drainage occurs.

It appears even in the TEOS system, we still see a regime where the patterned surface and flat surfaces overlap in G. As mentioned in the introduction, we identified this region as the near field time in a previous paper. For loading times under the near field time, the fluid has not entered the patterns of the sample enough to cause a discrepancy in the G between the flat and patterned samples. However, if we compare the samples at peel velocities of 600 μm/s, at dwell times of 10 seconds in panel c of Figure 6.7, the patterned sample is higher than the flat sample. If we compare this to the same dwell conditions in panel d of Figure 6.5 (without TEOS), the flat sample and patterned sample are statistically similar and thus the near field time has been affected by the TEOS coating in this case. However, this could also be attributed to the instruments capabilities, since the non-TEOS coating shows some range in the near field time: at 200 and 600 μm/s, the near field time is after 10 seconds, but at 300 μm/s it appears to be somewhat before. Ultimately, we see an enhancement from van der Waals at even relatively large separation, which is contradictory. This occurs because the drainage dynamics is probably aided by van der Waals forces. However, we surmise that portions of the TEOS coated samples are in contact, but the not the entire sample. We postulate that the average separation between the sample and bottom surface still gives rise to a regime where the patterned and flat samples are the same and another regime where the patterned and flat samples diverge in G.

Velocity Dependence of Viscous and van der Waals Interactions. We explore the velocity dependence of viscous and van der Waals interactions together. In Figure 6.7, we see the G for the TEOS coated samples, with the long loading limit of the flat samples in the non-TEOS system in the black dashed lines. When comparing across velocities, the flat TEOS coated samples do not seem to be a constant distance from the black lines. This suggests that the TEOS coating cannot be accounted for by a constant term at all velocities. As reflected by the force displacement curves, the G for TEOS coated patterned samples exceeds that of their flat counterparts. This is a reversal of the previous trends, in the samples without TEOS and our earlier work[17], where patterns have always shown reduced forces compared to flat samples when considering viscous interactions alone.

We can consider the change in G with velocity for both van der Waals forces and for a purely hydrodynamic system by plotting the G versus velocity on a log scale, as seen in Figure 6.8. In panel a, for the flat samples without TEOS, we note that at low velocities (200 μm/s), the hydrodynamic drag is too low to bend the samples significantly. This makes the increase to 300 μm/s more dramatic. Except for the 5-second dwell time, the 300 μm/s to 600 μm/s of the non-TEOS coated samples show a similar trend in increase. We note the slope of the 300 μm/s to 600 μm/s 180-second dwell time sample is 0.8, which means that G is proportional to $v^{0.8}$ under those conditions.

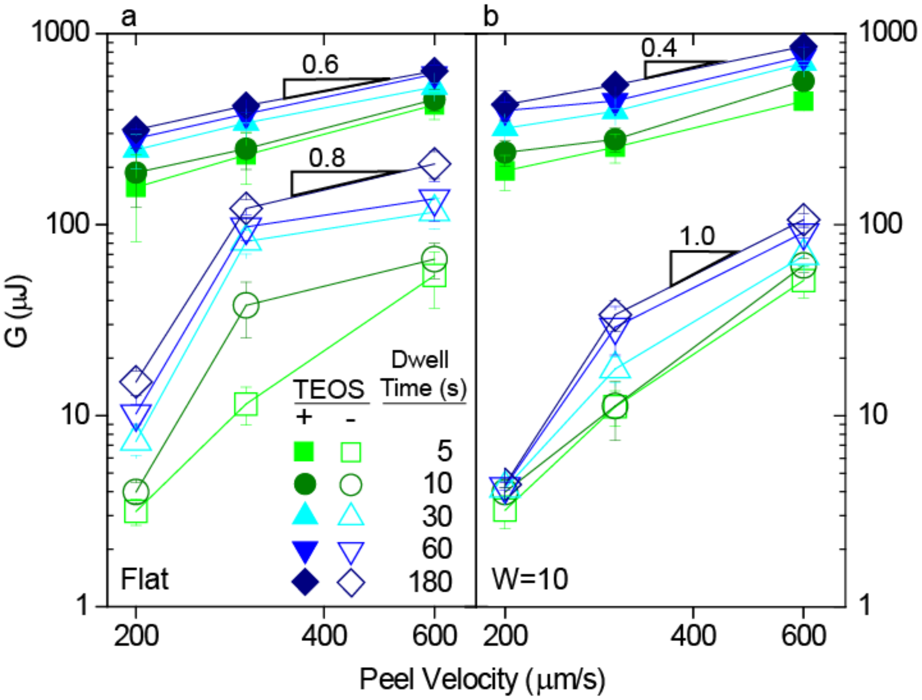

Figure 6.8. Change in G with peel velocity for different dwell times. In panel a, values of work flat samples including with and without TEOS are plotted against peel velocities. In panel b, the patterned samples are shown. Slope of one condition (180 second dwell time from 300 μm/s to 600 μm/s) shown for comparison. Legend refers to different dwell times (in seconds) and open symbols represents sample treated with TEOS coating and peeled in 200 cSt glyercol-water mixture. Closed symbols are peeled in 200 cSt silicone oil, without TEOS treatment (purely viscous system).

In the flat samples with a TEOS coating, there is consistency between the slope from 200 µm/s to 300 µm/s to the slope from 300 µm/s to 600 µm/s. The additional van der Waals contribution sufficiently bends the sample, even at 200 µm/s, which is not the case in the non-TEOS samples. For flat samples under the same conditions, the slope between 300 µm/s to 600 µm/s at 180 seconds is 0.6. This suggests that for flat samples, the addition of a TEOS coating has lowered the power at which G depends on the velocity. These trends are upheld for the other dwell times as well, but with differing values.

Overall, the slope with TEOS seems to decrease for flat samples compared to the non-TEOS samples. Although there is relatively few velocity studies available for similar apparatuses at low peel angles like this, we can compare to several constant angle peel tests. Work by Creton et al.[49] and Leger et al.[143] have demonstrated that G scales with velocity as 0.23 and 0.25 respectively, which would be consistent with the downward shift in velocity dependence from the non-TEOS to TEOS coated samples.

The patterned samples also show a similar downward dependence on velocity with introduction of the TEOS coating. As discussed in the force curves without TEOS coatings the 200 µm/s and 300 µm/s peel velocities both do not induce enough hydrodynamic drag to bend the sample. At 600 µm/s, there is enough hydrodynamic drag to bend the sample and since this did not occur until 600 µm/s, instead of 300 µm/s the slope is larger than the flat case. There are several studies that examine the effect of pattern sizing and optimal dimensions for enhancing adhesion or reversibility[60,131,144] and future designs could optimize this combination of viscous and van der Waals forces, depending on the application.

6.4. **Conclusions**

Within this paper, we have investigated how the detachment forces and G changes for samples peeled in viscous fluids. We have shown how deformable surfaces and deformable structured surfaces can lower these forces when considering purely viscous interactions, even more than rigid structures. The mechanism behind this reduction has been attributed to the fluid deforming the structures, which has been narrowed down from several other possible contributions due to the increased compliance of deformable structures.

We have shown that these deformable structured surfaces can increase the forces and G if van der Waals forces are introduced, and these increases can overcome the reduction from viscous forces. We were able to identify characteristic saw-tooth patterned in the force curves, which are indicative of crack arrest on structured surfaces. We also saw that the enhancement from van der Waals was significant enough to overcome the reduction in detachment force from the viscous contributions. Yet while we have shown evidence for van der Waals interactions, they cannot be considered as a superposition with the viscous forces.

While we have probed a narrow space of sample dimensions, we have chosen to explore the effect of patterned samples under different phenomena to isolate their coupling. These phenomena are the role of viscosity and rigidity, the effect of structured surfaces, the role of deformable flat and structured surfaces, and the coupling of van der Waals forces with hydrodynamic forces. We summarize the relative importance of these phenomena on G by plotting our results from this study and a previous study in Figure 6.9.

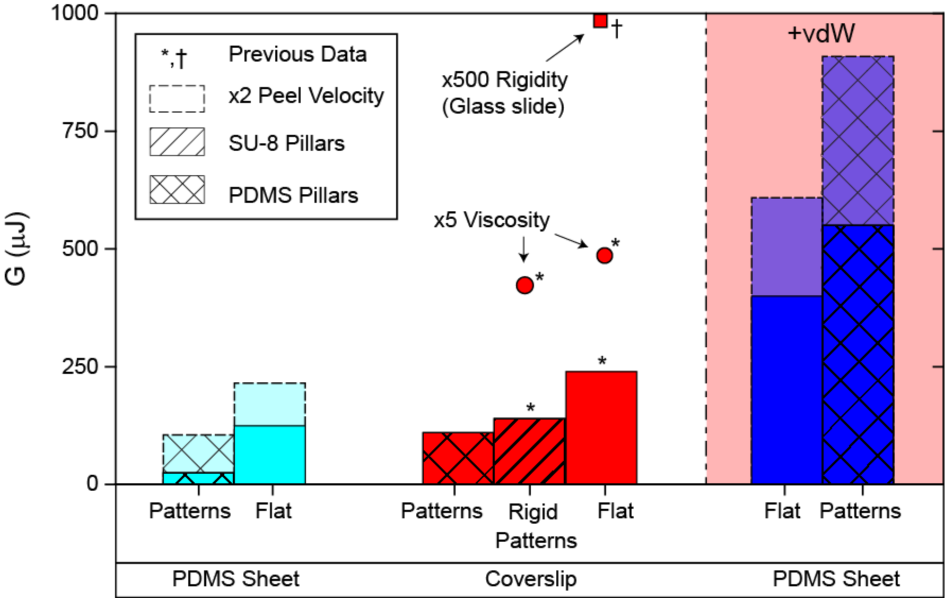

Figure 6.9. Summary of Design Parameters in Peeling in Viscous Fluids. All samples shown are peeled under the same conditions (200 cSt, 300 µm/s) unless otherwise noted. Dashed bars represent the same exact samples and experimental conditions, but peeled at 600 µm/s. Sample rigidity is the same for every sample shown unless otherwise noted, although the PDMS sheets are thicker than the coverslips to match rigidities. The liquid bath in the +vdW (van der Waals adhesion) case is glycerol-water, while in the non-vdW case, it is silicone oil. Data from previous studies are shown as *[73] and †Chapter 5.

When either designing surfaces that may be used in fluid applications, or trying to understand the locomotion of biological systems, it is clear that there are tradeoffs. Unless there are van der Waals or conservative forces, patterns have been shown to reduce the G of our samples. This effect is more severe for softer patterns than rigid. However, once van der Waals forces are introduced, the effect can be negated under the appropriate conditions. Yet this may not be true for all samples and fluids, and it is possible to create regimes where soft patterned samples with van der Waals adhesion would still be lower than their flat counterparts are. We have shown that several different phenomena that can be used to tune adhesion or detachment and their relative magnitude to each other, thus enabling new strategies for creating surfaces that interact with both dissipative and conservative forces.

Chapter 7

Conclusion

7.1. Concluding Remarks

The goal of this thesis was to understand how deformable structured surfaces modulated adhesion in flooded environments. This was done by creating a custom peeling apparatus that allowed us to test a variety of samples in different fluid environments. Our experimental device and choice of samples allowed us to deconstruct a highly coupled system. The evolution of our experiments began with unpatterned samples peeled in a viscous silicone oil bath. We then added rigid structures to create drainage structures on these samples. From there, we remade the same structures from a more deformable material. Finally, we coated these deformable structures in a silicate layer and switched the fluid from silicone to a matched viscosity of glycerol-water to amplify the van der Waals forces. Although analytical expressions were not usually available, we used scaling arguments to provide guidance to predict the relevant forces and works as a function of the material or fluid properties and to predict the regimes of behavior that occurred from the structured surfaces to the structure geometry.

7.2. Contributions

In chapter 3, we peeled unpatterned surfaces in a viscous setting. We demonstrated how the peak detachment force and work change as a function of viscosity and rigidity, and how far the motor must displacement to remove a sample *via* a compliant load cell (the force sensor). We also showed how the extensional compliance lowered the forces for more deformable substrates in samples with the same rigidity (but different Young's modulus and sample thicknesses). While this effect has been shown in dry environments, it has not been demonstrated in purely viscous environments that do not contain any appreciable conservative forces. We have shown that in a fluid, the effect of extensional compliance must be accounted for across the entire length of the sample (during crack propagation), not just during the crack initiation.

In Chapter 4, we showed how structured surfaces altered the approach and detachment dynamics of a patterned sample. By using two different patterns and probing sampling a variety of dwell times and fluid conditions, we were able to correlate when each pattern deviated from a flat surface and relate it to the geometry of the sample by using h_o. We showed that when considering purely viscous forces, structured surfaces reduced detachment forces.

In Chapter 5, we showed how deformable structured surfaces further reduced the detachment forces than their rigid counterparts did. We demonstrated that this is likely an effect of fluid flow around the deformable pillars, and dissimilar to how deformable structures peel in dry environments. Then, we coated these structures in a silicate and switched the fluid to a glycerol-water mixture to amplify van der Waals forces. In the presence of appreciable van der Waals forces, we recovered characteristic seesaw patterns in the force-displacement curves, which indicate crack arrest. This led to structured surfaces having higher detachment than flat surfaces for the first time. By changing the peel velocity, we could identify the viscous contributions separate from the van der Waals contributions.

Between all three chapters, we were able to compare the relative contributions of the viscosity, rigidity, role of structured surfaces, deformation and van der Waals forces. While we demonstrated one case where van der Waals adhesion was able to overcome viscous forces, we also have demonstrated cases where the viscous forces alone exceeded results from the tests with van der Waals forces. In order of weakest to strongest detachment force (with samples of the same rigidity, viscosity and peel velocity), we have 1) a deformable patterned PDMS sheet, 2) a deformable flat PDMS sheet, 3) a rigid patterned coverslip, 4) a rigid unpatterned coverslip 5) a flat PDMS sheet with TEOS and 6) a patterned PDMS sheet with TEOS. We expect other researcher might encounter situations where this list does not necessarily proceed the same order, which can still be compatible with the conclusions we have drawn in each chapter.

7.3. **Future Directions**

From the work presented in this thesis, several future directions to be pursued. We categorize these into three broad categories. 1) Continue investigating additional coupled mechanisms by increasing the complexity of samples 2) Practical realizations of phenomena investigated and 3) Theoretical development.

We have developed an experimental system that has successfully investigated an increasing complex system. It would be a natural extension to increase the complexity of the system conditions to mimic biological systems further. For example, the sample could be made to from a poroelastic material that is impregnated with a second fluid, different from the environmental bath. The bath itself could be changed to a non-Newtonian fluid, or some other complex fluid. This could be useful in investigating protein solutions that serve as a glue in dynamic environments, which may allow samples to bind to a bottom surface but only if the sample and surface create a suitable environment during contact. Finally, it would be relatively straightforward (assuming the fabrication is feasible) to investigate more complex structures such as directional patterns (e.g. triangles) or hierarchical features. In addition, a potentially more relevant system would be if the sheets were made to be thin, such that inertial effects become relevant. In this regime, samples can undulate and vary in morphology. However, it can be challenging to measure these forces since they will be significantly lower and a new sensor would be necessary.

The results of the work here could potentially be used to create novel self-folding devices. Since the majority of this work focused on viscous forces and their mechanical responses, these concepts could be integrated into existing self-folding platforms without altering the chemistry of those systems and offers an additional set of tools. One proposal could be the sequential folding of a cube by changing the pattern features at each face and create two different 3D structures from the same base materials, with the same layer height in each layer. This has been demonstrated in **Figure 7.1** where by designing the structures on the device surface, it is possible to create two different 3D morphologies from a very similar 2D structure. Another interesting, related feature would be to using partial coverage of patterns on the edge of a planar sample to increase the rigidity by folding the sample into a curved cross section, which increases its second area moment of inertia, and thus its rigidity, which further modulates the forces.

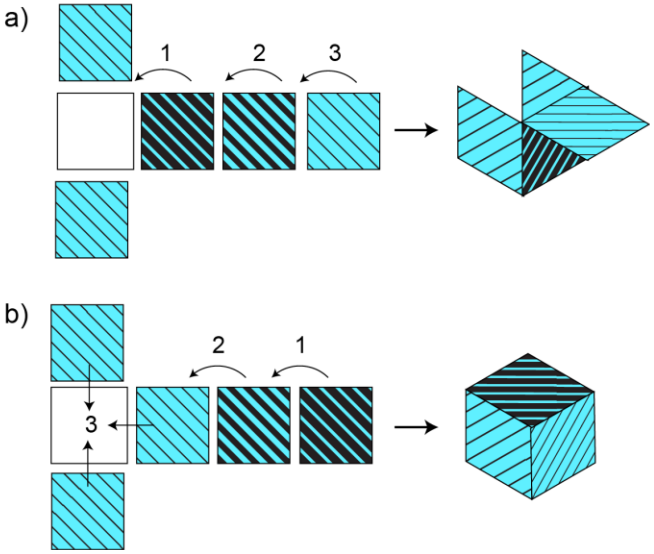

Figure 7.1. Schematic of using drainage channels to sequentially fold a 2D structure. A potential application where the 2D template in both cases is made from the same material and is the same layer thickness, but by controlling the density of drainage channels, different 3D morphologies are realizable and control over the order of folding is also possible.

Finally we can consider potential theoretical developments. Unfortunately, due to the presence of a load cell, we were unsuccesful in providing an analytical or numerical solution in the peeling geometry. One challenge is a tendancy for solutions to bifuricate, and the dependence of the Reynolds equation for planar substrates ($1/h^3$) instead of sphereical ($1/h$) adds complexity due to multiple possible solutions. Currently, no analytical expression exists for the flow around the drianage channels in any direction, and the peeling motion during detachment complicates this further. It is also difficult to simulate this, since the moving fluid-structure boundary can make computations challenging. Theoretical developments of either would be beneficial not only in this study, but to future systems.

References

1. G. Hanna and W. J. P. Barnes, *J. Exp. Biol.*, 1991, **155**, 103-125.
2. T. Endlein, W. J. P. Barnes, D. S. Samuel, N. A. Crawford, A. B. Biaw and U. Grafe, *PLoS One*, 2013, **8**, e73810.
3. R. Kitsomboonloha, S. Morris, X. Rong and V. Subramanian, *Langmuir*, 2012, **28**, 16711-16723.
4. D. J. Norris, E. G. Arlinghaus, L. Meng, R. Heiny and L. Scriven, *Adv. Mater.*, 2004, **16**, 1393-1399.
5. B. J. Nelson, I. K. Kaliakatsos and J. J. Abbott, *Annu. Rev. Biomed. Eng.*, 2010, **12**, 55-85.
6. M. Marder, C.-H. Chen and T. Patzek, *Phys. Rev. E: Stat., Nonlinear, Soft Matter Phys.*, 2015, **92**, 062408.
7. O. K. Baskurt and H. J. Meiselman, Seminars in thrombosis and hemostasis, 2003.
8. K. Autumn, A. Dittmore, D. Santos, M. Spenko and M. Cutkosky, *J. Exp. Biol.*, 2006, **209**, 3569-3579.
9. J. H. Waite, N. H. Andersen, S. Jewhurst and C. Sun, *The journal of adhesion*, 2005, **81**, 297-317.
10. K. Autumn, M. Sitti, Y. A. Liang, A. M. Peattie, W. R. Hansen, S. Sponberg, T. W. Kenny, R. Fearing, J. N. Israelachvili and R. J. Full, *Proceedings of the National Academy of Sciences*, 2002, **99**, 12252-12256.
11. Q. Lin, D. Gourdon, C. Sun, N. Holten-Andersen, T. H. Anderson, J. H. Waite and J. N. Israelachvili, *Proceedings of the National Academy of Sciences*, 2007, **104**, 3782-3786.
12. W. J. P. Barnes, P. J. P. Goodwyn, M. Nokhbatolfoghahai and S. N. Gorb, *J. Comp. Physiol., A*, 2011, **197**, 969-978.
13. W. J. P. Barnes, C. Oines and J. M. Smith, *J. Comp. Physiol., A*, 2006, **192**, 1179-1191.
14. A. Ghatak and M. K. Chaudhury, *J. Adhes.*, 2007, **83**, 679-704.
15. C. K. Hossfeld, A. S. Schneider, E. Arzt and C. P. Frick, *Langmuir*, 2013.

16. N. Canas, M. Kamperman, B. Volker, E. Kroner, R. M. McMeeking and E. Arzt, *Acta Biomater.*, 2012, **8**, 282-288.

17. M. K. Chaudhury, A. Chakrabarti and A. Ghatak, *The European Physical Journal E*, 2015, **38**, 1-26.

18. Y. Wang, C. Dhong and J. Frechette, *Phys. Rev. Lett.*, 2015, **115**, 248302.

19. Y. Wang, G. Pilkington, C. Dhong and J. Frechette, *Curr. Opin. Colloid Interface Sci.*, 2016.

20. C. Creton and M. Ciccotti, *Reports on Progress in Physics*, 2016, **79**, 046601.

21. R. Lacombe, *Adhesion measurement methods: theory and practice*, CRC Press, 2005.

22. Y. Lin, C. Hui and Y. Wang, *J. Polym. Sci. Part B Polym. Phys.*, 2002, **40**, 2277-2291.

23. J. M. Piau, G. Ravilly and C. Verdier, *J. Polym. Sci. Part B Polym. Phys.*, 2005, **43**, 145-157.

24. R. Villey, C. Creton, P.-P. Cortet, M.-J. Dalbe, T. Jet, B. Saintyves, S. Santucci, L. Vanel, D. J. Yarusso and M. Ciccotti, *Soft Matter*, 2015, **11**, 3480-3491.

25. A. Ghatak, L. Mahadevan, J. Y. Chung, M. K. Chaudhury and V. Shenoy, *Proc. R. Soc. A*, 2004, **460**, 2725-2735.

26. J. Y. Chung and M. K. Chaudhury, *J. R. Soc., Interface*, 2005, **2**, 55-61.

27. D. Kaelble, *J. Rheol.*, 1959, **3**, 161-180.

28. J. Bikerman and W. Yap, *J. Rheol.*, 1958, **2**, 9-21.

29. Y. Tian, N. Pesika, H. B. Zeng, K. Rosenberg, B. X. Zhao, P. McGuiggan, K. Autumn and J. Israelachvili, *Proc. Natl. Acad. Sci. U. S. A.*, 2006, **103**, 19320-19325.

30. D. Maugis and M. Barquins, *J. Phys. D: Appl. Phys.*, 1983, **16**, 1843.

31. B. A. Francis and R. G. Horn, *J. Appl. Phys.*, 2001, **89**, 4167-4174.

32. A. Carlson, S. Mandre and L. Mahadevan, *arXiv preprint arXiv:1508.06234*, 2015.

33. L. G. Leal, *Advanced transport phenomena: fluid mechanics and convective transport processes*, Cambridge University Press, 2007.

34. O. Reynolds, *Phil. Trans.*, 1886, **177**, 157-234.

35. B. N. J. Persson, *J. Phys.: Condens. Matter*, 2007, **19**.

36. J. M. Gere and S. Timoshenko, *Cole, Pacific Grove, CA*, 2001.

37. D. F. Moore, *J. Fluid Mech.*, 1964, **20**, 321-330.

38. K. Kendall, *J. Phys. D: Appl. Phys.*, 1975, **8**, 1449-1452.

39. S. Patil, R. Mangal, A. Malasi and A. Sharma, *Langmuir*, 2012, **28**, 14784-14791.

40. J. R. Lister, G. G. Peng and J. A. Neufeld, *Phys. Rev. Lett.*, 2013, **111**, 154501.

41. A. N. Gent and G. R. Hamed, *Rubber Chem. Technol.*, 1979, **52**, 1057-1071.

42. M. Zhang, J. Wu, L. Wang, K. Xiao and W. Wen, *Lab Chip*, 2010, **10**, 1199-1203.

43. A. R. Abate, D. Lee, T. Do, C. Holtze and D. A. Weitz, *Lab Chip*, 2008, **8**, 516-518.

44. J. N. Israelachvili, *Intermolecular and surface forces: revised third edition*, Academic press, 2011.

45. K. Fuller and D. Tabor, Proceedings of the Royal Society of London A: Mathematical, Physical and Engineering Sciences, 1975.

46. B. Thomases and R. D. Guy, *Phys. Rev. Lett.*, 2014, **113**, 098102.

47. R. H. Davis, Y. Zhao, K. P. Galvin and H. J. Wilson, *Philosophical Transactions of the Royal Society of London. Series A: Mathematical, Physical and Engineering Sciences*, 2003, **361**, 871-894.

48. R. Villey, E. Martinot, C. Cottin-Bizonne, M. Phaner-Goutorbe, L. Léger, F. Restagno and E. Charlaix, *Phys. Rev. Lett.*, 2013, **111**, 215701.

49. R. M. Espinosa-Marzal, R. M. Bielecki and N. D. Spencer, *Soft Matter*, 2013, **9**, 10572-10585.

50. A. Ghatak and M. K. Chaudhury, *Langmuir*, 2003, **19**, 2621-2631.

51. F. Kaveh, J. Ally, M. Kappl and H.-J. r. Butt, *Langmuir*, 2014, **30**, 11619-11624.

52. W. J. P. Barnes, *Mrs Bulletin*, 2007, **32**, 479-485.

53. J.-H. Dirks and W. Federle, *Soft Matter*, 2011, **7**, 11047-11053.

54. X. Zhang, R. Jeffrey and E. Detournay, *International journal for numerical and analytical methods in geomechanics*, 2005, **29**, 1317-1340.

55. Y. Kusaka, K.-i. Nomura, N. Fukuda and H. Ushijima, *Journal of Micromechanics and Microengineering*, 2015, **25**, 055022.

56. A. D. Mcewan and G. I. Taylor, *J. Fluid Mech.*, 1966, **26**, 1-&.

57. J. Nase, A. Lindner and C. Creton, *Phys. Rev. Lett.*, 2008, **101**.

58. P. H. Anjos, E. O. Dias, L. Dias and J. A. Miranda, *Phys. Rev. E: Stat., Nonlinear, Soft Matter Phys.*, 2015, **91**, 013003.

59. A. Ghatak, *Mechanics of Peeling of a Flexible Adherent Off a Thin Layer of Adhesive*, 2011.

60. C. Greiner, A. del Campo and E. Arzt, *Langmuir*, 2007, **23**, 3495-3502.

61. F. Yang and J. C. M. Li, *Langmuir*, 2001, **17**, 6524-6529.

62. M. P. Keh and L. G. Leal, *Physical Review Fluids*, 2016, **1**, 013201.

63. M. D. Bartlett, A. B. Croll, D. R. King, B. M. Paret, D. J. Irschick and A. J. Crosby, *Adv. Mater.*, 2012, **24**, 1078-1083.

64. D. R. King and A. J. Crosby, *ACS applied materials & interfaces*, 2015, **7**, 27771-27781.

65. K. R. Shull, D. Ahn, W. L. Chen, C. M. Flanigan and A. J. Crosby, *Macromol. Chem. Phys.*, 1998, **199**, 489-511.

66. M. D. Bartlett and A. J. Crosby, *Langmuir*, 2013, **29**, 11022-11027.

67. J. Nase, O. Ramos, C. Creton and A. Lindner, *The European Physical Journal E*, 2013, **36**, 1-10.

68. S. Ponce, J. Bico and B. Roman, *Soft Matter*, 2015, **11**, 9281-9290.

69. A. Hosoi and L. Mahadevan, *Phys. Rev. Lett.*, 2004, **93**, 137802.

70. M. Argentina, J. Skotheim and L. Mahadevan, *Phys. Rev. Lett.*, 2007, **99**, 224503.

71. A. Ghatak, L. Mahadevan and M. K. Chaudhury, *Langmuir*, 2005, **21**, 1277-1281.

72. A. Majumder, A. Sharma and A. Ghatak, *Langmuir*, 2010, **26**, 521-525.

73. C. Dhong and J. Fréchette, *Soft Matter*, 2015, **11**, 1901-1910.

74. M. Tirumkudulu, W. B. Russel and T. Huang, *Phys. Fluids*, 2003, **15**, 1588-1605.

75. K. R. Shull and C. Creton, *Journal of Polymer Science Part B-Polymer Physics*, 2004, **42**, 4023-4043.

76. I. Johnston, D. McCluskey, C. Tan and M. Tracey, *Journal of Micromechanics and Microengineering*, 2014, **24**, 035017.

77. H. Zeng, B. Zhao, Y. Tian, M. Tirrell, L. G. Leal and J. N. Israelachvili, *Soft Matter*, 2007, **3**, 88-93.

78. H. Zeng, Y. Tian, B. Zhao, M. Tirrell and J. Israelachvili, *Macromolecules*, 2007, **40**, 8409-8422.

79. D. F. Moore, *Wear*, 1965, **8**, 245-263.

80. T. Endlein, A. Ji, D. Samuel, N. Yao, Z. Wang, W. J. P. Barnes, W. Federle, M. Kappl and Z. Dai, *J. R. Soc., Interface*, 2013, **10**, 20120838.

81. W. Federle, W. J. P. Barnes, W. Baumgartner, P. Drechsler and J. M. Smith, *J. R. Soc., Interface*, 2006, **3**, 689-697.

82. I. Scholz, W. J. P. Barnes, J. M. Smith and W. Baumgartner, *J. Exp. Biol.*, 2009, **212**, 155-162.

83. J. M. Smith, W. J. P. Barnes, J. R. Downie and G. D. Ruxton, *J. Comp. Physiol., A*, 2006, **192**, 1193-1204.

84. K. Low, Defense Science Research Conference and Expo (DSR), Singapore, 2011.

85. A. Aydin, *Mar. Pet. Geol.*, 2000, **17**, 797-814.

86. B. N. J. Persson, *J. Phys.: Condens. Matter*, 2007, **19**, 376110_376111-376116.

87. B. N. J. Persson, *J. Adhes. Sci. Technol.*, 2007, **21**, 1145-1173.

88. J. F. Vignola and J. A. Judge, *J. Appl. Phys.*, 2008, **104**, 124305_124301-124308.

89. C. Vančura, J. Lichtenberg, A. Hierlemann and F. Josse, *Appl. Phys. Lett.*, 2005, **87**, 162510_162511-162513.

90. T. Lee, E. Charrault and C. Neto, *Adv. Colloid Interface Sci.*, 2014.

91. G. D. Bixler and B. Bhushan, *Soft Matter*, 2013, **9**, 1620-1635.

92. C. Y. Hui, N. J. Glassmaker, T. Tang and A. Jagota, *J. R. Soc., Interface*, 2004, **1**, 35-48.

93. J. Tamelier, S. Chary and K. L. Turner, *Langmuir*, 2013, **29**, 10881-10890.

94. B. Zhao, N. Pesika, H. Zeng, Z. Wei, Y. Chen, K. Autumn, K. Turner and J. Israelachvili, *J. Phys. Chem. B*, 2008, **113**, 3615-3621.

95. M.-J. Dalbe, S. Santucci, L. Vanel and P.-P. Cortet, *Soft Matter*, 2014, **10**, 9637-9643.

96. J. S. Stefan, K., *Sitz. Kais. Akad. Wiss. Math. Natur. Wien.*, 1874, **69** 713-735.

97. R. Gupta and J. Frechette, *Langmuir*, 2012, **28**, 14703-14712.

98. O. I. Vinogradova and A. V. Belyaev, *J. Phys.: Condens. Matter*, 2011, **23**, 184104.

99. A. A. Potanin and W. B. Russel, *Phys. Rev. E: Stat., Nonlinear, Soft Matter Phys.*, 1995, **52**, 730-737.

100. C. Wu, H. S. Leese, D. Mattia, R. R. Dagastine, D. Y. Chan and R. F. Tabor, *Langmuir*, 2013, **29**, 8969-8977.

101. D.-M. Drotlef, L. Stepien, M. Kappl, W. J. P. Barnes, H.-J. Butt and A. del Campo, *Adv. Funct. Mater.*, 2013, **23**, 1137-1146.

102. E. Cheung and M. Sitti, *J. Adhes. Sci. Technol.*, 2008, **22**, 569-589.

103. A. E. Kovalev, M. Varenberg and S. N. Gorb, *Soft Matter*, 2012, **8**, 7560-7566.

104. K. Li and S. Cai, *Soft Matter*, 2014, **10**, 8202-8209.

105. R. Gupta and J. Fréchette, *J. Colloid Interface Sci.*, 2013, **412**, 82-88.

106. A. T. Al-Halhouli, I. Kampen, T. Krah and S. Büttgenbach, *Microelectron. Eng.*, 2008, **85**, 942-944.

107. S. Patil, A. Malasi, A. Majumder, A. Ghatak and A. Sharma, *Langmuir*, 2011, **28**, 42-46.

108. S. Poivet, F. Nallet, C. Gay and P. Fabre, *Europhys. Lett.*, 2003, **62**, 244.

109. A. J. Crosby, K. R. Shull, H. Lakrout and C. Creton, *J. Appl. Phys.*, 2000, **88**, 2956-2966.

110. M. Varenberg and S. N. Gorb, *Adv. Mater.*, 2009, **21**, 483-+.

111. A. Majumder, A. Ghatak and A. Sharma, *Science*, 2007, **318**, 258-261.

112. A. Ghatak, *Phys. Rev. E: Stat., Nonlinear, Soft Matter Phys.*, 2010, **81**.

113. D. R. Helsel and R. M. Hirsch, *Statistical methods in water resources*, Elsevier, Amsterdam ; New York, 1992.

114. M. Scaraggi and B. N. J. Persson, *Tribol. Lett.*, 2012, **47**, 409-416.

115. C. Cawthorn and N. Balmforth, *J. Fluid Mech.*, 2010, **646**, 327-338.

116. B. Persson and M. Scaraggi, *J. Phys.: Condens. Matter*, 2009, **21**, 185002.

117. C. S. Davis, D. Martina, C. Creton, A. Lindner and A. J. Crosby, *Langmuir*, 2012, **28**, 14899-14908.

118. T. J. Bowman, G. Drazer and J. Frechette, *Biomicrofluidics*, 2013, **7**, 064111.

119. J. Happel, *AIChE J.*, 1959, **5**, 174-177.

120. A. Sangani and A. Acrivos, *Int. J. Multiphase Flow*, 1982, **8**, 193-206.

121. CYTOP Technical Data, www.bellexinternational.com/products/cytop/pdf/cytop-catalog-p8.pdf, Accessed Dec. 14, 2014.

122. XIAMETER® PMX-200 SILICONE FLUID, www.xiameter.com/EN/Products/Pages/ProductDetail.aspx?pid=01013190&lir=X76, Accessed Dec. 14, 2014.

123. Dielectric Properties of Pure Silicone Fluids, www.clearcoproducts.com/pdf/library/Dielectrical-Properties1.pdf, Accessed Dec. 17, 2014.

124. SU-8 2000 Permanent Epoxy Negative Photoresist, www.microchem.com/pdf/SU-82000DataSheet2025thru2075Ver4.pdf, Accessed Dec. 14, 2014.

125. W. J. P. S. Barnes, J. M.; Oines, C.; Mundl, R., *Tire Technology International* 2002, 56-60

126. W. J. P. Barnes, *Tire Technology International*, 1999, 42-47.

127. G. Huber, H. Mantz, R. Spolenak, K. Mecke, K. Jacobs, S. N. Gorb and E. Arzt, *Proc. Natl. Acad. Sci. U. S. A.*, 2005, **102**, 16293-16296.

128. M. Lamblet, E. Verneuil, T. Vilmin, A. Buguin, P. Silberzan and L. Leger, *Langmuir*, 2007, **23**, 6966-6974.

129. B. Zhao, N. Pesika, K. Rosenberg, Y. Tian, H. Zeng, P. McGuiggan, K. Autumn and J. Israelachvili, *Langmuir*, 2008, **24**, 1517-1524.

130. L. F. Boesel, C. Greiner, E. Arzt and A. Del Campo, *Adv. Mater.*, 2010, **22**, 2125-2137.

131. C. Poulard, F. Restagno, R. Weil and L. Léger, *Soft Matter*, 2011, **7**, 2543-2551.

132. J. Iturri, L. Xue, M. Kappl, L. García-Fernández, W. J. P. Barnes, H. J. Butt and A. del Campo, *Adv. Funct. Mater.*, 2015, **25**, 1499-1505.

133. B. N. J. Persson and F. Mugele, *J. Phys.: Condens. Matter*, 2004, **16**, R295-R355.

134. R. H. Davis, D. A. Rager and B. T. Good, *J. Fluid Mech.*, 2002, **468**, 107-119.

135. N. Balmforth, C. Cawthorn and R. Craster, *J. Fluid Mech.*, 2010, **646**, 339-361.

136. T. Salez and L. Mahadevan, *J. Fluid Mech.*, 2015, **779**, 181-196.

137. A. Oláh, H. Hillborg and G. J. Vancso, *Appl. Surf. Sci.*, 2005, **239**, 410-423.

138. R. L. Patrick, *Treatise on adhesion and adhesives*, CRC Press, 1981.

139. D. R. Paretkar, M. D. Bartlett, R. McMeeking, A. J. Crosby and E. Arzt, *The Journal of Adhesion*, 2013, **89**, 140-158.

140. H. Amini, E. Sollier, M. Masaeli, Y. Xie, B. Ganapathysubramanian, H. A. Stone and D. Di Carlo, *Nature communications*, 2013, **4**, 1826.

141. N. Quennouz, M. Shelley, O. du Roure and A. Lindner, *J. Fluid Mech.*, 2015, **769**, 387-402.

142. A. Ghatak, K. Vorvolakos, H. She, D. L. Malotky and M. K. Chaudhury, *J. Phys. Chem. B*, 2000, **104**, 4018-4030.

143. S. Leroy and E. Charlaix, *J. Fluid Mech.*, 2011, **674**, 389-407.

144. L. Y. Clasohm, J. N. Connor, O. I. Vinogradova and R. G. Horn, *Langmuir*, 2005, **21**, 8243-8249.

Out-of-Contact Elastohydrodynamic Deformation Due to Lubrication Forces

[This chapter is reprinted with permission from: Wang, Yumo, Charles Dhong, and Joelle Frechette. "Out-of-contact elastohydrodynamic deformation due to lubrication forces." *Physical review letters* 115.24 (2015): 248302.]

Yumo Wang[1]*, Charles Dhong*[1]*, and Joelle Frechette*[1,2]

[1]Chemical and Biomolecular Engineering Department, and [2]Hopkins Extreme Materials Institute

Johns Hopkins University, Baltimore MD 21218.

A.1. Introduction

Surface and interfacial phenomena in soft matter display complex mesoscale behaviors that are qualitatively different from those encountered in stiff materials, such as elastic instabilities during adhesion[1,2] and Schallamach waves in friction[3,4]. Surface [5-7] or viscous[8] stresses can also lead to elastic deformations that are similar to those observed at fluid interfaces. Elastohydrodynamic deformation (EHD), for example, can cause lift and reduce friction during sliding [9-13] and alter the rheological properties of soft colloidal particles[14-17]. Elastohydrodynamic deformation also modifies the shape of approaching surfaces, a determining factor for the adhesion dynamics to wet or flooded surfaces.[18-21] When studying elastohydrodynamics in soft matter it is a challenge to measure simultaneously the hydrodynamic forces and the deformation, both necessary to understand how contact is reached and the coupling between deformation and viscous dissipation.

To illustrate the importance of elastohydrodynamic deformations, consider the normal approach of a rigid sphere toward a surface with an elastically compliant coating in a Newtonian fluid (Fig. 1A). The hydrodynamic forces lead to deformation of the soft material prior to contact (w(r,t)), as was visualized by Roberts during the settling of a rubber sphere toward a wall.[8] For elastic half-space this problem can be described by the theory of Davis et al.[22,23] derived for the collision of elastic spheres in fluid, and based on the coupling between lubrication forces and linear elasticity. Recent direct measurements of viscous forces in the presence of a soft surface demonstrated that even minute elastic deformations can have a profound effect on the hydrodynamic interactions.[24,25] Therefore, elasticity likely has to be considered when studying slip at a solid-liquid interfaces. The predominance of soft coatings in tribology and adhesion makes the extension of elastohydrodynamic theory to thin supported films technologically relevant, especially to understand how contact is reached in soft matter. The treatment for supported elastic films, however, is challenging and has limited experimental validation. For thin films, the underlying substrate can support a significant fraction of the mechanical stress, which can alter the elastohydrodynamic response from that expected with semi-infinite solids[26,27]. The theory for supported films developed by Charlaix, for instance, elegantly takes advantage of the contribution of the underlying substrate on the hydrodynamic forces to extract the Young's modulus of coatings.[25,27,28] However, the absence of absolute measurement of spatiotemporal separation brings uncertainties to the role played by elasticity on hydrodynamic interactions, especially for the case of thin elastic coatings where our understanding is more limited. Combining visualization of spatiotemporal deformation with force measurements would allow to understand the dynamic of contact formation in soft materials, and to analyze the response of supported films.

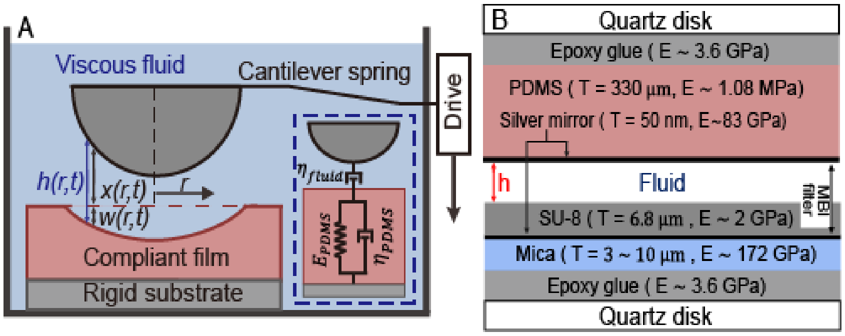

Figure A.0.1. Schematics (not to scale) of (A) the elastohydrodynamic problem with labelled variables (Inset: Kelvin-Voigt model for elastomer viscoelasticity), and (B) Material layers and properties.

In this letter we investigate the role of compliance on the normal approach of a soft surface toward a rigid one in a viscous Newtonian fluid (Fig. 1A). Spatiotemporal deformation profiles and hydrodynamic forces are measured, and compared to an elastohydrodynamic theory for half-space. We find that elastic deformation in the shape of a dimple at the centerpoint prevents contact between approaching surfaces. We also observe that the finite thickness of the elastic layer restricts the deformation and favors contact. Finally, we show that deformation leads to significantly stronger hydrodynamic forces than those observed with rigid surfaces for the same central separation.

A.2. Materials and Methods

Experiments are performed between crossed-cylinders (equivalent to the sphere-plane geometry) using the Surface Forces Apparatus.[29-31] One surface is rigid (bottom in Fig. 1B) and the other is compliant due to the presence of a relatively thick 330 μm PDMS film (polydimethyl siloxane) coated with a 50 nm silver film as a top layer (top in Fig. 1B). Both surfaces are glued on a cylindrical disk (radius, R=1.75 cm). The top silver film facilitates interferometry and prevents swelling in the silicone oil (viscosity, η=0.2Pa*s). An effective Young's modulus of 1.08 ± 0.05 MPa for the PDMS film was obtained by performing in situ contact mechanics experiments[32-34] in silicone oil with the same surfaces (see supporting information 2[35-40]). Because of the underlying rigid substrate [41-45], we expect this modulus to overestimate the intrinsic modulus of the PDMS layer by 15-20%.[46,47] We rely on white light multiple-beam interferometry[30,48,49] to map the local fluid film thickness, h(r,t), within nanometer resolution in the normal direction and micron resolution in the lateral direction.

The dynamic experiments follow the approach of Chan and Horn[50,51], where a disk initially at rest and mounted on a cantilever spring (spring constant k = 165.3 N/m) is driven toward the other surface at a constant drive velocity (V). The spring deflects because of the drag, and the velocity of the surface (v) is always less than the drive velocity. As the surfaces approach, the hydrodynamic forces increase and deform the PDMS film, as evidenced by the flattening at the center, see III-IV in Fig. 2A. Further approach lead to an increase in the fluid pressure near the center causing the formation of a dimple in the elastic film, see V-VII in Fig. 2A.

For the theoretical description we employ the lubrication equation in axisymmetric coordinates ( ) and follow closely the treatment of Ref [22] to couple the fluid pressure distribution (p(r,t)) with linear elasticity of the compliant film. We treat the elastic film as a half-space in the small strain limit (strain of the PDMS coating here,), i.e. we neglect the contribution of the substrate supporting the elastic film. We incorporate a force balance, , where the cantilever spring deflects due to the repulsive viscous forces, . Here h(0,0) is the initial separation at the centerpoint. We neglect the radial shear stress on the film and use the no-slip boundary condition for both surfaces. We obtain a solution numerically using the initial fluid film profile (h(r,0)) from the experiments as the initial condition without any fitting parameters. As a second description we treat the PDMS film as a viscoelastic material with a viscosity η_PDMS, and model the film's response to an applied load as a spring and dashpot in parallel (Kelvin-Voigt model, Fig. 1A). In the viscoelastic description η_PDMS is not known a priori and we iterate to find a single η_PDMS that best describes all the profiles for all drive velocities. (see supporting information [35-40] for details of the model, algorithm, and treatment of viscoelasticity.)

A.3. Results and Discussion

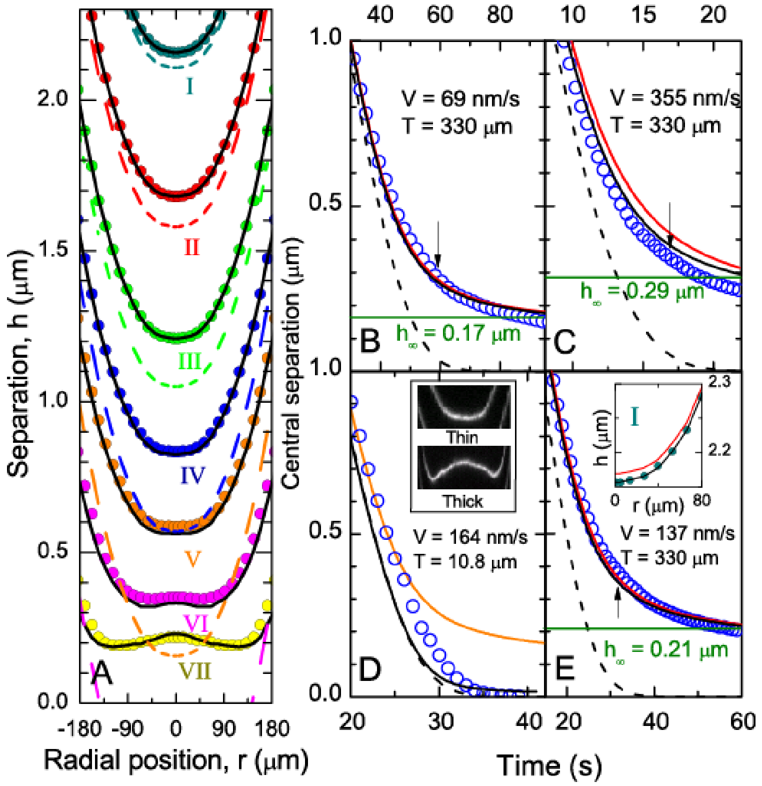

Figure A.2 (A) Experimental and theoretical spatiotemporal surface profile during approach at V = 137 nm/s. The black solid lines correspond to theoretical predictions treating the PDMS films as a viscoelastic solid. Time stamps are: I: t = 3.8s, II: t = 8.8s, III: t = 13.8s, IV: t = 18.8s, V: t = 23.8s, VI: t = 33.8s, and VII: t = 53.8s. Dash lines are for the positions of the corresponding undeformed sphere. (B-E): Temporal central separation for: (B) V = 69 nm/s, (C) V = 355 nm/s, (D) 164 nm/s, and (E) V = 137 nm/s. (B-C): Effect of drive velocity. (D-E): Effect of film thickness. Black solid lines are the same as in (A), dash lines: Reynolds' theory. Red solid lines are predictions treating the elastomer as an elastic solid. Black arrows: time for dimple formation. : Long time predictions (central dh/dt < 1%V). (D): Approach of a thinner PDMS coating (T = 10.9 µm, R = 1.10cm), black rigid line represents predictions for E = 84 MPa. Yellow line represents the predictions for E = 1 MPa. Insets of: (D) shape of fringes for thin (10.9 µm) and thick (330 μm) PDMS film during the approach with hcenter = 150 nm and (E) Effect of viscosity of PDMS on initial surface profile.

The measured and predicted profiles are shown in Fig. 2. In general the elastic solution is sufficient to describe the surface profile but treating the PDMS as a viscoelastic solid gives a better agreement. The viscoelasticity of the PDMS alters the fluid film profile when the rate of strain is the largest (acceleration and deceleration) such as during start up where viscoelastic contributions are visible (inset of Fig. 2E and supporting information [35-40]). For the viscoelastic predictions, a single value of η_PDMS=1.5MPa·s best fits all the profiles at all velocities, in agreement with literature values.[52] In Fig. 2A, the predictions with viscoelasticity predict fluid film thicknesses that are always ±35nm of the measured values at the centerpoint. The error increases with drive velocity: at 355nm/s it is ±48nm, while it is less than 30nm for 69nm/s. For all drive velocities when the two surfaces are close (strong hydrodynamic forces), the observed separation is less than predicted. This error can be understood considering that surfaces appear stiffer as the forces increase due to the finite thickness of the elastomer, and at a constant time stiffer surfaces are always closer than compliant ones (inset of Fig 4).

Elastic deformation prevents the surfaces from reaching contact at all drive velocities investigated, which is captured by the long time predictions (central dh/dt < 1%V, see Fig. 2B,C,E). As the surfaces approach, flattening away from the centerpoint occurs faster than the normal motion toward the surface, which leads to dramatically large forces and prevents contact. Theoretical solutions for the surface separation are not defined at contact regardless of compliance. For rigid materials, predictions diverge at very short-range where irreversibilities such as roughness, size of fluid molecules, and surface forces often favor contact in experiments[53]. In contrast, for a compliant material, the separation at long times is sufficiently large to prevent these mechanisms from playing a role. With compliant surfaces the drive will lead to a broader surface instead of significantly decreasing the central fluid film thickness, at least until non-linear effects occur. Note that contact can be reached under quasi-static condition.

The thickness of the compliant layer plays an important role in determining the spatiotemporal fluid film thickness. We contrast the temporal change in surface separation at the centerpoint of a thick (T=330 µm, Fig. 2E) and thin (T=10.9 µm, Fig. 2D) PDMS films for similar drive velocities. Both films have the same bulk mechanical properties, however the effective modulus is much larger (E=84 MPa) for the thin film because of incompressibility and apparent stiffening due to the underlying rigid substrate (supporting information[35-40])[54,55]. For the thin film, as the hydrodynamic forces increase, the stress becomes increasingly supported by the rigid substrate. As a result, the temporal fluid film thickness gradually transitions from being the one predicted for a compliant material (E=1MPa) to that of a rigid one (see predictions for the two moduli in Fig. 2D). We find that the effective stiffening suppresses the formation of a dimple (within our spatial resolution) in the elastic film, and that contact can be reached in a fashion similar than for rigid materials. Such a transition to a rigid-like behavior is not observed with the thicker film. This stiffening effect is well-characterized for contact mechanics experiments[45]. Our work shows how the finite thickness of the elastic film gradually alters the deformation profile from that of a semi-infinite compliant material as the surfaces approach and how it favors contact. Increasing the modulus in the model will not give better agreement with experiments, and always make the far-field predictions significantly worse (see supporting information[35-40]). An alternative treatment would be to use a solution for arbitrary axisymmetric pressure distribution for a finite thickness elastic layer, such as in Refs [26,27], to obtain a solution valid at all h. A simplified scaling argument treating the deformation solely as shear, such as in Ref [27] could also work close to contact but not for the far-field. The importance of film thickness on the force required to make contact has profound implications for hydrodynamic interactions with soft materials and coatings, such as in biological systems, tribology, adhesion, and rheology.

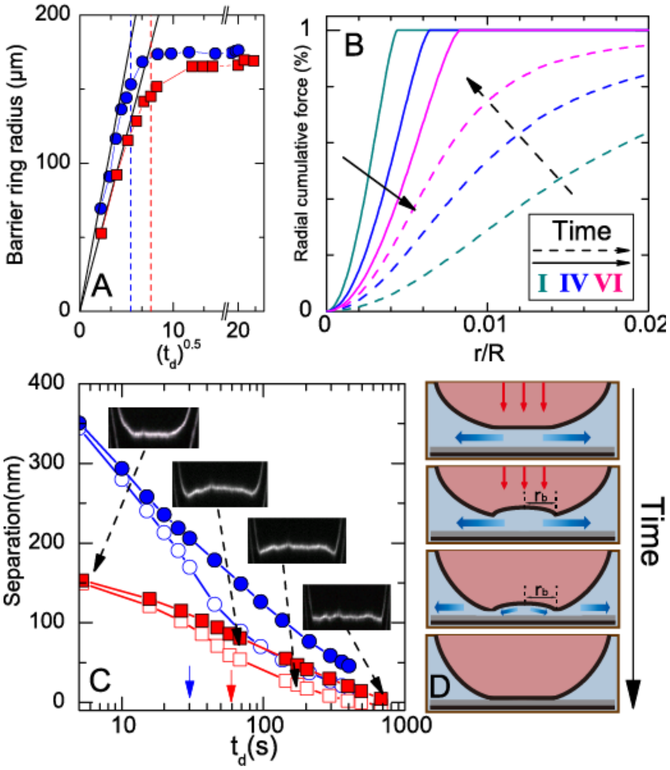

Figure A.3. (A) Growth of barrier ring radius (rb). Squares: V = 69 nm/s, circles: V = 137 nm/s. td (s) is the time elapsed after center curvature of the elastomer becomes negative.

Black solid lines: . Vertical dashed lines indicate when the motor stopped. (B) Radial cumulative force (%) as a function of r/R for V = 137 nm/s. The roman numerals represent the same times as those of Fig. 2A. Solid lines correspond to the relative cumulative force results from a spherical indenter with the same load as that in EHD (Dashed lines), calculated from Hertz contact mechanics. (C) Centerpoint (solid) and edge (open) separation after dimple formation (circles: V=137 nm/s, squares: V=69 nm/s). Inset: Corresponding interference fringes for V = 69 nm/s. Solid arrows: motor stop time for V = 137 nm/s and V = 69 nm/s. (D) Schematic showing formation and relaxation of dimples with a barrier ring rb.

The formation of dimple—a bell of liquid trapped around the centerpoint— is observed as the force increases (Fig. 2A). Once formed (td=0) the growth of dimples forming a barrier ring follows the same geometric scaling as the one observed for fluid droplets, and is independent of materials properties (, Fig. 3A)[56,57]. This scaling implies that beyond td the fluid film thickness remains essentially constant while the increase in pressure is almost solely accommodated by elastic deformation. The appearance of a dimple requires the fluid pressure to be highly concentrated near the centerpoint and our model (Fig. 3B) shows that as the force increases, the fluid pressure distribution becomes increasingly more concentrated near the center. We compare the radial cumulative force with the one predicted based on a Hertzian contact for the same force (Fig. 3B). For a given force, a spherical indenter always leads to a narrower pressure distribution than the elastohydrodynamic case. As the force increases, however, the contact area based on indentation increases while the elastrohydrodynamic pressure distribution becomes shaper and significantly more concentrated near the centerpoint (compare the radial cumulative force at the Hertz contact radius for the three cases shown in Fig. 3B).

If we stop the motor (near the limit of the range of the motor), the surface velocity decreases but does not stop because of the stored energy in the cantilever. The dimple slowly relaxes after the motor stops (see Fig. 3C), and after a long time contact can be reached first at the edge of the ring, followed later by near contact (to within 10nm) at the centerpoint (Fig. 3C). This process is very slow (»100s): the fluid has to drain through the edge of the dimple as the pressure drop between the center and the surrounding decreases. During this relaxation a fluid pocket can be trapped at the center while contact is reached at the edge.

The measured hydrodynamic forces and predictions for soft and rigid surfaces are shown in Fig. 4. The experimental points are calculated based on the measured fluid film profile and predictions for the model treat the PDMS film as a viscoelastic solid. To calculate the hydrodynamic force from our experimental data we used the prediction for w at the centerpoint (see supporting information [35-40]). In general our experiments show excellent agreement with predictions over all the velocities, with the largest error present for the fastest drive velocity and close to contact. When comparing the hydrodynamic forces between soft and rigid surfaces we see that predictions based on rigid surfaces underestimate the real force for all fluid film thicknesses. In contrast, Reynolds theory always overestimates the force at a given time (inset of Fig. 4). For a given fluid film thickness the deformed surface is flatter, giving rise to larger hydrodynamic repulsion than for rigid surfaces. In contrast, at a given time t rigid surfaces are always closer to contact and the force is higher than for a deformable surface. We also observe systematic deviation in the hydrodynamic forces at small h and at long times that are attributed to the effective stiffening caused by the rigid underlying substrate. If we compare with AFM experiments where only and are known, predictions based on Reynolds theory would overestimate the measured force: for the same a rigid surface has a smaller separation ( ) than the compliant surface. Thus the rigid case predicts a larger force than measured because of the different , as shown by Ref [24].

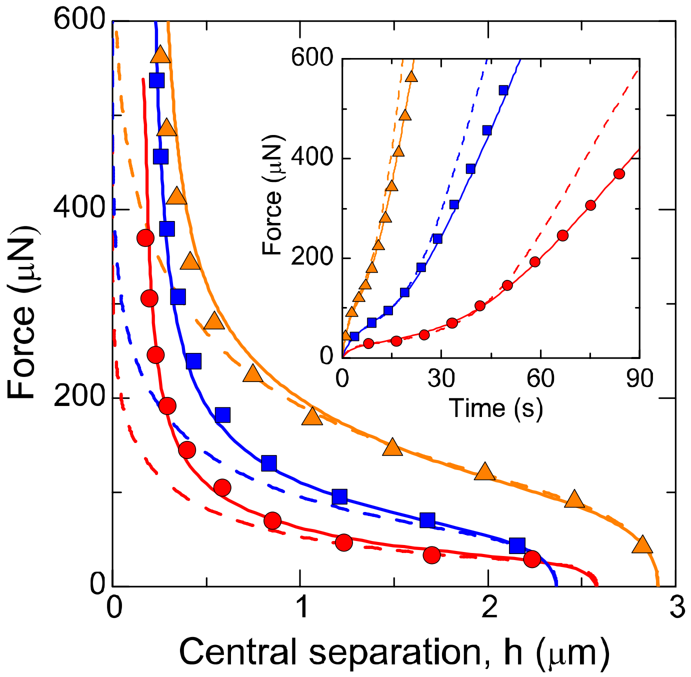

Figure A.4. Repulsive elastohydrodynamic force as a function of central separation, h. Circles: V = 69 nm/s, squares: V = 137 nm/s, triangles: V = 355 nm/s. Dash lines: predictions for rigid surfaces, solid lines: predictions for compliant surfaces treating the elastomer as a viscoelastic solid. Inset: corresponding force as a function of time.

In summary, we characterized the spatiotemporal deformation of a compliant film during the normal drainage of fluid from a narrowing gap. For a thick elastic film (approx. half-space) we observe that elastic deformation in the form of a dimple prevents the surfaces from reaching contact. For a thinner elastic the formation of the dimple is suppressed and contact can be reached because the stress is supported by the underlying substrate. We find that the growth of the dimples in the elastic films is nearly independent of the mechanical properties of the film. Finally we find that at a given time elastic compliance leads to weaker forces while it leads to stronger forces at a given fluid film thickness. Measuring absolute surface separation is critical when working with soft materials, such as in biological systems or in the lubrication of surfaces with compliant coatings of a finite thickness.

A.4. Acknowledgements

This work is partially supported by the Office of Naval Research – Young Investigator Award (N000141110629), by the Donors of the American Chemical Society Petroleum Research Fund under Grant 51803-ND5, the Hopkins Extreme Materials Institute (HEMI), and NSF-CMMI 1538003.

A.5. References

[1] A. Ghatak and M. K. Chaudhury, J. Adhes. 83, 679 (2007).
[2] S. Yang, K. Khare, and P. C. Lin, Adv. Funct. Mater. 20, 2550 (2010).
[3] C. J. Rand and A. J. Crosby, J. Appl. Phys. 106, 4, 064913 (2009).

[4] K. Vorvolakos and M. K. Chaudhury, Langmuir 19, 6778 (2003).

[5] J. S. Wexler, T. M. Heard, and H. A. Stone, Phys. Rev. Lett. 112, 5, 066102 (2014).

[6] L. A. Lubbers, J. H. Weijs, L. Botto, S. Das, B. Andreotti, and J. H. Snoeijer, J. Fluid Mech. 747, 12, R1 (2014).

[7] R. W. Style, R. Boltyanskiy, Y. L. Che, J. S. Wettlaufer, L. A. Wilen, and E. R. Dufresne, Phys. Rev. Lett. 110, 5, 066103 (2013).

[8] A. Roberts, J. Phys. D: Appl. Phys. 4, 423 (1971).

[9] D. Dowson, Wear 190, 125 (1995).

[10] A. Gopinath and L. Mahadevan, in Proceedings of the Royal Society of London A: Mathematical, Physical and Engineering Sciences (The Royal Society, 2011), p. rspa20100228.

[11] J. M. Skotheim and L. Mahadevan, Phys. Fluids 17, 092101 (2005).

[12] M. Scaraggi, G. Carbone, B. N. J. Persson, and D. Dini, Soft Matter 7, 10395 (2011).

[13] G. A. Ateshian, H. Wang, and W. M. Lai, J. Tribol. 120, 241 (1998).

[14] J. R. Seth, L. Mohan, C. Locatelli-Champagne, M. Cloitre, and R. T. Bonnecaze, Nat. Mater. 10, 838 (2011).

[15] A. Ikeda, L. Berthier, and P. Sollich, Phys. Rev. Lett. 109, 018301 (2012).

[16] M. Gross, T. Kruger, and F. Varnik, Soft Matter 10, 4360 (2014).

[17] S. Adams, W. Frith, and J. Stokes, J. Rheol. (1978-present) 48, 1195 (2004).

[18] J. Iturri, L. Xue, M. Kappl, L. García-Fernández, W. J. P. Barnes, H. J. Butt, and A. del Campo, Adv. Funct. Mater. (2015).

[19] B. N. J. Persson, J. Phys. Condens. Matter 19, 16, 376110 (2007).

[20] L. Heepe and S. N. Gorb, Annu. Rev. Mater. Res. 44, 173 (2014).

[21] C. Dhong and J. Frechette, Soft Matter 11, 1901 (2015).

[22] R. H. Davis, J.-M. Serayssol, and E. Hinch, J. Fluid Mech. 163, 479 (1986).

[23] G. Barnocky and R. H. Davis, Phys. Fluids 31, 1324 (1988).

[24] F. Kaveh, J. Ally, M. Kappl, and H. J. Butt, Langmuir 30, 11619 (2014).

[25] S. Leroy, A. Steinberger, C. Cottin-Bizonne, F. Restagno, L. Leger, and E. Charlaix, Phys. Rev. Lett. 108, 264501 (2012).

[26] X. Zhao and R. Rajapakse, Int. J. Eng. Sci. 47, 1433 (2009).

[27] S. Leroy and E. Charlaix, J. Fluid Mech. 674, 389 (2011).

[28] R. Villey, E. Martinot, C. Cottin-Bizonne, M. Phaner-Goutorbe, L. Léger, F. Restagno, and E. Charlaix, Phys. Rev. Lett. 111, 215701 (2013).

[29] D. Tabor and R. H. S. Winterton, Proc. R. Soc. London, Ser: A 312, 435 (1969).

[30] J. N. Israelachvili, J. Colloid Interface Sci. 44, 259 (1973).

[31] J. N. Israelachvili et al., Rep. Prog. Phys. 73, 036601 (2010).

[32] K. L. Johnson, K. Kendall, and A. D. Roberts, Proc. R. Soc. London, Ser. A 324, 301 (1971).

[33] M. K. Chaudhury and G. M. Whitesides, Science 255, 1230 (1992).

[34] K. Khanafer, A. Duprey, M. Schlicht, and R. Berguer, Biomed. Microdevices 11, 503 (2009).

[35] For PDMS preparation, calculation of the effective modulus and layering effect, determination of the deformation and numerical algorithm, see Supplemental Material, which include Refs.[36-40].

[36] J. N. Lee, C. Park, and G. M. Whitesides, Anal. Chem. 75, 6544 (2003).

[37] M. Heuberger, Rev. Sci. Instrum. 72, 1700 (2001).

[38] G. Lian, M. J. Adams, and C. Thornton, J. Fluid Mech. 311, 141 (1996).

[39] J.-M. Sérayssol, Dynamic deformation and rebound of particles during filtration and coagulation 1985).

[40] B. Hughes and L. White, Q. J. Mech. Appl. Math. 32, 445 (1979).

[41] I. Sridhar, K. L. Johnson, and N. A. Fleck, J. Phys. D: Appl. Phys. 30, 1710 (1997).

[42] K. L. Johnson and I. Sridhar, J. Phys. D: Appl. Phys. 34, 683 (2001).

[43] P. M. McGuiggan, J. S. Wallace, D. T. Smith, I. Sridhar, Z. W. Zheng, and K. L. Johnson, J. Phys. D: Appl. Phys. 40, 5984 (2007).

[44] F. K. Yang, W. Zhang, Y. G. Han, S. Yoffe, Y. C. Cho, and B. X. Zhao, Langmuir 28, 9562 (2012).

[45] E. Barthel and A. Perriot, J. Phys. D: Appl. Phys. 40, 1059 (2007).

[46] K. R. Shull, Mater. Sci. Eng. R-Rep. 36, 1 (2002).

[47] E. K. Dimitriadis, F. Horkay, J. Maresca, B. Kachar, and R. S. Chadwick, Biophys. J. 82, 2798 (2002).

[48] S. Tolansky, Multiple-Beam Interferometry of surfaces and films (Oxford University Press, London, 1948).

[49] R. Gupta and J. Fréchette, J. Colloid Interface Sci. 412, 82 (2013).

[50] D. Y. C. Chan and R. G. Horn, J. Chem. Phys. 10, 5311 (1985).

[51] R. Gupta and J. Frechette, Langmuir 28, 14703 (2012).

[52] S. T. Choi, S. J. Jeong, and Y. Y. Earmme, Scr. Mater. 58, 199 (2008).

[53] R. Horn and J. Israelachvili, Macromolecules 21, 2836 (1988).

[54] A. Perriot and E. Barthel, J. Mater. Res. 19, 600 (2004).

[55] E. Barthel, A. Perriot, A. Chateauminois, and C. Fretigny, Philos. Mag. 86, 5359 (2006).

[56] J. N. Connor and R. G. Horn, Farad. Discuss. 123, 193 (2003).

[57] R. Manica, J. N. Connor, S. L. Carnie, R. G. Horn, and D. Y. C. Chan, Langmuir 23, 626 (2007).

Appendix B

Rotation and translation of a non-colloidal particle down a microstructured incline at low Reynolds numbers

[adapted from a manuscript under review]

*Brian K. Ryu, Charles Dhong, and Joëlle Fréchette**

Department of Chemical and Biomolecular Engineering, Johns Hopkins University,
Baltimore, Maryland 21218, United States

B.1. Introduction

Controlling hydrodynamic interactions between a particle and a rough or patterned surface is of particular interest in rheology [1], separation [2], friction [3], drag reduction [4], and adhesion [5]. In particular, there is a recent focus on understanding the flow characteristics near bio-inspired microstructured surfaces, due to their superior drag reduction, anti-fouling, adhesion, or friction properties [6-8]. For example, materials designed to mimic the microstructure found on shark skin are currently employed for drag reduction and anti-fouling [9-11]. Similarly, the soft microscale pillars on the tree frog toe pads gives them strong adhesion and friction forces that enhance the dynamics of underwater adhesion [12-15]. Bio-inspired materials based on the tree frog toe pads could help design better underwater gripping materials for applications in areas as diverse as robotics, transportation, or for the biomedical industry [16-19]. Similarly, microstructured microfluidic channels significantly increase particle-surface interactions, showing prospects in rare cell detection from heterogeneous suspensions [20,21]. While it is well-established that surface microstructures modulate contact or near contact interactions in fluid environments, there is a strong need to better understand how microstructures influence friction, drag and adhesion properties.

The measurement of hydrodynamic drainage forces using the atomic force microscope or the surface forces apparatus allows to study how microstructured or rough surfaces alter the hydrodynamic interactions of an approaching sphere [22-28]. In general, wetting microstructures lead to a reduction in the hydrodynamic force acting on an approaching surface, similar to that observed for slip on non-wetting surfaces [27,29,30]. For example, Vinogradova and coworkers showed that introducing an effective no-slip plane shifted below the top of the textured roughness (i.e. a shifted plane) can be employed to describe the fluid drainage caused by the approach of a smooth sphere [31-33]. Yet, the studies note the inconsistency of the shifted plane model in the thin channel limit, where the sphere is asymptotically close to the surface. Pilkington et al. address this issue by invoking a separation dependent shifted plane to account for the different flow regimes as the fluid drains during the approach of the sphere to the microstructured surface [26]. Similarly, Chastel and Mongruel developed an alternative model by approximating the medium of microstructures and the surrounding fluid as a second fluid with a higher effective viscosity than the original fluid and accounting for viscous dissipation [34]. The model accurately describes the motion of an approaching sphere when the gap between the sphere and the top of the microstructures is comparable to the dimensions of the microstructures. However, normal force measurements do not provide any information on the lateral (friction, rotation) forces caused by the microstructure. It is also challenging to interpret drainage force measurements when the sphere is asymptotically close to the microstructure surface, or to incorporate effects due to solid-solid contacts.

In contrast, previous studies have shown that the rolling motion of a non-colloidal sphere down an inclined plane is strongly affected by surface roughness and other contact forces [35-37]. In particular, surface asperities introduce torque and cause the sphere to rotate as well as slip as it descends an inclined plane (see Figure 1). As a result, efforts to understand how surface roughness leads to deviation from the ideal case of smooth surfaces have led to models of hydrodynamic roughness and interactions between spheres and surfaces at low Reynolds numbers [38]. Goldman et al. studied the motion of a non-colloidal sphere asymptotically close to a smooth plane wall in a viscous fluid [39,40]. These studies obtained asymptotic solutions to hydrodynamic resistance functions for separations less than 4% of the sphere radius in the form of logarithmic functions, predicting that a mathematically smooth sphere tangent to a smooth surface would not move parallel to the wall due to a contact singularity.

Smart and Leighton implemented the theory of Goldman et al. to describe the motion of microscopically rough spheres down an inclined plane [35]. In their approach the sphere maintains a constant separation from the smooth surface that is equal to the height of the surface asperities, and contact between the asperities and the surface leads to friction. The theory is developed under the assumption that the roughness features only cover a small fraction of the surface, and thus only serve to maintain a consistent separation. The model has two fitting parameters to relate the measured velocity to the resistance functions: the fluid gap between the sphere and the surface (normalized by the sphere radius) and an effective coefficient of friction. The framework of Smart and Leighton successfully described the measurements of the translational and rotational velocities of a rough sphere rolling down an incline in a viscous fluid driven by gravitational force. These experiments demonstrated that spheres placed on an incline rolled without slipping at small angles of inclination with the dimensionless velocity of a non-slipping sphere determined by the gap height between the sphere and the surface. However, as the angle increases and reaches a critical angle, determined by the coefficient of friction between the two surfaces, the mode of motion begins to include slipping.

Further investigations by Prokunin and Williams examined the motion of a rough sphere rolling down a smooth glass tube over a wide range of Reynolds numbers [41,42]. The studies introduced a method for measuring the sliding coefficient of friction of a sphere on an incline. Their measurements showed that, for the same material, larger spheres experienced significantly smaller coefficients of friction than smaller spheres. Prokunin also observed that the apparent gap between a smooth rolling sphere and a smooth incline, calculated from the rotational and translational velocities of the sphere, was significantly larger than the actual measured roughness. Galvin et al. addressed this discrepancy between the measured and effective gap height with multiple scales of roughness [43]. Their work extends the model of Smart et al. to incorporate two macroscopic roughness scales that induce liftoff to calculate a time-averaged hydrodynamic roughness that depends on the sizes of roughness scales and the angle of inclination. Zhao et al. later showed that analogous results are obtained if the roughness elements are placed on the plane, instead of the sphere [36]. All these studies rely on the assumption that the roughness features on the sphere or incline are randomly dispersed asperities that only sparsely cover the surface. These assumptions simplify the analysis by neglecting the hydrodynamic interactions within the roughness elements, and imply that surface asperities only affect the hydrodynamic resistance forces acting on the sphere by manipulating the separation between the sphere and the surface.

The formalism developed for the motion of a sphere on rough surfaces has not been tested or validated for well-defined, wettable periodic microstructures with high surface coverage. In particular, the surface coverage dependence of the effective gap height experienced by the spheres has not been characterized systematically and is poorly understood. Similarly, the current theoretical treatment for rolling motion has no distinction for surface microstructures with different geometries, for example between wells and pillars of the same surface coverage and feature heights. Expanding the treatment and understanding of the rolling motion of non-colloidal spheres on rough inclined planes to the rolling motion on well-defined microstructured surfaces would allow to study the motion on bio-inspired surfaces. In addition, rolling measurements on microstructured surfaces would complement direct friction or adhesion force measurements as well as drainage force measurements, especially for drag or friction reduction applications.

In this study, we examine the motion of a smooth sphere rolling down a microscopically textured surface. We measure independently the rotational and translational velocities of the spheres as they roll down inclined planes at various angles of inclination. We compare and contrast the rolling motion on surfaces patterned with hexagonal arrays of micropillars, microwells, as well as on flat surfaces. We employ the model introduced by Smart et al. [35] to obtain an effective gap height and coefficient of friction for all the surfaces investigated. We observe an exponential dependence on the effective gap height experienced by the spheres on the surface fraction. We then compare the effective gap heights to values predicted by a simple model we developed that is based on the superposition of resistance functions to relate the effective gap heights experienced by a rolling sphere on a textured surface to the surface coverage of the micropatterned features. We also see that the effective coefficient of friction is much larger on a surface with micropillars than on a surface with microwells for a given area fraction and feature height, consistent with direct friction force measurements on lubricated contacts reported in the literature [44].

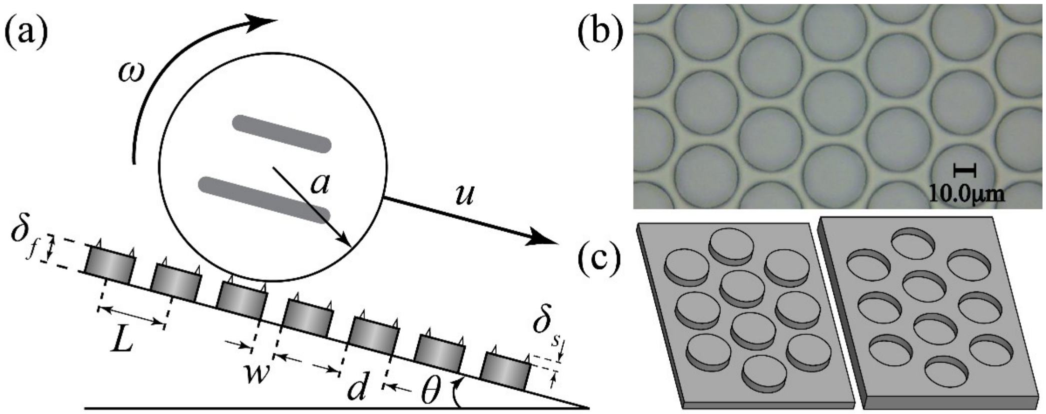

Figure B.0.1. (a) Sketch of a sphere rolling with a translational velocity u and angular velocity Ω on a microstructured incline with feature height δ_f, diameter d, and spacing w. The top plane of the microstructures have an inherent roughness height of δ_s. Two parallel lines of different lengths are drawn on the side to track the angular orientation of the sphere. (b) Bright-field microscopy top-view image of an SU-8 microwell array (d = 30 μm, w = 3 μm). (c) Schematic of micropillar (left), and microwell (right) array.

B.2. Theoretical Development

A. Motion of a Sphere on a Rough Surface

We describe the steady rolling motion of a smooth sphere of radius a down a rough plane with an angle of inclination θ in a viscous, Newtonian fluid of viscosity μ, with a translational velocity u and an angular velocity ω. To do so, we follow the treatment of Smart et al. and Zhao et al., detailed here for clarity [35,36]. We assume that the sphere is non-colloidal and negatively buoyant with a density ρ_p greater than that of the fluid ρ_f, where density difference is Δρ. We further assume that inertial forces are negligible (i.e. Stokes flow), and ignore colloidal interactions such as van der Waals forces. Because the equations of motion under Stokes flow are linear, the force and torque balance on the sphere moving at steady state are:

$$F_G = F_T + F_R + F_f \tag{1}$$

$$aF_f = T_T + T_R, \tag{2}$$

where F_G is the gravitational force on the sphere, F_T, T_T, F_R, and T_R are resistance forces and torques caused by the translational and rotational motion of the sphere, and F_f is the frictional force on the point of contact. The term on the left side of Eq. (2) is the torque exerted on the point of contact due to friction between the sphere and the surface. The net weight, or gravitational force, tangent to the direction of the incline is $F_G = \frac{4}{3}\pi a^3 g\Delta\rho\sin(\theta)$ and the frictional force is $F_f = \frac{4}{3}\pi a^3 g\Delta\rho\cos(\theta)\mu_f$, where μ_f

is the coefficient of friction. We assume here that the coefficients of rolling and sliding friction between the sphere and plane are equal. Hence, the force and torque balance are re-written respectively as:

$$\frac{4}{3}\pi a^3 g\Delta\rho \sin\left(\theta\right) = 6\pi\mu a\left(uF_T^* + a\omega F_R^*\right) + \frac{4}{3}\pi a^3 g\Delta\rho\cos\left(\theta\right)\mu_f, \tag{3}$$

$$\frac{4}{3}\pi a^4 g\Delta\rho\cos\left(\theta\right)\mu_f = 8\pi\mu a^2\left(uT_T^* + a\omega T_R^*\right), \tag{4}$$

where are resistance functions that are non-dimensionalized as [39]:

$$F_T = 6\pi\mu a u F_T^*, \tag{12}$$

$$T_T = 8\pi\mu a^2 u T_T^*, \tag{13}$$

$$F_R = 6\pi\mu a^2 \omega F_R^*, \tag{14}$$

$$T_R = 8\pi\mu a^3 \omega T_R^*. \tag{15}$$

Following Smart et al., we define the dimensionless translational (U) and rotational (Ω) velocities as:

$$U = u / U_S \sin\left(\theta\right), \tag{9}$$

$$\Omega = a\omega / U_s \sin\left(\theta\right), \tag{10}$$

where U_S is the Stokes settling velocity, defined as $U_S = \frac{2}{9}\left(a^2 g\Delta\rho / \mu\right)$. The force balances of Eqs. (3) – (4) reduce to the following dimensionless form:

$$1 = UF_T^* + \Omega F_R^* + \mu_f \cot\left(\theta\right), \tag{11}$$

$$\mu_f \cot(\theta) = \frac{4}{3}\left(UT_T^* + \Omega T_R^*\right), \tag{12}$$

In addition, the analysis of Galvin et al. [43] demonstrates that the above force and torque balance (Eqs. (11) – (12)) simplify as:

$$U = \Omega = \frac{1}{F_T^* + F_R^* + \frac{4}{3}\left(T_T^* + T_R^*\right)}, \tag{13}$$

when the sphere is rolling without slipping, and as:

$$\Omega = \frac{1 - \mu_f \cot(\theta)\left[1 + \frac{3}{4} F_T^* / T_T^*\right]}{F_R^* - T_R^* F_R^* / T_T^*}, \tag{14}$$

$$U = \frac{\frac{3}{4}\mu_f \cot(\theta) - \Omega T_R^*}{T_T^*}, \tag{15}$$

when the sphere is rolling with slipping. At low angles of inclination, the sphere rolls without slipping. As θ increases, the sphere starts to slip when the following criterion applies:

$$\cot(\theta) < \frac{\frac{4}{3}\left(T_T^* + T_R^*\right)}{\mu_f [F_T^* + F_R^* + \frac{4}{3}\left(T_T^* + T_R^*\right)]}. \tag{16}$$

We define the critical angle θ$_c$ as the angle of inclination in which the rolling particle starts to slip:

$$\cot\left(\theta_c\right)=\frac{\frac{4}{3}\left(T_T^*+T_R^*\right)}{\mu_f\left[F_T^*+F_R^*+\frac{4}{3}\left(T_T^*+T_R^*\right)\right]}. \tag{17}$$

The dimensionless resistance functions for a sphere asymptotically near a plane wall with separation δ have been developed by Goldman et al. [39]:

$$F_T^*=-\frac{8}{15}\ln\left(\frac{\delta}{a}\right)+0.9588, \tag{16}$$

$$T_T^*=\frac{1}{10}\ln\left(\frac{\delta}{a}\right)+0.1895, \tag{17}$$

$$F_R^*=\frac{2}{15}\ln\left(\frac{\delta}{a}\right)+0.2526, \tag{18}$$

$$T_R^*=-\frac{2}{5}\ln\left(\frac{\delta}{a}\right)+0.3817, \tag{19}$$

where $T_T^*=\frac{3}{4}F_R^*$ due to the reciprocal theorem of Stokes flow. In the absence of the nearby plane, T_T^* and F_R^* are both equal to zero [45].

B. Motion of a Sphere on a Microtextured Surface

We now consider the role of a microtextured wall on the hydrodynamic resistance of a sphere. The geometry of the patterned features and solid fraction at the top of the wall surface characterizes the microtextured wall. For a hexagonal array of micropillars of diameter d and spacing w (see Figure 1), the solid fraction or areal coverage ϕ of the microstructures is:

$$\phi = \frac{\pi\left(d+w\right)^2}{2\sqrt{3}d^2}, \tag{20}$$

and for a hexagonal array of microwells of diameter d and spacing w, ϕ is:

$$\phi = 1 - \frac{\pi\left(d+w\right)^2}{2\sqrt{3}d^2}. \tag{21}$$

We extend the treatment of Staben et al. for the motion of particles between two narrow parallel walls to model the motion of a particles on microstructured surfaces [46,47]. In contrast to having the particle being sandwiched by the two walls, here one wall is located at the top of the features and the other at the bottom. Yet, we still assume that both walls are still asymptotically close to the particle. We propose, as a first order approximation, that a simple linear superposition of one-wall force functions can model the resistance function due to the microstructures. For a sphere near a plane surface with microstructures of height δ_f, solid fraction ϕ, and an inherent roughness at the top plane of the microstructures δ_s, we represent the resistance functions as a sum of lubrication formulas for the plane above and below the microstructures. This superposition results in the following forces and torques:

$$F_T^* = \phi\left(-\frac{8}{15}\ln\left(\frac{\delta_s}{a}\right)\right) + \left(1-\phi\right)\left(-\frac{8}{15}\ln\left(\frac{\delta_f}{a}\right)\right) + 0.9588, \tag{22}$$

$$T_T^* = \phi\left(\frac{1}{10}\ln\left(\frac{\delta_s}{a}\right)\right) + \left(1-\phi\right)\left(\frac{1}{10}\ln\left(\frac{\delta_f}{a}\right)\right) + 0.1895, \tag{23}$$

$$F_R^* = \phi\left(\frac{2}{15}\ln\left(\frac{\delta_s}{a}\right)\right) + (1-\phi)\left(\frac{2}{15}\ln\left(\frac{\delta_f}{a}\right)\right) + 0.2526, \quad (24)$$

$$T_R^* = \phi\left(-\frac{2}{5}\ln\left(\frac{\delta_s}{a}\right)\right) + (1-\phi)\left(-\frac{2}{5}\ln\left(\frac{\delta_f}{a}\right)\right) + 0.3817, \quad (25)$$

where the first terms on the right hand side of Eqs. (24) – (27) correspond to the plane located on the top of the structures and the second terms correspond to the plane below the structures. Because Eqs. (24) – (27) are based on the model by Goldman et al. [39], in which spheres are asymptotically close to the plane, it is assumed that the height of the microstructures are at most 4% of the sphere radius as required in their study, which is the case for the experiments performed here.

By solving Eqs. (24) – (27) for the resistance functions in Eqs. (18) – (21), an apparent dimensionless gap width δ*/a is found as:

$$\frac{\delta^*}{a} = \left(\frac{\delta_s}{a}\right)^{\phi}\left(\frac{\delta_f}{a}\right)^{(1-\phi)}, \qquad (26)$$

which is interpreted as an effective separation between the sphere and the incline experienced by the rolling sphere. In the context of the model of Smart et al., the quantity δ*/a represents the equivalent asperity height for a given surface microstructure if the roughness elements were sparsely dispersed on the surface. Due to the logarithmic relation of the resistance functions with respect to the apparent gap, the resultant effective dimensionless gap height follows an exponential model in which δ* decreases rapidly as the solid fraction of the microstructures ϕ increases. To the best of our knowledge, this is the first attempt to relate the microstructure (via the solid fraction) to the apparent gap experienced by the rolling sphere. We note that the superposition of forces employed in this model is a rough approximation of hydrodynamic interactions. However, the limit where the fluid gap is smaller than the pore scale while keeping the hydrodynamic radius large compared to the pore size is a hard limit to fully model explicitly. Based on this analysis, the apparent dimensionless gap is only a function of the solid fraction and as such should be the same for microwells and micropillars structures. The bounds for Eq. (28) are the feature height δ_f in the dilute limit ($\phi \rightarrow 0$) and the inherent surface roughness at the top of the features for a flat surface (in the limit of $\phi \rightarrow 1$).

B.3. Materials and Methods

A. Ceramic Spheres

Silicon nitride (Si3N4) spheres with diameters of 3.00 mm and 5.00 mm and a density of 3.29 g/cm3 were used as received. The ceramic spheres (BC Precision) are grade 5 ball bearings with a reported maximum absolute roughness tolerance of 20 nm. The roughness of the particles measured under a profilometer (Dektak) did not exceed 5 nm. Two parallel lines of different lengths were painted on the spheres to track the angular orientation of the sphere (Figure 1(a)) during the motion in the experiments.

B. Fabrication of SU-8 Features

Flat and microstructured surfaces consist of layers of SU-8 on silicon wafers. The fabrication process follows standard photolithography protocol, and is briefly summarized here for clarity. To create a basecoat, the negative photoresist (SU-8 2007, MicroChem) is spin-coated onto a silicon wafer at 1700 rpm for 30 seconds with an acceleration of 500 rpm/s. The spin-coated silicon wafer is baked on a hot plate for 3 minutes at 95°C and followed by exposure at an energy of 140 mJ/cm2 without a photomask. The exposed wafer is baked again at 95°C for 3 minutes to create a smooth basecoat of SU-8. For the microstructured surfaces, an additional layer SU-8 is spin-coated on top of the basecoat under the same conditions and exposed through a chrome-on-glass photomask. The exposed wafer is then baked on a hot plate for 3 minutes at 95°C. Upon the post-exposure bake, the SU-8 coated wafers are immersed in SU-8 developer (MicroChem) for 3 minutes. Any residues of SU-8 were removed with excess developer and isopropyl-alcohol followed by drying with compressed air.

The fabricated features were characterized using an optical microscope and a confocal laser scanning microscope. Each of the fabricated microstructures is checked for a uniform thickness (i.e. pillar height or well depth) of 10 μm and for pattern fidelity. The inherent roughness of the SU-8 surfaces (flat and microstructured) is measured using a profilometer (Dektak). The arithmetic average of absolute roughness heights Ra did not exceed 5 nm for the smooth surface and the top of the structures of the textured surfaces.

Table B.1. Dimensions of the microtextured surfaces investigated (Figure 1). All features heights are $\delta_f = 10$ μm.

diameter d (μm)	spacing w (μm)	type	solid fraction ϕ
-	-	Flat	1
10.0	40	Pillars / Wells	0.04 / 0.96
10.0	10	Pillars / Wells	0.23 / 0.77

10.0	3.0	Pillars / Wells	0.54 / 0.46
19.5	6.5	Pillars / Wells	0.51 / 0.49
30.0	3.0	Pillars / Wells	0.75 / 0.25

C. Experimental Setup

The experimental setup consists of an acrylic tank with a cross section of 25 cm □ 12.5 cm at the base and a 25 cm height. The tank was filled with a Newtonian, water/glycerol solution consisting 90% glycerol and 10% water by weight. The kinematic viscosity and density at room temperature was calculated using the empirical exponential model developed by Cheng [48]. Based on this model the resultant mixture should have a kinematic viscosity of and a density of ρ_f = 1235 kg/m3 at 25°C. However, due to the hygroscopic nature of glycerol-water solutions, the viscosity of the mixture decreases over time. Therefore, the kinematic viscosity of the solution is also measured with an Ostwald viscometer before and after each set of experiments to ensure consistent viscosity, and to have the appropriate numerical values to use in the analysis. The measured viscosity varied between and among experiments did not change more than 3% within a three-hour experiment. A silicon wafer with fabricated microstructures was submerged and fixed flat on the center of the floor of the acrylic tank. The tank was then placed on a stand with an adjustable angle of inclination θ. Spheres were rolled down the planes at least 15 times on all surfaces prior to starting any data collection to remove any bubbles present in the interstices of the microstructures (which were sometime observed with the smaller microstructures) or until all visible air bubbles were removed.

For the measurements, an individual ceramic sphere is released on the wafer to roll down the surface. During each release, the spheres are oriented so that the two drawn parallel lines face the camera and that the markings do not touch the plane or microstructures. The motion of the rolling sphere is recorded by a video camera (Apple iPhone 6) at 60 fps for experiments with $\theta \leq 15$ degrees and at 240 fps for experiments with $\theta > 15$ degrees, the videos are then transferred to a computer where MATLAB is used to extract individual frames. We rely on ImageJ software to analyze the video files to determine the rotational and translational velocities of the spheres. The rotational velocity is calculated by measuring the number of frames required to complete a half or full rotation depending on the amount of slipping. The translational velocity is calculated by determining the location and the diameter of the sphere at 11 frames chosen at regular intervals within a half or full rotation, and averaging the velocity within the 10 intervals. According to the model developed by Jan et al. [49], and Jalaal et al. [50,51], the particle should reach terminal velocity practically instantaneously under these experimental conditions. The velocities at each interval are checked to confirm that terminal velocity is reached by the particle. Based on the translational velocity, the particle Reynolds number ranges from to for the 5.00 mm particle and from 1×10^{-3} to 5×10^{-2} for the 3.00 mm particle for inclination angles between 6 degrees and 30 degrees. While we analyze our results in the Stokes flow limit, we note that the Reynolds numbers of particles are small yet finite. For a given surface and inclination angle pair, two separate particles with the same diameter are rolled twice in an experiment. The experiment is replicated twice, resulting in eight replicated measurements for each condition. Note here that the measured rotational and translational velocities, although measured from the same video, are independent measurements.

B.4. Results and Discussion

A. Experimental results

The measured rotational and translational velocities for the 3.00 and 5.00 mm particles are shown in Figure 2. We scale the measured velocities with their respective Stokes velocities to make them dimensionless (see Eqs. (9) – (10)). The Stokes velocity for each data point is calculated using the average of the viscosities measured before and after each set of experiment. The data presented in Figure 2 is for all the surfaces microstructures detailed in Table 1, and the velocities are displayed as a function of inclination angle. The velocities for surfaces without microstructures (i.e. flat) is reproduced on each plot to highlight the contribution of the microstructure on the particle velocities. The error bars, which are in general smaller than the markers on data points, represent one standard deviation calculated from eight repeats.

The general features of the velocity curves shown in Figure 2 are very similar to the ones obtained by Smart et al. [35] At low inclination angles, the overall translating motion down the surfaces occurs via rotation of the spheres for all the surfaces investigated: the differences between the translational and rotational velocities are very small (less than 2%). Note here that the dimensionless rotational and translational velocities are independent sets of data. Then, as the inclination angle increases and reaches its critical value, slipping becomes more important and dominates the translating motion of the sphere down the plane. As a result, our experiments capture the branching out between the rotational and translational velocities at higher inclination angles. As the solid fraction of the features increases for both the micropillar and microwell surfaces (going from the top to the bottom within a column in Figure 2) we measure a systematic shift of the velocity curves towards the curves of the smooth surface. We also find that surfaces with lower solid fractions have higher dimensionless velocities when not slipping and a higher critical angle θ_c.

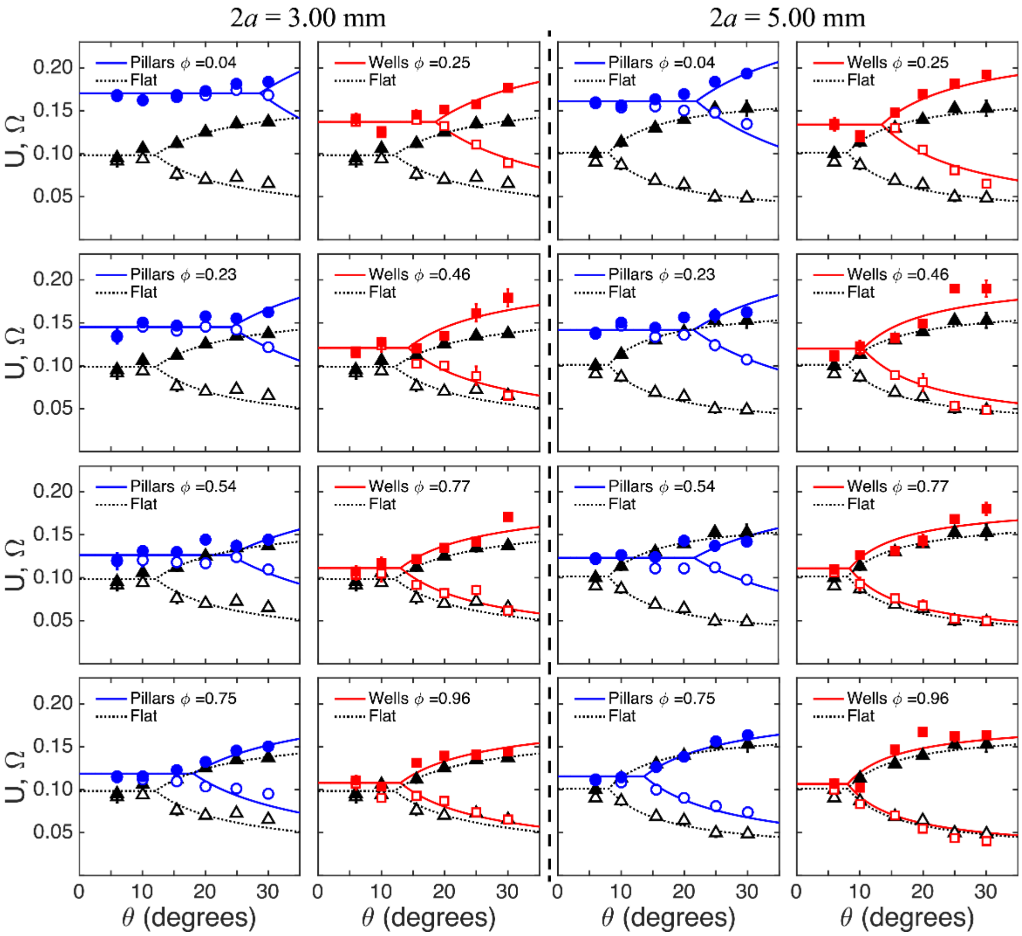

Figure B.2. Non-dimensionalized experimental results of the 3.00 mm particle (left) and 5.00 mm particle (right). The translational (U, filled markers) and rotational (Ω, open markers) velocities are plotted versus the angle of inclination, θ. The left column consists of particles rolled on micropillars (blue circles) with solid fractions ϕ = 0.04, 0.23, 0.54, 0.75 (blue, from top to bottom) and are compared to results from a flat surface (black triangles). On the right column, microwells (red squares) of ϕ = 0.25, 0.46, 0.77, 0.96 (red, from top to bottom) with the same flat results as the left column, shown for comparative purposes. Solid lines are drawn from Eqs. (13) – (15) using the fitted dimensionless gap and coefficient of friction of a least squares fit.

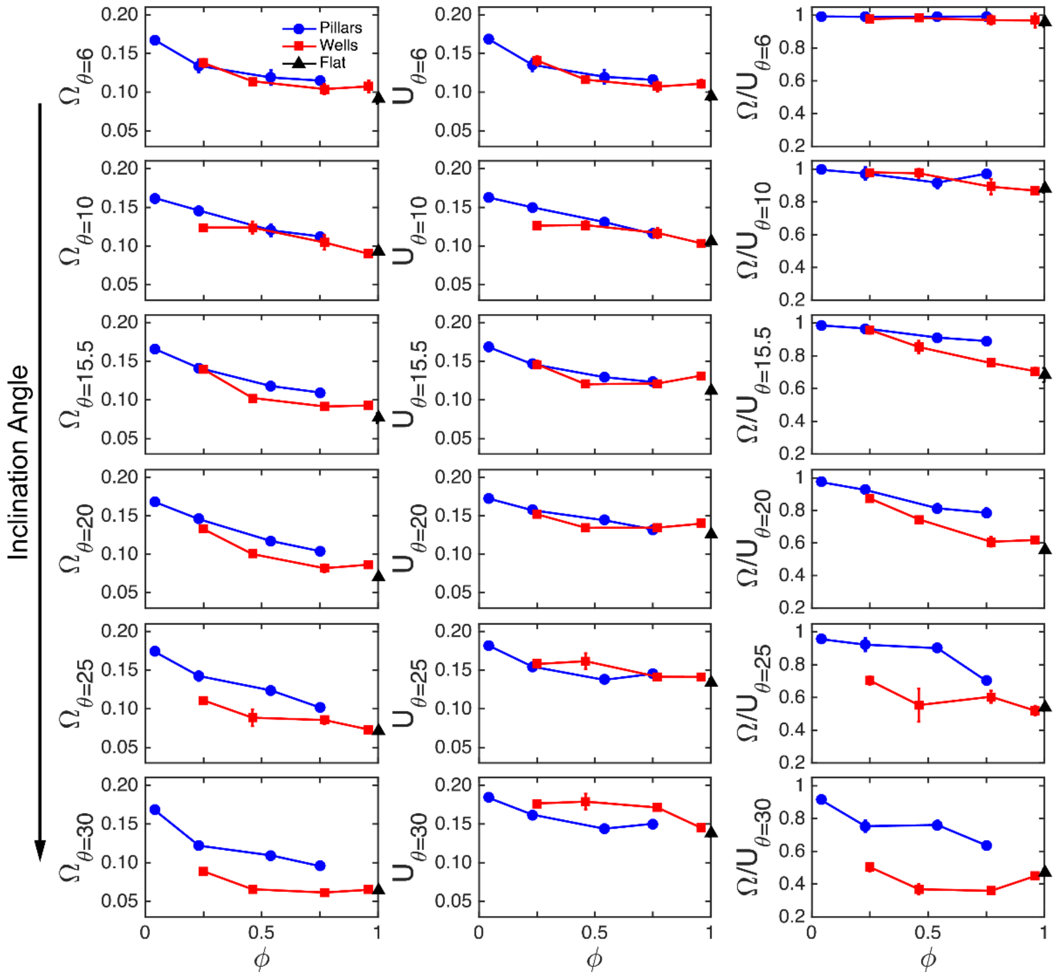

Figure B.3. Dimensionless rotational velocities Ω (left), translational velocity U (center), and fraction of rotation in net translational velocity Ω/U (right) of 5.00 mm sphere on pillars (blue circles), wells (red squares), and flat (black triangles) surfaces as a function of coverage obtained at different angle of inclinations (increasing from top to bottom). Error bars which are mostly smaller than the marker size represent standard deviations from 8 repeated measurements. Legend the same for all the panels.

The rotational velocities show a clear dependence on the surface coverage and distinct differences between the microwells and micropillars (left column in Figure 3). First, spheres rolling on micropillar surfaces have a larger rotational velocity than when they are rolling on microwells surfaces. This trend holds across the range of surface coverages investigated and for both particle sizes. The rotational velocity decreases as the coverage increases for both the micropillars and microwells surfaces, and for all inclination angles investigated (up to 30 degrees). For example, the dimensionless rotational velocity increases by 77% on the $\phi = 0.04$ micropillar surface compared to the flat surface for the 3.00 mm sphere. In contrast to the rotational velocity, the translational velocity, U, is largely unaffected by the type of surface structure (wells or pillars, see the middle column in Figure 3). Perhaps one exception is for the highest inclination angle ($\theta=30^o$) where the microwells definitely have a larger translational velocity across the whole range of surface coverage than the surface with micropillars.

The differences in the ratio of the rotational velocity to the translational velocity (U/Ω) for two type of surface structures investigated is striking as the inclination angle increases (see right column in Figure 3). We observe that the contribution of sphere rotation on the overall translational motion decreases drastically for the microwells surfaces as the inclination angle increases (going from the top to the bottom of the column). While the relative importance of rotational motion also decreases for the micropillar surfaces with increasing inclination angle, this trend is much less pronounced than for the motion on microwells surfaces. This is particularly interesting because the dominant mode of translation for spheres at low inclination angle is rotational motion, and under these conditions only small differences exist between the dimensionless rotational velocities of spheres on micropillar surfaces and on microwells surfaces. However, as the angle of inclination increases, the dominant mode of motion shifts to slipping, and under these conditions the difference between wells and pillars becomes much more evident. This transition suggests that the relative effect of microstructures on the motion of rolling spheres not only depends on the parameters that define the structures themselves, but also on the driving force (i.e. angle of inclination) acting on the spheres. Thus, in the case of spheres rolling due to shear driven flow or pressure driven flow, for example, the spheres may translate faster on micropillars for smaller shear velocities or pressure, whereas higher fluid velocities may allow spheres to translate faster on microwells.

The greatest difference in the Ω/U ratio between the two structure types (right column of Figure 3) is at surface coverages near $\phi = 0.50$. This outcome implies that the effect of geometry is most pronounced at $\phi \approx 0.50$. One possible explanation is that, as the coverage deviate from this value, the rolling motion approaches limits where the geometry of the asperities is less important. For instance, as the coverage decreases the microstructures may approach idealized asperities limit, where roughness elements merely support the sphere (i.e. the dilute limit predicted by Smart et al. [35]). At the high coverage limit, on the other hand, the interconnected channels between the micropillars may become too narrow, failing to favor boundary contact between the sphere and the plane, and becoming virtually indistinguishable from microwells.

B. Comparison with theory

The lines in Figure 2 correspond to a least-square fit of the two-parameter (δ and μf) model of Smart et al. [35] described in the theory section. We employ a grid-search method [52] to perform a nonlinear least squares fit to the experimental data. The parameter space surveyed consists of effective gap widths that span 0.01 nm to 150 □m and coefficients of friction ranging from 0.01 to 0.40. The grid is based on 2800 logarithmically spaced points for dimensionless gap widths ranging from 10^{-8} to 10^{-1}, which results in approximately 0.6% increments, and step sizes of 0.0025 are used for coefficient of friction. For each gap width and coefficient of friction pair, a theoretical velocity plot is calculated from Eqs. (13) – (15) using the resistance functions of Eqs. (18) – (21). Then the error in velocity is calculated for each inclination angle for which experimental data points are collected. The sum of the squares of errors was calculated for each gap width and coefficient of friction pair, and the pair of two parameters that yields the smallest square sum of errors is chosen as the fitting parameter for each particle size and microstructure combination. Figure 4 shows a sample error map of the square sum of errors for the 3.00 mm particle rolled on the flat surface calculated from the grid search method. The map shows the entire range of δ/a and μ_f scanned. It is clear from the error map that we obtain a single global minimum for a fitted dimensionless gap and coefficient of friction pair. A $\log_{10}$ of the sum of errors is plotted in Figure 4 due to the rapid increase of the errors as the two parameters deviate from the optimal value. We obtain a unique global minimum for the error that is qualitatively similar to the error map presented in Figure 4 for all the cases investigated. Figure 5 shows the numerically fitted parameters used in Figure 2 as a function of surface coverage. We treat the flat surface with a uniform layer of SU-8 as a surface having a solid fraction of $\phi = 1.00$. To determine the error bars in Figure 5, we propagate the mean standard deviation of the dimensionless velocities and calculate the apparent gap widths corresponding to a vertical shift above and below the original fitted velocity curves.

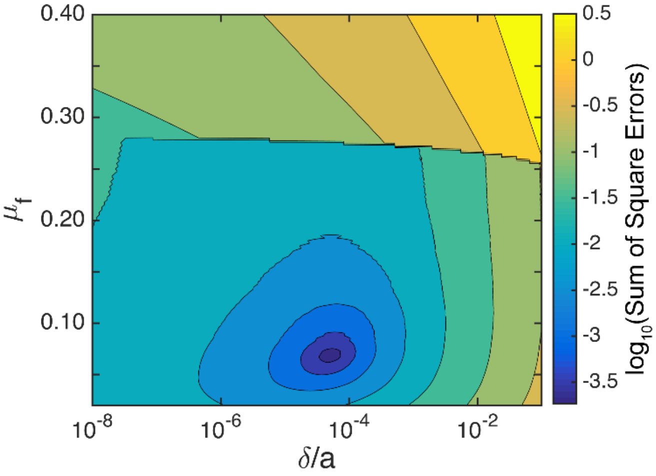

Figure B.4 Contour plot of $\log_{10}$ of the square sum of errors of the 3.00 mm particle rolling on the flat surface created using the grid search method. A single global minimum is obtained at $\mu_f = 0.0675$ and $\delta/a = 5.1 \times 10^{-5}$.

The model developed by Smart et al. describes very well the experimental data (Figure 2). The vertical shift of the velocity plot (or decrease in dimensionless velocity) as the solid fraction increases shown in Figure 2 leads to a smaller apparent gap (Figure 5(a)). Similarly, the decrease in the critical inclination angle (θ_c) with surface coverage shown in Figure 2 results in lower coefficients of friction experienced by the particles (Figure 5(b)).

It is interesting to point out that for $\phi = 0.04$ both the microwells and micropillars surfaces give values for the fitted apparent gap of approximately 10 μm, which is the physical height of the patterned features. The model of Smart et al. should relate the apparent gap to the true physical height of roughness elements only in the dilute limit, which is what we observe in our experiments. As the surface coverage increases and departs from the dilute limit, the effective gap decreases exponentially from the feature heights. The apparent gaps experienced on the flat surface are approximately 100 nm for particles of both sizes, which is somewhat larger than the average measured roughness Ra of the sphere and of the SU-8 surface. This discrepancy is consistent with the results by Prokunin, in which the motion of relatively smooth spheres with roughness heights less than 1 μm down an incline at low Reynolds numbers showed significantly larger separation (i.e. contactless motion) between the sphere and plane than the measured average roughness from profilometry [41]. The study states that the origin of this contactless motion is unclear, but suspects that the outcome may be a result of inertial forces or changes in physical properties of thin liquid films between the two solid surfaces under high disjoining pressure. As the Reynolds Numbers observed during our experiments reaches values up to at $\theta = 30^{\circ}$, small inertial effects may result in higher velocities and increased gap widths. The study by Galvin et al. further questions the notion of a single value of roughness and suggests that this outcome may be due to multiple scales of roughness, which results in a time-averaged hydrodynamic roughness that may be greater than the average roughness R_a [43]. Atomic force microscopy or electron microscopy could provide a more detailed characterization of the roughness for the flat surface. However, the reason for the apparent contactless motion, whether it is inertial effects or altered physical properties, is unclear and requires further investigation.

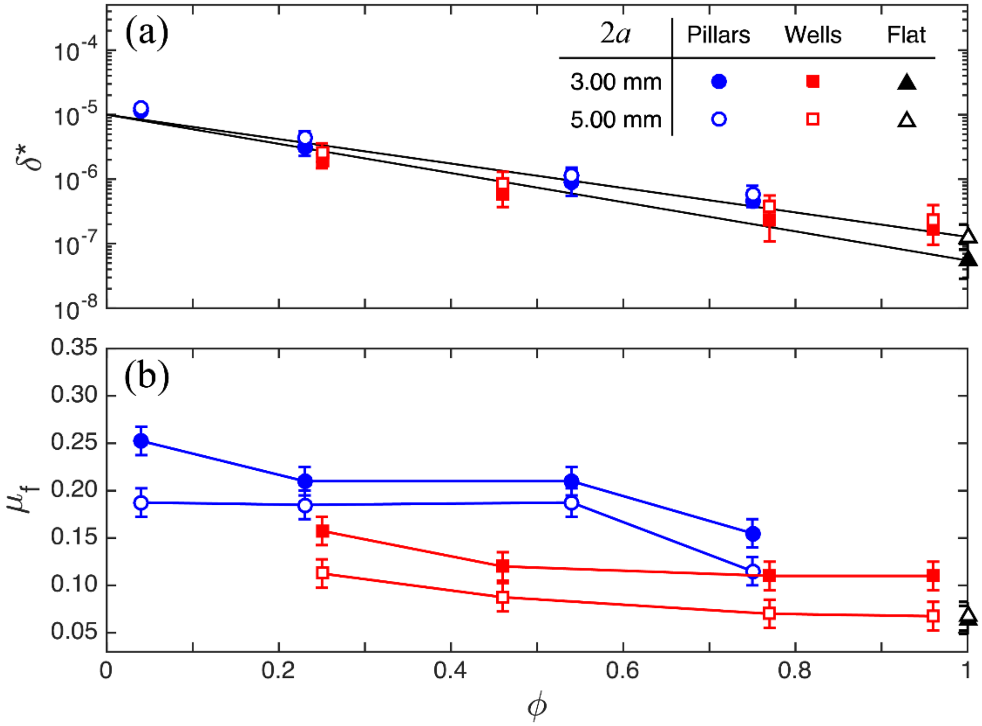

Figure B.5. (a) Apparent gap width δ* calculated by rolling spheres on pillars (blue circles), wells (red squares), and flat (black triangles) surfaces as a function of coverage. Error bars represent the propagated standard deviations from dimensionless velocities. The solid line represents Eq. (28). (b) The effective coefficients of friction μ_f of the rolling spheres. The error bars have a fixed magnitude of 0.02, which approximately translates to a critical angle of 2 degrees. This error value gives a conservative range for the critical inclination angle based on the variability of the dimensionless velocity plots shown in Figure 2. The solid lines serve as visual guides only.

To model the dependence of the effective gap width on the solid fraction shown in Figure 5(a) we implement a superposition approach inspired by the work of Staben et al. [46]. We treat the micropatterned surfaces as an ideal mixture of top and bottom surfaces, each of which with its own resistance functions (see Theoretical Development section). In this analysis, the fraction of top and bottom surface experienced by the sphere is determined by the solid fraction of a given microstructure surface, using Eqs. (22) – (23). The black solid lines in Figure 5(a) represent theoretical predictions of the apparent gap width from Eq. (28) with a feature height of 10 μm for δ_f and the fitted effective gap from the Smart et al. model for δ_s. The experimental results show good agreement with the surface coverage dependence predicted by the developed model. The data points at $\phi = 0.04$ in Figure 5(a) show that both the 3.00 mm and 5.00 mm particles respectively experience gap widths of 11.4 μm and 12.5 μm, which are roughly equal to the physical height (10 μm) of the microstructures. However, the apparent gap width rapidly decreases as the coverage of the roughness features increases, reaching an order of magnitude less at □ = 0.5 for both the micropillar and microwells structured surfaces, which is consistent with the prediction in Eq. (28). Note that the model predicting the effective gap width does not distinguish between different structures (micropillars and microwells). However, the data points in Figure 5(a) show greater δ^* for surfaces with micropillars than with microwells. For surface with similar coverages, the apparent gap width was about 75% to 100% greater on micropillar surfaces than on microwell surfaces. Because of the exponential relation between coverage and δ^*, the effect of coverage on the apparent gap is far more significant than the effect of different structures, and only small differences in velocities are seen between the two surfaces. While small, deviation between the model and the experiments are present, especially at high area fraction for the microwells surfaces. These deviations are likely due to the approximate nature of the model and maybe also in the variability of the fabrication process. Therefore, further studies focusing on whether the model holds for a variety of complex structures may provide a deeper understanding on how the structure influences the effective gap width and could enable the development of better resistance functions for microstructured surfaces. To the best of our knowledge, this is the first time where a relationship between surface coverage and effective gap width for a rolling sphere is established.

In contrast to the effective gap height, the fitted coefficient of friction depends more strongly on the type of surface features (microwells vs micropillars) and particle size than on the surface coverage (see Figure 5(b)). The fitted coefficients of friction varied between 0.068 and 0.253 across all the surfaces and for both particles investigated (see Figure 5b). This range agrees fairly well with coefficients of friction obtained from direct tribological measurements between Si3N4 spheres and various SU-8 microstructures [53]. This agreement suggests that our experimental method and analysis could be a gentle and effective way of measuring friction in fluid environments. The fact that the coefficient of friction varies slightly with the type of surface, particle size, and area fraction also suggests that hydrodynamics also plays a role in its value, similar to the change in the coefficient of friction for lubricated contacts found on Stribeck curves [54].

We find that rolling particles experience a greater coefficient of friction on micropillars surfaces than on microwells surfaces, and the flat SU-8 surface had the smallest coefficient of friction of all. This general trend is in agreement with a variety of frictional studies where surfaces patterned with micropillar showed increased friction forces in wet environments, compared to their flat counterparts. The study by Huang and Wang, for example, compared the tribological performance of various microstructured surfaces (cylindrical and hexagonal micropillars, cylindrical wells, and flat surfaces) under lubricated conditions [44]. They observe that the friction force increases when going from a flat surface, to microwells, and with pillars having the highest coefficient of friction. The authors suggest that a continuous lubricant film present during sliding on flat surfaces supports the weight of the sphere (hydrodynamic lubrication regime) and reduces friction. In our experiments, the fitted gap on the flat surface is indeed greater than the measured roughness, suggesting that spheres may also be experiencing the hydrodynamic lubrication regime without significant solid contact, resulting in a smaller coefficient of friction. Surfaces with micropillars, in contrast, would provide an additional path for fluid drainage through the pore space between the pillars, and fluid drainage could prevent the formation of a lubricant film between the sliding surfaces. The absence (or decrease in thickness) of the fluid film would then favor direct solid-solid contact, and thus increases the friction forces (mixed lubrication regime). Fluid drainage through surface channels could also explain the increase in friction forces observed by Varenberg et al. where they showed that surface structures with pillars designed to mimic the toe pads of bush crickets lead to an enhancement of friction under flooded conditions [55]. Interestingly, similar measurements by Drotlef [13] however, showed no dependence in the adhesion force on the fluid viscosity, as it would have been expected for a lubrication or mixed lubrication regime. In our previous work we investigated directly the role of surface channels on fluid drainage via normal hydrodynamic force measurements in the Surface Forces Apparatus [26,27].

We showed that the network of channel formed by the space between the pillars favored fluid drainage and contact formation. We also showed that in the thin channel geometry typical corrections for the no-slip boundary conditions could not fully explain the decrease in the viscous forces caused by the surface structures. In a related study we showed that the thickness of the fluid film separating flat surfaces determined if the work of separation during the peeling of a smooth surface from surfaces with micropillars was equal or less than that between two flat surfaces [56].

The fitted coefficients of friction decrease as the solid fraction increases, and at $\phi = 0.96$ the coefficient of friction of the microwells surface is approximately equal to the one of a flat surface (Figure 5(b)). As the spacing between each structural unit gets smaller, a higher fluid pressure is necessary for the fluid to drain via the channels present between individual surface features, which could shift the mode of lubrication from mixed mode to hydrodynamic and lead to a lower coefficient of friction. We anticipate that at the geometrical packing limit of $\phi = 0.907$, at which the spacing between pillars becomes zero, the interconnected channels between the structures of micropillars surfaces will no longer be present and the effective gap width and coefficient of friction should be very similar to those of microwells surfaces. We will test this hypothesis in future work. In the case of microwells, the fitted coefficient has a much weaker dependence on the surface coverage, with the greatest decrease in increasing surface coverage observed between $\phi = 0.25$ and $\phi = 0.50$. At low coverages, the well structures may be acting as asperities, thereby creating solid contact that increase the coefficient of friction, as described in the study by Saito and Yabu [57]. However, it is also possible that the difference measured between $\phi = 0.25$ and $\phi = 0.50$ is due to the difference in well diameter more than the change in coverage.

We also find that the coefficient of friction depends on the sphere radius (see Figure 5b). This is in contrast with the fitted values for the effective gap where we did not observe any meaningful difference caused by particle size (for the range of particle size investigated here). Across all the surfaces investigated, the smaller 3.00 mm sphere has a larger coefficient of friction than the 5.00 mm sphere, which is consistent with observation by Prokunin and Williams in which the coefficient of friction decreased with increase in the particle diameter [41]. Within our experiments, the two particles had a mean difference in coefficient of friction of 0.040 and standard deviation of the differences of 0.013. While the coefficient of friction in solid-solid contact should be constant, it is unclear why smaller spheres have a higher coefficient of friction despite having the same material properties. The increase in hydrodynamic radius for the larger spheres could lead to a thicker film, resulting in less solid-solid contact between the sphere and the microstructures and less friction. The effective gap data of Figure 5(a) supports this hypothesis. Particle-surface interactions, such as van der Waals forces, could also play a role, this aspect may be elucidated by further studies involving a wide range of sphere sizes and material properties.

The effect of the feature size (for a given surface coverage) is subtler than the effect of the other parameters investigated here (surface coverage, particle size, microstructure). In Figure 6 we show the fitted velocity curves of spheres rolling on two surfaces of the same geometry and similar coverages of $\phi \approx 0.50$. The solid lines correspond to the surface with microstructures of diameter d = 10 μm and spacing w = 3 μm whereas the dashed lines correspond to the velocity plots on surfaces with microstructures of diameter d = 19.5 μm and spacing w = 6.5 μm. The velocity plots are calculated from Eqs. (13) – (15) using the apparent gap width and coefficient of friction experienced by the 3.00 mm (top row) and

5.00 mm (bottom row) particles on rolling on the microstructured surfaces. The black dotted lines correspond to the fitted velocity plots of the particles on the flat surface showed here to aid comparison. As seen from Figure 6, there is a small (but consistent) effect of features sizes on the velocity plots caused by different values of both the apparent gap width and the coefficient of friction. For both the micropillars and microwells surfaces, the apparent gap width experienced by the particles and the velocities increases when the diameter and spacing approximately doubles, despite the negligible difference in surface coverage of the microstructures. For the micropillars surfaces, we observe a decrease in the fitted coefficient of friction as the diameter of the pillar doubles, and this effect is more visible for the 5.00 mm sphere. We do not find any significant difference in the coefficient of friction for the microwells when the diameter of the wells doubles. The reason for why no significant difference in the coefficient of friction is observed is not clear, but one possible reason may be the availability of large areas on the top of individual features that favor lubrication. As the size of the micropillars increases above a certain dimension, the structure may start to provide sufficient area for to act as a plane instead of a roughness element. Due to the limited set of data here, further study is necessary to understand better the effect of the feature size at a given surface coverage.

Table B.2. Fitted dimensional gap widths and coefficient of frictions for two surfaces of similar coverage for the curves shown in Figure 6.

Type	Solid Fraction ϕ	2a = 3.00 mm δ^* (μm)	 μ_f	2a = 5.00 mm δ^* (μm)	 μ_f
Flat	1	0.0548	0.103	0.128	0.068
Micropillars	0.54	0.893	0.210	1.15	0.188
	0.51	1.71	0.200	1.85	0.140
Microwells	0.46	0.570	0.120	0.872	0.088
	0.49	0.863	0.123	1.18	0.090

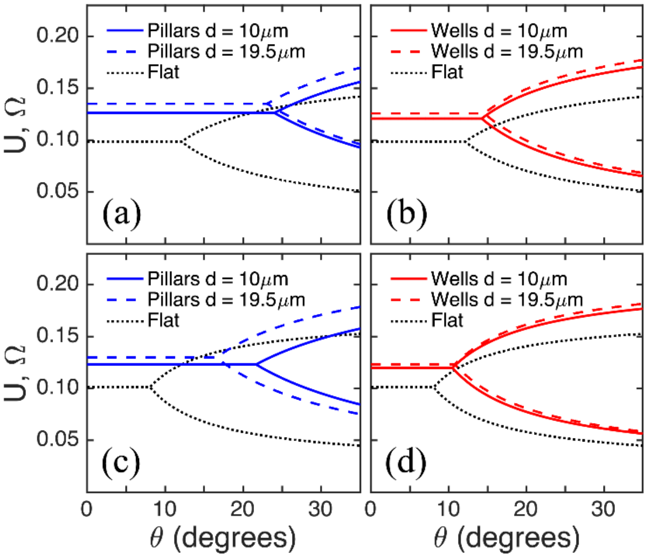

Figure B.6. Fitted dimensionless translational and rotational velocity curves created from fitted apparent gap widths and coefficients of friction for two surfaces of similar coverage but different dimensions for the 3.00 mm particle (top row) and the 5.00 mm particle (bottom row). The d = 10 μm micropillars have a solid fraction of ϕ = 0.54 and microwells have $\phi = 0.46$ whereas the d = 19.5 μm micropillars have $\phi = 0.51$ and microwells have $\phi = 0.49$. The values of the fitted parameters are given in Table 2.

B.5. Conclusions

In this study, we examined the rotational and translational velocities of spheres rolling down micropatterned surfaces of varying geometry and dimensions. The spheres rolled down silicon wafers patterned with either micropillars or microwells placed inside a tank of viscous glycerol-water mixture positioned on an adjustable incline. We captured the motion of the rolling spheres in a video and measured independently the rotational and translational velocities. The rolling motion was analyzed with the two-parameter contact force model developed by Smart et al. in which the motion is governed by the effective gap width between the particle and the plane, and the coefficient of friction between the two surfaces [35]. To account for the varying surface coverage of the patterned features we modified the asymptotic lubrication resistance functions of Goldman et al. to create a two-wall lubrication model, in which the respective resistance functions are linear combinations of the forces due to the plane located on the top and at the bottom of the microstructures.

The experimental results showed good quantitative agreement between the predicted and measured velocities. At low areal coverage ($\phi = 0.04$) of the roughness elements, the fitted gap height experienced by the particles matched the actual height of the microstructures. However, as the coverage increased, the apparent gap width quickly decreased, converging to the height experienced on a flat surface. Such apparent gaps experienced by particles showed a small dependence on structures. At a given coverage, the apparent gap on micropillars were slightly but consistently greater than the apparent gap on microwells. However, a significant difference in the coefficient of friction between the two types of surfaces was observed. Particles experienced a significantly higher friction on micropillars surfaces, especially at intermediate solid fractions ($\phi = 0.54$). This effect could be due to the presence of interconnected channels between pillar structures that allows the surrounding fluid to drain and let the two surfaces experience solid-solid contact. This study shows that characterizing the rolling motion of particles on microstructured surfaces can act as a gentle probe of the friction and lubrication properties of the surface. Such characterization can be useful to study the drag reduction and friction properties of bio-inspired microstructured surfaces, for microfluidic, biomedical, or robotic applications.

B.6. Acknowledgements

This work was partially supported by the Donors of the American Chemical Society Petroleum Research Fund under Grant 51803-ND5, and NSF-CMMI 1538003. BR acknowledges support from the Johns Hopkins University Provost Undergraduate Research Award (PURA).

REFERENCES

[1] R. H. Davis, Microhydrodynamics of particulate: Suspensions, Adv. Colloid Interface Sci. 43, 17 (1993).

[2] E. M. Hoek, S. Bhattacharjee, and M. Elimelech, Effect of membrane surface roughness on colloid-membrane DLVO interactions, Langmuir 19, 4836 (2003).

[3] B. Persson, O. Albohr, U. Tartaglino, A. Volokitin, and E. Tosatti, On the nature of surface roughness with application to contact mechanics, sealing, rubber friction and adhesion, J. Phys.: Condens. Matter 17, R1 (2004).

[4] B. Dean and B. Bhushan, Shark-skin surfaces for fluid-drag reduction in turbulent flow: a review, Phil. Trans. R. Soc. A 368, 4775 (2010).

[5] F. W. DelRio, M. P. de Boer, J. A. Knapp, E. D. Reedy, P. J. Clews, and M. L. Dunn, The role of van der Waals forces in adhesion of micromachined surfaces, Nat. Mater. 4, 629 (2005).

[6] L. Heepe and S. N. Gorb, Biologically inspired mushroom-shaped adhesive microstructures, Annu. Rev. Mater. Res. 44, 173 (2014).

[7] K. Liu and L. Jiang, Bio-inspired self-cleaning surfaces, Annu. Rev. Mater. Res. 42, 231 (2012).

[8] M. J. Hancock, K. Sekeroglu, and M. C. Demirel, Bioinspired directional surfaces for adhesion, wetting, and transport, Adv. Funct. Mater. 22, 2223 (2012).

[9] P. Ball, Engineering shark skin and other solutions, Nature 400, 507 (1999).

[10] C. M. Magin, S. P. Cooper, and A. B. Brennan, Non-toxic antifouling strategies, Mater. Today 13, 36 (2010).

[11] L. Wen, J. C. Weaver, and G. V. Lauder, Biomimetic shark skin: design, fabrication and hydrodynamic function, J. Exp. Biol. 217, 1656 (2014).

[12] W. Federle, W. Barnes, W. Baumgartner, P. Drechsler, and J. Smith, Wet but not slippery: boundary friction in tree frog adhesive toe pads, J. R. Soc. Interface 3, 689 (2006).

[13] D. M. Drotlef, L. Stepien, M. Kappl, W. J. P. Barnes, H. J. Butt, and A. del Campo, Insights into the adhesive mechanisms of tree frogs using artificial mimics, Adv. Funct. Mater. 23, 1137 (2013).

[14] J. Iturri, L. Xue, M. Kappl, L. García-Fernández, W. J. P. Barnes, H. J. Butt, and A. del Campo, Torrent Frog-Inspired Adhesives: Attachment to Flooded Surfaces, Adv. Funct. Mater. 25, 1499 (2015).

[15] D. M. Drotlef, E. Appel, H. Peisker, K. Dening, A. del Campo, S. N. Gorb, and W. J. P. Barnes, Morphological studies of the toe pads of the rock frog, Staurois parvus (family: Ranidae) and their relevance to the development of new biomimetically inspired reversible adhesives, Interface focus 5, 20140036 (2015).

[16] B. Persson, Wet adhesion with application to tree frog adhesive toe pads and tires, J. Phys.: Condens. Matter 19, 376110 (2007).

[17] B. Bhushan, Biomimetics: lessons from nature–an overview, Philos. Trans. R. Soc. London, Ser. A 367, 1445 (2009).

[18] M. R. Cutkosky and S. Kim, Design and fabrication of multi-material structures for bioinspired robots, Philos. Trans. R. Soc. London, Ser. A 367, 1799 (2009).

[19] S. Gorb, M. Varenberg, A. Peressadko, and J. Tuma, Biomimetic mushroom-shaped fibrillar adhesive microstructure, J. R. Soc. Interface 4, 271 (2007).

[20] T. P. Forbes and J. G. Kralj, Engineering and analysis of surface interactions in a microfluidic herringbone micromixer, Lab on a Chip 12, 2634 (2012).

[21] S. Nagrath et al., Isolation of rare circulating tumour cells in cancer patients by microchip technology, Nature 450, 1235 (2007).

[22] E. Bonaccurso, H.-J. Butt, and V. S. Craig, Surface roughness and hydrodynamic boundary slip of a Newtonian fluid in a completely wetting system, Phys. Rev. Lett. 90, 144501 (2003).

[23] V. S. Craig, C. Neto, and D. R. Williams, Shear-dependent boundary slip in an aqueous Newtonian liquid, Phys. Rev. Lett. 87, 054504 (2001).

[24] D. Y. Chan and R. Horn, The drainage of thin liquid films between solid surfaces, J. Chem. Phys. 83, 5311 (1985).

[25] A. Steinberger, C. Cottin-Bizonne, P. Kleimann, and E. Charlaix, High friction on a bubble mattress, Nat. Mater. 6, 665 (2007).

[26] G. A. Pilkington, R. Gupta, and J. Fréchette, Scaling Hydrodynamic Boundary Conditions of Microstructured Surfaces in the Thin Channel Limit, Langmuir 32, 2360 (2016).

[27] R. Gupta and J. Frechette, Measurement and scaling of hydrodynamic interactions in the presence of draining channels, Langmuir 28, 14703 (2012).

[28] T. V. Nizkaya, A. L. Dubov, A. Mourran, and O. I. Vinogradova, Probing effective slippage on superhydrophobic stripes by atomic force microscopy, Soft Matter 12, 6910 (2016).

[29] C. Kunert, J. Harting, and O. I. Vinogradova, Random-roughness hydrodynamic boundary conditions, Phys. Rev. Lett. 105, 016001 (2010).

[30] N. Lecoq, R. Anthore, B. Cichocki, P. Szymczak, and F. Feuillebois, Drag force on a sphere moving towards a corrugated wall, J. Fluid Mech. 513, 247 (2004).

[31] A. Mongruel, T. Chastel, E. S. Asmolov, and O. I. Vinogradova, Effective hydrodynamic boundary conditions for microtextured surfaces, Phys. Rev. E 87, 011002 (2013).

[32] O. I. Vinogradova and G. E. Yakubov, Surface roughness and hydrodynamic boundary conditions, Phys. Rev. E 73, 045302 (2006).

[33] O. I. Vinogradova and A. V. Belyaev, Wetting, roughness and flow boundary conditions, J. Phys.: Condens. Matter 23, 184104 (2011).

[34] T. Chastel and A. Mongruel, Squeeze flow between a sphere and a textured wall, Phys. Fluids 28, 023301 (2016).

[35] J. R. Smart, S. Beimfohr, and D. T. Leighton Jr, Measurement of the translational and rotational velocities of a noncolloidal sphere rolling down a smooth inclined plane at low Reynolds number, Phys. Fluids A 5, 13 (1993).

[36] Y. Zhao, K. P. Galvin, and R. H. Davis, Motion of a sphere down a rough plane in a viscous fluid, Int. J. Multiphase Flow 28, 1787 (2002).

[37] G. P. Krishnan and D. T. Leighton Jr, Inertial lift on a moving sphere in contact with a plane wall in a shear flow, Phys. Fluids 7, 2538 (1995).

[38] J. R. Smart and D. T. Leighton Jr, Measurement of the hydrodynamic surface roughness of noncolloidal spheres, Phys. Fluids A 1, 52 (1989).

[39] A. J. Goldman, R. G. Cox, and H. Brenner, Slow viscous motion of a sphere parallel to a plane wall—I Motion through a quiescent fluid, Chem. Eng. Sci. 22, 637 (1967).

[40] A. Goldman, R. Cox, and H. Brenner, Slow viscous motion of a sphere parallel to a plane wall—II Couette flow, Chem. Eng. Sci. 22, 653 (1967).

[41] A. Prokunin and M. Williams, Spherical particle sedimentation along an inclined plane at high Reynolds numbers, Fluid Dyn. 31, 567 (1996).

[42] A. Prokunin, Spherical particle sedimentation along an inclined plane at small Reynolds numbers, Fluid Dyn. 33, 573 (1998).

[43] K. Galvin, Y. Zhao, and R. Davis, Time-averaged hydrodynamic roughness of a noncolloidal sphere in low Reynolds number motion down an inclined plane, Phys. Fluids 13, 3108 (2001).

[44] W. Huang and X. Wang, Biomimetic design of elastomer surface pattern for friction control under wet conditions, Bioinspir. Biomim. 8, 046001 (2013).

[45] C. Pozrikidis, Boundary integral and singularity methods for linearized viscous flow (Cambridge University Press, 1992).

[46] M. E. Staben, K. P. Galvin, and R. H. Davis, Low-Reynolds-number motion of a heavy sphere between two parallel plane walls, Chem. Eng. Sci. 61, 1932 (2006).

[47] M. E. Staben, A. Z. Zinchenko, and R. H. Davis, Motion of a particle between two parallel plane walls in low-Reynolds-number Poiseuille flow, Phys. Fluids 15, 1711 (2003).

[48] N.-S. Cheng, Formula for the viscosity of a glycerol-water mixture, Ind. Eng. Chem. Res. 47, 3285 (2008).

[49] C.-D. Jan and J.-C. Chen, Movements of a sphere rolling down an inclined plane, J. Hydraul. Res. 35, 689 (1997).

[50] M. Jalaal and D. Ganji, An analytical study on motion of a sphere rolling down an inclined plane submerged in a Newtonian fluid, Powder Technol. 198, 82 (2010).

[51] M. Jalaal and D. Ganji, On unsteady rolling motion of spheres in inclined tubes filled with incompressible Newtonian fluids, Adv. Powder Technol. 22, 58 (2011).

[52] C. Ritz and J. C. Streibig, Nonlinear regression with R (Springer Science & Business Media, 2008).

[53] N. B. Tay, M. Minn, and S. K. Sinha, Polymer jet printing of SU-8 micro-dot patterns on Si surface: optimization of tribological properties, Tribol. Lett. 42, 215 (2011).

[54] B. Persson, Sliding friction: physical principles and applications (Springer Science & Business Media, 2013).

[55] M. Varenberg and S. N. Gorb, Hexagonal surface micropattern for dry and wet friction, Adv. Mater. 21, 483 (2009).

[56] C. Dhong and J. Fréchette, Coupled effects of applied load and surface structure on the viscous forces during peeling, Soft matter 11, 1901 (2015).

[57] Y. Saito and H. Yabu, Bio-Inspired Low Frictional Surfaces Having Micro-Dimple Arrays Prepared with Honeycomb Patterned Porous Films as Wet Etching Masks, Langmuir 31, 959 (2015).

Elastic deformation during dynamic force measurements in viscous fluids

Yumo Wang†1, Georgia Pilkington†1, Charles Dhong1, and Joelle Frechette*,1,2

1Chemical and Biomolecular Engineering Department and 2Hopkins Extreme Materials Institute, Johns Hopkins University, Baltimore MD 21218

* Corresponding Author, jfrechette@jhu.edu

† Equal contribution

C.1 Introduction

Viscous forces caused by the relative movement of two surfaces in a viscous fluid can exert local pressures that can be sufficiently large to cause elastic deformation of the interacting materials (see Figure 1). This scenario is very common in the tribology of lubricated contacts, where deformation due to viscous forces in oils is a key mechanisms to reduce friction and prevent wear (i.e. elastohydrodynamic lubrication or EHL, see Figure 1a).[1] Similarly, the presence of an elastic boundary during the drainage or infusion of fluid in a confined gap can lead to elastohydrodynamic deformation (EHD, see Figure 1b).

Both EHD and EHL play an important role in soft matter where materials such as gels, biological tissues, or elastomers (Young's modulusE~10kPa-100MPa) can deform during motion in a fluid at relatively low velocities and viscosities.[2-5] For example, elastic deformation will affect the collision and rheological response of soft colloidal particles

(Figure 1c (i) and (ii)), coalescence of bubbles/drops (Figure 1c (iii)), and has been hypothesized as a mechanism for shear thickening behavior.[6]. Studying the dynamic adhesion of cells or capsules attached to a wall is also accompanied by deformation, and the stored elastic energy greatly alters the detachment process (Figure 1d).[7] Similarly, insects and several vertebrates are also known to mediate contact between their soft toe pads and surfaces through liquid layers[8], therefore understanding their locomotion and detachment requires understanding how the toe pads and highly confined liquid layers interact. Finally, in joint cartilage, a lubricating layer of fluid and the squeeze out from a polymer network (weeping lubrication) is suspected to be responsible for the low apparent friction across joints.[9,10]

These deformations, in turn, can have a profound effect on the hydrodynamic interactions [11], such as those encountered during dynamic force measurements with the atomic force microscope (AFM)[12,13] or the surface forces apparatus (SFA) (see Figure 1b).[14,15] The SFA and AFM are well-suited to study the coupling between soft matter and hydrodynamic interactions, as demonstrated with droplets or bubbles[16-21](Figure 1c(iii)). More recently, these tools have been employed and adapted to study elastohydrodynamic deformation of compliant solids.[13-15] It is also important to consider the possibility of elastic deformation in the interpretation of surface forces measurements when one (or both) of the interacting surfaces has some degree of compliance (or reversely to know when to confidently ignore it). Neglecting to account for elastic deformation could lead to misinterpretation of the conservative surface forces (such as van der Waals or electrostatic) or slip behavior.

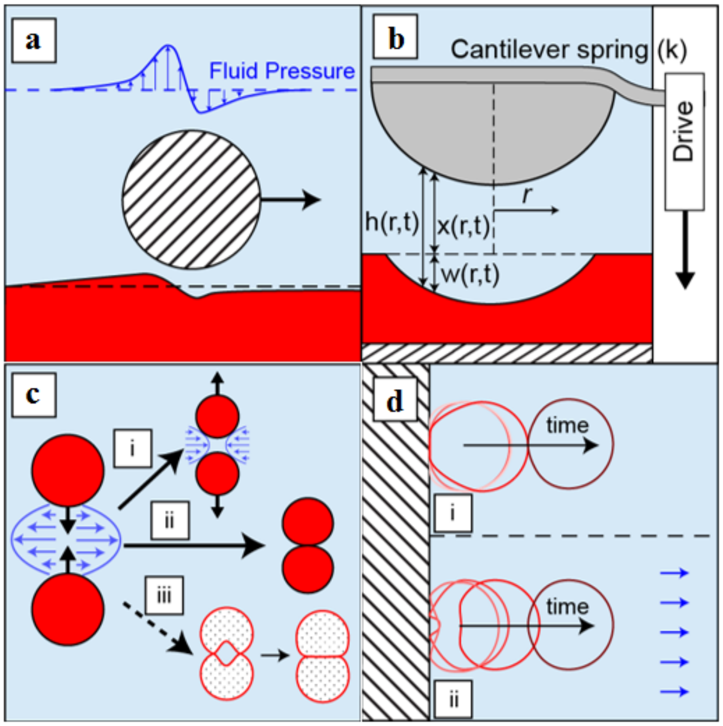

Figure C.1. Hydrodynamic interactions in the presence of deformable materials. (a) Elastohydrodynamic lubrication: lift generated due to the sliding of a rigid cylinder along a soft material. (b) Elastohydrodynamic force measurement in the sphere-wall configuration with labeled variables. (Not to scale) (c) Rheological behavior of particles, bubbles, or drops colliding followed by either (i) rebound or (ii) sticking, or (iii) dimpling and then coalescence for bubbles/drops. (d) Adhesion and detachment of a soft or liquid-filled capsule, or cell, where the morphology and dynamics of detachment changes in the presence of quiescent (i) or external (axisymmetric) flow (ii). (d) is adapted from [22] with permission.

Due to its broad practical significance, a better understanding of the impact of deformation on hydrodynamic interactions and surface forces is necessary. Here we review studies, which in general have considered the classic geometry of a sphere approaching a plate at a constant drive velocity in a viscous fluid within the lubrication limit, and where one of the surfaces is supported by a force measuring spring (see Figure 1b). These are the experimental conditions encountered in typical surface forces measurements. This review is organized as follows: first we describe the theoretical framework and present experimental validations, focusing on direct force measurements. We then discuss current scientific challenges in describing or characterizing hydrodynamic interactions in the presence of elastic deformation. Finally, we provide broad guidelines to researchers working on surface forces measurements that highlight experimental conditions where elastic deformation might be present in dynamic force measurements with the AFM or SFA. Important and related topics not covered here include bouncing and rebounding of spheres[6](Fig.1c), jamming of deformable spheres[23], elastohydrodynamic lubrication (EHL), and rheological implications[24].

C.2 Physical Description

While there are many configurations where elastohydrodynamic deformation might be important (see Figure 1), the most common alignment encountered surface force measurements is the sphere-plane geometry. This configuration facilitates experimentation and analysis due to axisymmetry and by ensuring point contact. (Figure 1b). A geometrically equivalent configuration would be that of two nearby cross-cylinders which is used in the SFA.[25] The description of the elastohydrodynamic problem needs to address the coupling between fluid dynamics and surface deformations. The lubrication approximation with the no-slip boundary condition (Equation 1) describes drainage and infusion of liquid from a thin gap in the limit where the surface separation is much smaller than the radial length scale:

$$\frac{\partial h}{\partial t} = \frac{1}{12\mu r}\frac{\partial}{\partial r}\left(rh^3\frac{\partial p}{\partial r}\right), \qquad [1]$$

where h is surface separation, t is time, μ is the viscosity for a Newtonian fluid and p is fluid pressure. [26,27] In the absence of elastic deformation the fluid pressure distribution is readily obtained from Eq. 1 for a given initial condition, h(r,0). The pressure can then be integrated radially to determine the total hydrodynamic force.

Surface deformation alters the fluid film thickness profile and shape of the interacting surfaces. This change in local fluid film thickness modifies the fluid pressure which, in turn, determines the deformation profile. The deformation profile, w(r,t), can be obtained from linear elasticity for a spherical half-space, and is given by Equation 2:

$$w(r,t) = 4\theta \int_0^\infty f(y,t)\frac{y}{y+r}K\left[\frac{4ry}{(r+y)^2}\right]dy, \qquad [2]$$

where θ=(1-v^2)/πE, v is Poisson's ratio, E is Young's modulus, f is surface stress distribution, y is a dummy variable used in integration, and K is the complete elliptic integral of the first kind. In Eq. 2 the surface stress distribution comes from the fluid pressure, and due to the solid-fluid coupling, the lubrication equation needs to be solved simultaneously with the deformation profile. Usually a numerical solution is necessary, but analytical solutions can be obtained by making some approximations. For instance, Davis et al. [28] demonstrated that in the limit of small deformation (w/x<0.05 in Figure 1b) a closed-form solution can be obtained by using the undeformed surface separation in the lubrication equation. This solution has served as a useful means of examining whether notable deformation is present in drainage flow.[25] A simple algorithm proposed for modeling half-space in the case of significant deformation is to treat the deformation as a non-adhesive contact (Hertz theory[29]), and to replace the contact pressure distribution with the fluid pressure obtained for a given gap thickness by the lubrication equation. [30]

A more general consideration than assuming a half-space is necessary to treat the case of hard surfaces with compliant coatings or more generally for layered materials. In this case, the deformation can be acquired by applying a sticky boundary condition on the rigid substrate, using fluid pressure as a surface condition, and then solve for linear elasticity theory.[31] This approach allows for the role of the coating thickness to be investigated directly. For instance, Leroy and Charlaix used this approach to characterize regimes where fluid viscosity or the elasticity of the soft materials dominates the force response when confined by an oscillating rigid indenter (see Figure 2a).[3] Using this method they demonstrated that the absolute modulus of soft coatings could be measured out of contact, and without measuring the contributions of the underlying substrate.

During surface forces measurements one surface is typically mounted on a spring (or cantilever). In this case, the surface separation is different from the displacement of the driving motor due to the deflection of the spring. The different contributions to the total force, FT, from the hydrodynamic and conservative forces (F_s, e.g. van der Waals force, double layer force) can be considered independently[16] and this force balance for the sphere-wall geometry is given by Eq. 3:

$$F_T = kS(t) = \int_0^R 2\pi r p(r) dr + F_s, \qquad [3]$$

where R is the radius of spherical particle, and S(t) is the deflection of the cantilever with a spring constant k as a function of time.

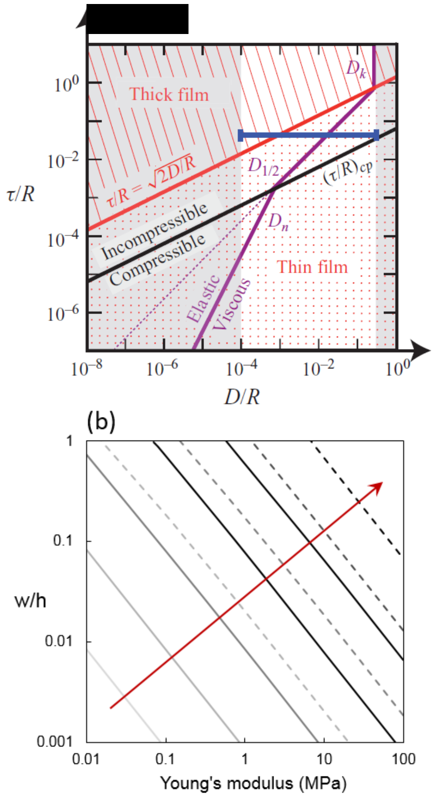

Figure C.2. (a) Dynamic phase diagram for an elastic film of thickness τ with a Poisson's ratio v =0.499. D is the surface separation, R represents the sphere radius. The continuous red line is the thick/thin film transition and the parallel black line is the compressible–incompressible transition, where the incompressible thin film domain lies between those lines. The purple lines are the elastic/viscous cross-over distances. The horizontal blue line is an example of experimental space which crosses several transitions. Figure is reprinted from [3] with permission (b) Calculated deformation (normalized by the fluid film thickness) predicted for normal continuous approaches in typical AFM and SFA experiments in water (viscosity 0.001 Pa·s). The deformation at the centerpoint (w) is calculated at a central fluid film thickness 20nm, well within the range of most conservative surface forces. Solid lines: typical AFM experiments with radius 5 μm, spring constant k= 1 N/m, and approaching velocity v at 0.1, 1, 10, 100, 1000 μm/s. Dashed lines: typical SFA experiments with R = 2 cm, spring constant 100 N/m, motor velocities v at 0.1, 1, 10, 100 nm/s. Red arrow and change in color gradient indicate the increasing of motor velocity.

For rigid surfaces in simple geometries (e.g. sphere-plane, crossed cylinders) the Derjaguin approximation can be used to extract the surface potential E(h) from surface force Fs = 2πRE(h). In addition, the hydrodynamic contribution to the total force can be further simplified to the Taylor equation.[25] However, for deformable surfaces, the surface geometry as well as the absolute surface separation, can vary due to fluid pressure. Thus, the knowledge of the surface profile as a function of time is required to decouple the hydrodynamic and surface forces. To do so, one needs to estimate how much deformation is present in the separation range where surface forces are measured. As an example, we present here deformation maps (see Figure 2b) by solving Eqns 1-3 for a continuous approach in the absence of surface forces (Fs = 0). In Figure 2b the relative deformation at the center point (w/h) is plotted for a range of Young's modulus (half-space) for experimental conditions that are typical of AFM (R = 5µm, k = 1 N/m) or SFA (R = 2cm, k = 100N/m) during dynamic experiments in water for a central separation h = 20 nm. As seen in Figure 2b, significant deformation (of order of the fluid film thickness) can be achieved under many realistic experimental conditions involving compliant materials. Based on the deformation plotted in Figure 2b, for an AFM experiment with drive velocity of v = 1 mm/s, we calculate the increase in hydrodynamic force at h = 20 nm due to the deformation of a material of E = 1MPa to be 17%. Similarly, for a SFA experiment at a drive velocity of v = 100 nm/s which is fairly fast consider its larger radius, this increase is in force is 10%, even for E = 5MPa material. In addition, deformation brings uncertainties in the determination of the contact position during dynamic AFM measurements. Furthermore, possible additional deformation due to shear near contact, which we did not include in the map of Figure 2b, would amplify further the change in fluid film profile.

C.3. Experimental validation

A limited number of drainage studies have investigated hydrodynamic forces where one or both of the interacting surfaces are able to deform. In general, these have been performed using atomic force microscopy (AFM) and the surface forces apparatus (SFA).[3,13,14,18-20,32,33] However, due to the difficulty in measuring both the deformation of the surface and the hydrodynamic forces, most studies fit direct force measurements data with theoretical approximations for the spatiotemporal deformed surface geometry. Recently, Kaveh et al. measured the hydrodynamic forces between a colloidal sphere and a soft, elastic polydimethylsiloxane (PDMS) surface using an AFM.[13] To approximate the deformation they used a numerical model to describe the normal hydrodynamic stresses acting on the liquid-solid interface. They showed that upon approach the deformation of the elastic layer leads to a reduction in the hydrodynamic forces due to an increase in the surface separation, facilitating additional drainage out of the gap. Whilst upon retraction, an upward deformation of the elastic layer was found to conversely retard the widening of the gap.

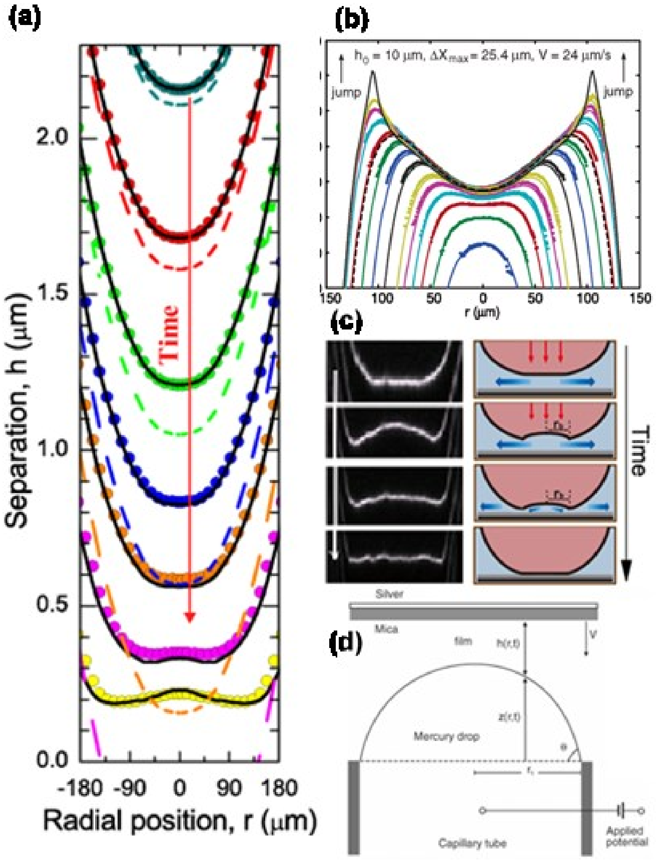

Figure C.3. Predicted and measured spatiotemporal evolution of the fluid film thickness for (a) an equivalent PDMS elastic sphere approaching a rigid wall in a viscous oil and (b) a mercury droplet with an applied positive potential approaching a negatively charged mica surface in an aqueous electrolyte. In both (a) and (b), the data points represent experimental results and the solid lines are theoretical predictions. In (a) the dashed lines correspond to the theoretical undeformed surface profiles. Schematic diagrams of the experimental configurations used to obtain results in (a) and (b) are shown in (c) and (d), respectively.

Figure (a),(c) are reprinted from [14], and (b),(d) are from [17] with permissions.

One possible difficulty in interpreting force measurements is that different contact geometries could potentially result in the same force. Therefore, direct measurements of surface deformation as a function of absolute separation are particularly helpful to understand the role of elastohydrodynamics on dimpling and conservative surface forces. Recently, we demonstrated that the deformation of an elastic surface approaching a rigid surface in a viscous fluid can be directly monitored as a function of absolute separation in a SFA (Figure 3a,c).[14] We showed that the deformation profiles were better described as a viscoelastic solid using the Kelvin-Voigt model than by treating the film simply as an elastic solid. By performing measurements for different PDMS film thicknesses, we also showed that for a thick film EHD leads to the formation of a dimple, preventing the interacting surfaces to make full contact, while for a thinner film contact could be made. This difference in the contact mechanics for the thin film was attributed to the stresses in the film being supported by the underlying substrate. In addition, we found that, despite having the same bulk mechanical properties, the effective modulus of a deformable layered system obtained by static force measurements cannot be applied in the analysis of dynamic interactions.

To avoid contributions from an underlying substrate when trying the measure the properties of elastic thin films, Charlaix and coworkers developed a nanorheological method which monitors the small amplitude oscillation of a sphere close to an elastic surface.[3] Based on the interplay of the liquid viscosity and solid elasticity, they showed that the viscous and elastic contributions to the damping force can be derived from a continuous elastohydrodynamic model (Figure 2a). By applying this technique and analysis, they demonstrated that the surface elastic properties of thin films can be characterized at nanoscale separations without mechanical contact, therefore eliminating the effects of adhesion and preventing surface contamination. In a related study, this technique has also been demonstrated to be a powerful method for studying the surface elasticity and interfacial properties of bubbles or air pockets trapped in hydrophobic structures.[33]

A number of similarities can be drawn between the elastohydrodynamic interactions between soft, solid interfaces and those of gas bubbles or liquid droplets (which have been investigated in more details). For example, Horn and coworkers developed a modified version of the SFA to measure the surface and hydrodynamic forces between a mercury drop and flat solid surface.[34] By analyzing the local curvature of the mercury/aqueous interface and relating it to the pressure drop across the interface via the Young-Laplace equation, they showed that the total film pressure does not vary greatly during the formation of a dimple or the thin film drainage process for different magnitudes and signs of disjoining pressures.[35] Instead, for different electrical potentials between the mercury drop and the aqueous phase, the hydrodynamic pressure was found to adjust to balance the disjoining pressure so that the total film pressure is approximately constant.

More complex flow phenomena and deformation profiles, such as dimples, wimples, pimples and ripples, have also been observed between drops or a drop and a sold surface. These complex geometries have been shown to be similarly well-described by combining the Stokes-Reynolds and Young-Laplace equations.[16,18] Using this analysis it was demonstrated that a repulsive hydrodynamic force leads to the formation of a dimple prior to contact, whereas an attractive double layer force causes a collapse or "jump in" at the dimple barrier rim (Figure 3b,d), where the surface forces are expected to be largest.[17] On the contrary, some repulsive surface forces, such as van der Waals forces, have been shown to further prevent the surfaces from collapsing or coalescing in order to maintain a minimum fluid thickness between them.[21] In a number of related studies, Chan and coworkers have developed a full numerical theory based on this analysis to describe the dynamic interactions of drops and bubbles measured using AFM (Fig. 3b).[16] In doing so, they have defined key parameters to describe the deformation behavior of drops as function of separation.[20] However, although there are many similarities which can be drawn between the dynamic interactions of drops and bubbles with those of soft solids, for drops and bubbles surface tension plays a key role in determining their shape and deformation. In contrast, for soft solids surface tension is expected to be less pronounced, therefore their deformation mechanisms are different. Though it should be noted that elastocapillary effects[36] could also play a role in the case of solid-solid interactions.

In absence of a moving spring which limits the surface movement, many experiments involving the bouncing of a sphere have been conducted to validate the EHD theory. These studies are important in the context of collisions,[28,37,38] as well as in hydrodynamic detachment for applications such as filtration, surface cleaning, and biological adhesion[22] Additional studies investigated the surface interactions and contact behaviors of viscous and viscoelastic thin films. For example, Zeng et al. combined in situ microscopy with interferometry in an SFA to measure the separation, film thickness, refractive index and contact geometry of adhesive contacts of viscous liquids and viscoelastic thin films.[39] They showed that the rate of growth of contact area could be well-predicted by a power law for adhesive contact and sintering of two Maxwell viscoelastic spheres. The viscoelastic behavior of confined viscous liquids has also been studied by Villey et al.[24] Their results showed that when confined to nanometer scales, the rheological properties of liquids cannot be decoupled from the global system response.

The confinement of pressurized synovial fluid has been hypothesized to contribute to the lubricating mechanism in mammalian joints by preventing direct contact and therefore avoiding wear-induced failure.[40] Analogous to this behavior, Espinosa-Marzal et al. showed that the confinement-induced pressurization of highly viscous lubricants can lead to the enhancement of the effective elastic modulus of polymer brush surfaces and shield polymer brush layers from the effects of the load.[9] In a related study, Charrault et al. studied via AFM measurements the effects of EHD on polymer brushes, and their effects on the hydrodynamic drainage forces.[41] By shifting the force curves by the length of the unperturbed polymer brush they showed that the hydrodynamic forces of a thick polymer brush layer could be described with a boundary slip model at low velocities (Figure 4). However, at high velocity the hydrodynamic forces were found to deviate from their analysis.

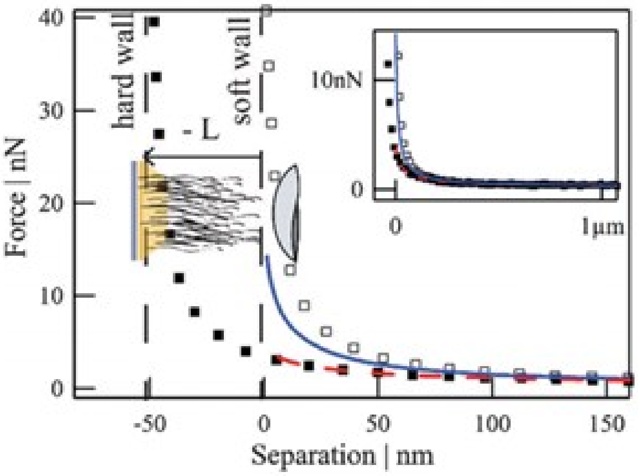

Figure C.4. Hydrodynamic drainage force (open squares) plotted as a function of separation for a silica microsphere (R ~ 10 µm) approaching a thick, end grafted PEG polymer brush. The black squares represent the same data if shifted by the equilibrium brush thickness (50 nm). The solid (blue) line represents the no slip model and the dashed (red) line represents the slip model fitted to the shifted force curve, with a slip length. The inset shows the same force curves and model predictions at larger separations. Figure reprinted from [41] with permission.

A dependence on approach velocity has also been observed in the hydrodynamic interactions of other poroelastic systems. For example, using a novel colloidal probe AFM method with a direct magnetic drive to remove cantilever drag effects, Nalam et al. demonstrated that the load dependence of the storage stiffness of polyacrylamide hydrogels transitioned from Hertzian to a dynamic punch-type model at higher frequencies.[42] This change in the contact mechanical behavior of the hydrogels was attributed to a contribution from solvent confinement or hydrogel poroelasticity, which was found to lead to a stiffening of the mechanical response of the gels.

C.4. Current challenges

Development of new instrumentation and techniques In AFM studies, the absolute separation between the interacting surfaces and associated deformation can typically only be obtained indirectly through theoretical modeling. In recent years a number of efforts have been made to integrate the measurement of the interaction force of deformable surfaces with simultaneous spatial-temporal visualization. For example, Tabor et al.[21] combined AFM and laser scanning confocal microscopy to analyze the interactions between fluorinated oil droplets in water. Other groups also combined AFM with reflection interference contrast microscopy (RICM). For instance, Shi et al. measured the interactions between an air bubble and solid surface of different hydrophobicites.[43] However, Erath et al.[44] used this approach to study the quasi-static adhesive-elastic interactions between solids, dynamic AFM-RICM measurements involving soft solid surfaces have yet to be performed.

Different versions of the SFA have also similarly been modified to enable simultaneous optical[39] and fluorescence[45] imaging of the contact area during surface force measurements. In particular, such in-line visualization has been demonstrated to provide valuable additional insight into the adhesion mechanisms of viscoelastic thin films.[39]

Other modifications to the SFA have also been implemented by Charlaix and coworkers to allow the measurement of the relative displacement of the surfaces with a capacitance sensor, hence allowing for surface deformation to be uncoupled from the force spring bending. [3,33,46] However, this technique does not allow for direct characterization of the contact shape. On the other hand, our own group has had success with using interferometry to directly monitor the elastohydrodynamic deformation of elastic films, but have had to rely on theoretical models to estimate far-field deformations in the calculations of forces.[14]

In addition to AFM and SFA, many lab-built microtribometers have been developed in the last ten years that combine force measurements with in situ imaging and/or in line laser techniques. These have been used to study the adhesive contact geometries[47] or role of surface deformation in the friction of compliant surfaces.[48] However, we are not aware that any such instruments have been employed for dynamic force measurements in fluid environments. In other experimental set-ups, the embedding of fluorescent particles combined with laser profilometry (Figure 5b) has been recently demonstrated to be a useful method to capture the in situ deformation of an elastic thin films in oil.[49] However, in this form of imaging the spatial resolution of deformation is limited. On the other hand, it has been demonstrated that physical and chemical methods, such as quick quenching with liquid nitrogen and UV cross-linking, can provide a means to capture transient surface patterns and instabilities in viscoelastic thin films for ex situ image analysis.[39]

Viscoelasticity. The majority of existing studies and theoretical models have focused on accounting for the deformation of elastic contacts. However, many soft materials are inherently viscoelastic. A number of recent studies demonstrated the need to consider the role of viscoelasticity of the interacting materials in the theoretical treatment, and to characterize the role of viscoelasticity on adhesion and contact dynamics. For example, For example, in a recent theoretical study, Pandey et al. presented how the viscoelasticity of a soft wall lifted the sliding of a lubricated sphere (Figure 5a).[50] Ffor microstructured epoxy surfaces, results from Castellanos et al. have demonstrated that viscoelasticity can determine the adhesion properties of structured surfaces more than their bulk elasticity (Young's modulus).[51] While otherOther investigations for smooth surfaces, such as by Zeng et al., have shown existing contact mechanical models to fail for viscous liquids and viscoelastic thin films.[39] Similarly, Nalam et al. observed the Hertzian model to be limited to low frequencies and strains in dynamic modulation measurements on hydrogel networks, further demonstrating the complex and dissipative nature of viscoelastic materials.[42] Analogously, in our own analysis, we also showed that the spatiotemporal deformation of an elastic film for elastic layers in viscous fluid can be best described by treating the elastic film as a viscoelastic material.[14]

Soft coatings and finite thickness films. Another complication to EHD, which has been addressed by very limited number studies, is that of layered or stratified materials. Nano-rheological techniques have been shown to be promising to probe the dynamic responses of viscoelastic properties of materials by separating the viscous and elastic contributions to their overall mechanical behaviors. Using this type of approach, Leroy et al. extracted the absolute modulus of an elastic soft layer, in both limits of a thin and thick film, by applying a finite thickness elastic model.[3] Such observations are also supported by our results, which showed that the finite thickness of the elastic film gradually alters the deformation profile from that of a semi-infinite compliant material during the drainage measurements in a viscous oil.[14]

Compared to an elastic half-space, an elastic layer of finite thickness on a rigid substrate would be more general and relevant to applications such as nano-scale devices and thin film coatings. For the case of contact mechanics McGuiggan et al. provided a full numerical solution for indentation (contact) of multilayer system. To verify their model they compared their numerical results to the contact radii and forces measured for the same system using an SFA.[52] In the case of EHD, the fluid pressure distribution is not the same as in contact mechanics. Therefore, corrections based on a contact mechanics treatment cannot be applied for EHD of stratified materials.[14] Modeling general elasticity solutions in 3D systems is mathematically complex and analytical solutions for only a few simple geometries are attainable. Instead, a more basic approach one can take is to consider only a 2D geometry, for example in axisymmetrical situations. This theoretical analysis has been previously employed by Balmforth et al. who studied the sedimentation of objects under gravity toward a layered elastic system.[53] By solving this EHD problem they compared the different contact profiles for a few limiting cases: as a foundation (thin compressible layer on rigid base), half-space, beam and membrane, for varying thicknesses of the elastic layer. In these 2D limits of very thin films they predicted how the asymptotic scaling of a central and barrier rim fluid gap thickness changes.

Path-dependent deformation. The dissipative nature of fluid drainage processes leads to surface deformation and fluid flow during EHD that depends on the history of the surface motion. Such path-dependent deformation profiles were demonstrated by Clasohlm et al., who investigated the sudden approach of a solid wall towards a liquid drop from close proximity.[18] Using a modified SFA to monitor the contact geometry and absolute surface separation, they showed that unusual shapes of the mercury drops could occur depending on the approach conditions. In particular, they observed the formation of a wimple en route to an eventual dimple, which was not observed for approaches from large initial separations. It can be anticipated that such path dependent flow and contact geometries would also occur for a soft solid. However, to the best of our knowledge, no previous study has yet to discuss this possibility in detail.

Slip. In general, the no-slip boundary condition has been used to describe the fluid flow at wetting interfaces. However, the validity of available corrections to the no-slip boundary condition have yet to be investigated systematically for deformable surfaces. Furthermore, the incorporation of slip corrections to a deformable surface is not straightforward.[54] For a polymer brush layer, Charrault et al. demonstrated that the hydrodynamic drainage of a fluid squeezed between a sphere and a thick brush could be well described by the invoking a slip length, if the surface separation was corrected for a non-deformed zero position (Figure 4).[41] However, for a large approach velocity they observed a notable deviation from the separation-corrected slip model which they attributed to prior contact elastic deformation of polymer brushes due to the larger magnitude of the repulsive hydrodynamic force at a high velocity.

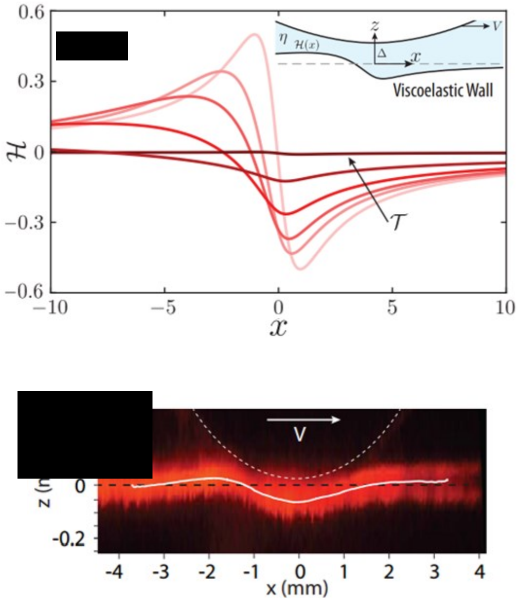

Figure C.5. (a) Theoretical prediction for the deformation of a viscoelastic wall during the sliding of a standard linear solid half space (shown in inset) for various characteristic time scale T, where T = 0 signifies a purely elastic wall. Figure reprinted from [50](b) Laser profilometry image showing the deformation of the elastic thin film with fluorescent particles embedded during sliding of a negatively-buoyant rigid cylinder immersed in a viscous oil bath on a tilted elastic wall. Figure reprinted from [49] with permission.

Heterogeneous (porous) materials. Difficulties in modelling EHD are also met when dealing with heterogeneous surfaces, such as porous or structured surfaces. For example, in a recent theoretical study Pandey et al. presented how the viscoelasticity of a soft wall lifted the sliding of a lubricated sphere (Figure 5a).[50] It is also possible that compliant materials can be poroelastic. In general that case the EHD models, as described in the previous section, must be greatly modified to account for material poroelasticity as the boundary condition on a porous interface is more complex and needs to be carefully considered to describe the coupling between the deformation of solid skeleton and flow of permeating fluid which do not exist in purely elastic solids.[2] The hydrodynamics of poroelastic ordered and disordered microstructures have been studied by Gopinath et al.[55]. Instead of using traditional Brinkman approximations for porous media, they demonstrated that to fully consider the flow through pores a modified boundary condition must be invoked, adding further complexity.

C.5 Conclusions

We have reviewed a number of important experimental and theoretical studies which have investigated the effects of surface deformation on hydrodynamic forces. By and large, previous experimental studies have been performed using AFM or SFA. However, typically these techniques need to rely on numerical models to access information about the deformation profile or geometry. To facilitate the direct visualization of surface deformation with force measurements a number of new techniques are emerging, for example RICM[43] and laser profilometry. [49]

For rigid surfaces, hydrodynamic interactions in a low Reynolds number Newtonian fluid have been well described by Reynolds equation in the lubrication limit. Conversely, in the case of soft surfaces the deformation of the interface will alter the hydrodynamic interactions. For elastic surfaces, the linear elasticity model provides simple forms of deformation for a half-space and needs to be coupled with the lubrication equation. [28] However, due to finite thickness effects, the deformation for layered materials is more complex and needs to be studied further.

In addition, we discussed more complicated scenarios where the material poroelasticity, viscoelasticity or physical or chemical heterogeneities, such as slip, need to be considered. These effects are particularly important in understanding the role of hydrodynamic forces in biological systems, for instance in wet bio-adhesion. A better understanding in EHD can be anticipated to aid the future development of biomedical implants, such as artificial organs or tubing[7], as well as microfluidic sensors and devices. Furthermore, elastohydrodynamic interactions may provide an additional avenue to fabricate complex 3D structures, such as self-folded structures from 2D planar surfaces and allow more precise control of capillary interactions in micro-electromechanical systems (MEMS). Together, these broader aspects of applications provide a strong motivation for the future study of hydrodynamic interactions in the presence of deformable surfaces.

References

1. Lugt P, Morales-Espejel GE: A review of elasto-hydrodynamic lubrication theory. Tribology Transactions (2011) 54(3):470-496.

2. Skotheim JM, Mahadevan L: Soft lubrication: The elastohydrodynamics of nonconforming and conforming contacts. Physics of Fluids (2005) 17(9):092101.

3. Leroy S, Charlaix E: Hydrodynamic interactions for the measurement of thin film elastic properties. J Fluid Mech (2011) 674(389-407).

4. Snoeijer J, Eggers J, Venner C: Similarity theory of lubricated hertzian contacts. Physics of Fluids (1994-present) (2013) 25(10):101705.

5. Urzay J: Asymptotic theory of the elastohydrodynamic adhesion and gliding motion of a solid particle over soft and sticky substrates at low reynolds numbers. J Fluid Mech (2010) 653(391-429.

6. Vlassopoulos D, Cloitre M: Tunable rheology of dense soft deformable colloids. Current Opinion in Colloid & Interface Science (2014) 19(6):561-574.

7. Jin Z, Dowson D: Elastohydrodynamic lubrication in biological systems. Proceedings of the Institution of Mechanical Engineers, Part J: Journal of Engineering Tribology (2005) 219(5):367-380.

8. Dirks J-H, Federle W: Fluid-based adhesion in insects–principles and challenges. Soft Matter (2011) 7(23):11047-11053.

9. Espinosa-Marzal RM, Bielecki RM, Spencer ND: Understanding the role of viscous solvent confinement in the tribological behavior of polymer brushes: A bioinspired approach. Soft Matter (2013) 9(44):10572-10585.

10. Greene GW, Banquy X, Lee DW, Lowrey DD, Yu J, Israelachvili JN: Adaptive mechanically controlled lubrication mechanism found in articular joints. Proceedings of the National Academy of Sciences (2011) 108(13):5255-5259.

11. Roberts A: Squeeze films between rubber and glass. Journal of Physics D: Applied Physics (1971) 4(3):423.

12. Dagastine RR, Manica R, Carnie SL, Chan D, Stevens GW, Grieser F: Dynamic forces between two deformable oil droplets in water. Science (2006) 313(5784):210-213.

13. Kaveh F, Ally J, Kappl M, Butt H-Jr: Hydrodynamic force between a sphere and a soft, elastic surface. Langmuir (2014) 30(39):11619-11624.

14. Wang Y, Dhong C, Frechette J: Out-of-contact elastohydrodynamic deformation due to lubrication forces. Physical review letters (2015) 115(24):248302.

15. Leroy S, Steinberger A, Cottin-Bizonne C, Restagno F, Leger L, Charlaix E: Hydrodynamic interaction between a spherical particle and an elastic surface: A gentle probe for soft thin films. Physical review letters (2012) 108(26):264501.

16. Chan DY, Klaseboer E, Manica R: Film drainage and coalescence between deformable drops and bubbles. Soft Matter (2011) 7(6):2235-2264.

17. Manica R, Connor JN, Carnie SL, Horn RG, Chan DY: Dynamics of interactions involving deformable drops: Hydrodynamic dimpling under attractive and repulsive electrical double layer interactions. Langmuir (2007) 23(2):626-637.

18. Clasohm LY, Connor JN, Vinogradova OI, Horn RG: The "wimple": Rippled deformation of a fluid drop caused by hydrodynamic and surface forces during thin film drainage. Langmuir (2005) 21(18):8243-8249.

19. Dagastine RR, Webber GB, Manica R, Stevens GW, Grieser F, Chan DYC: Viscosity effects on hydrodynamic drainage force measurements involving deformable bodies. Langmuir (2010) 26(14):11921-11927.

20. Chan DY, Klaseboer E, Manica R: Dynamic deformations and forces in soft matter. Soft Matter (2009) 5(15):2858-2861.

21. Tabor RF, Lockie H, Mair D, Manica R, Chan DY, Grieser F, Dagastine RR: Combined afm− confocal microscopy of oil droplets: Absolute separations and forces in nanofilms. The Journal of Physical Chemistry Letters (2011) 2(9):961-965.

22. Keh M, Leal L: Adhesion and detachment of a capsule in axisymmetric flow. Physical Review Fluids (2016) 1(1):013201.

23. Pellet C, Cloitre M: The glass and jamming transitions of soft polyelectrolyte microgel suspensions. Soft matter (2016) 12(16):3710-3720.

24. Villey R, Martinot E, Cottin-Bizonne C, Phaner-Goutorbe M, Léger L, Restagno F, Charlaix E: Effect of surface elasticity on the rheology of nanometric liquids. Physical Review Letters (2013) 111(21):215701.

25. Chan DY, Horn R: The drainage of thin liquid films between solid surfaces. The Journal of chemical physics (1985) 83(10):5311-5324.

26. Reynolds O: On the theory of lubrication and its application to mr. Beauchamp tower's experiments, including an experimental determination of the viscosity of olive oil. Proceedings of the Royal Society of London (1886) 40(242-245):191-203.

27. Temizer İ, Stupkiewicz S: Formulation of the reynolds equation on a time-dependent lubrication surface. 472:Abs 20160032.

28. Davis RH, Serayssol J-M, Hinch E: The elastohydrodynamic collision of two spheres. J Fluid Mech (1986) 163(479-497).

29. Hertz H: Über die berührung fester elastischer körper. Journal für die reine und angewandte Mathematik (1882) 92(156-171).

30. Lian G, Adams M, Thornton C: Elastohydrodynamic collisions of solid spheres. J Fluid Mech (1996) 311(141-152).

31. Sneddon IN: Fourier transforms. Courier Corporation, (1995).

32. Aston DE, Berg JC: Thin-film hydrodynamics in fluid interface-atomic force microscopy. Industrial & Engineering Chemistry Research (2002) 41(3):389-396.

33. Steinberger A, Cottin-Bizonne C, Kleimann P, Charlaix E: Nanoscale flow on a bubble mattress: Effect of surface elasticity. Physical Review Letters (2008) 100(13):134501.

34. Horn RG, Bachmann D, Connor J, Miklavcic S: The effect of surface and hydrodynamic forces on the shape of a fluid drop approaching a solid surface. Journal of physics: condensed matter (1996) 8(47):9483

35. Horn RG, Asadullah M, Connor JN: Thin film drainage: Hydrodynamic and disjoining pressures determined from experimental measurements of the shape of a fluid drop approaching a solid wall. Langmuir (2006) 22(6):2610-2619.

36. Wexler JS, Heard TM, Stone HA: Capillary bridges between soft substrates. Physical review letters (2014) 112(6):066102.

37. Gondret P, Lance M, Petit L: Bouncing motion of spherical particles in fluids. Physics of Fluids (1994-present) (2002) 14(2):643-652.

38. Joseph G, Zenit R, Hunt M, Rosenwinkel A: Particle–wall collisions in a viscous fluid. J Fluid Mech (2001) 433(329-346).

39. Zeng H, Zhao B, Tian Y, Tirrell M, Leal LG, Israelachvili JN: Transient surface patterns during adhesion and coalescence of thin liquid films. Soft Matter (2007) 3(1):88-93.

40. Macirowski T, Tepic S, Mann RW: Cartilage stresses in the human hip joint. Journal of biomechanical engineering (1994) 116(1):10-18.

41. Charrault E, Lee T, Easton CD, Neto C: Boundary flow on end-grafted peg brushes. Soft Matter (2016).

42. Nalam PC, Gosvami NN, Caporizzo MA, Composto RJ, Carpick RW: Nano-rheology of hydrogels using direct drive force modulation atomic force microscopy. Soft Matter (2015) 11(41):8165-8178.

43. Shi C, Cui X, Xie L, Liu Q, Chan DY, Israelachvili JN, Zeng H: Measuring forces and spatiotemporal evolution of thin water films between an air bubble and solid surfaces of different hydrophobicity. ACS Nano (2014) 9(1):95-104.

44. Erath J, Schmidt S, Fery A: Characterization of adhesion phenomena and contact of surfaces by soft colloidal probe afm. Soft Matter (2010) 6(7):1432-1437.

45. Lee DW, Kristiansen K, Donaldson Jr SH, Cadirov N, Banquy X, Israelachvili JN: Real-time intermembrane force measurements and imaging of lipid domain morphology during hemifusion. Nature communications (2015) 6(

46. Restagno F, Crassous J, Charlaix E, Monchanin M: A new capacitive sensor for displacement measurement in a surface-force apparatus. Measurement Science and Technology (2001) 12(1):16.

47. Krick BA, Vail JR, Persson BN, Sawyer WG: Optical in situ micro tribometer for analysis of real contact area for contact mechanics, adhesion, and sliding experiments. Tribology letters (2012) 45(1):185-194.

48. Piccardo M, Chateauminois A, Fretigny C, Pugno NM, Sitti M: Contact compliance effects in the frictional response of bioinspired fibrillar adhesives. Journal of The Royal Society Interface (2013) 10(83):20130182.

49. Baudouin Saintyves TJ, Thomas Salez, and L. Mahadevan: Self-sustained lift and low friction via soft lubrication. Proceedings of the National Academy of Sciences (2016) 113(21):5847-5849.

50. Pandey A, Karpitschka S, Venner K, Snoeijer J: Lubrication of soft viscoelastic solids. arXiv preprint arXiv:151206156 (2015).

51. Castellanos G, Arzt E, Kamperman M: Effect of viscoelasticity on adhesion of bioinspired micropatterned epoxy surfaces. Langmuir (2011) 27(12):7752-7759.

52. McGuiggan P, Wallace J, Smith D, Sridhar I, Zheng Z, Johnson K: Contact mechanics of layered elastic materials: Experiment and theory. Journal of Physics D: Applied Physics (2007) 40(19):5984.

53. Balmforth N, Cawthorn C, Craster R: Contact in a viscous fluid. Part 2. A compressible fluid and an elastic solid. J Fluid Mech (2010) 646(339-361).

54. Pilkington GA, Gupta R, Fréchette J: Scaling hydrodynamic boundary conditions of microstructured surfaces in the thin channel limit. Langmuir (2016) 32(10):2360-2368.

55. Gopinath A, Mahadevan L: Elastohydrodynamics of wet bristles, carpets and brushes.Abs rspa20100228.

Curriculum Vitae

Charles Dhong was born on January 26th in Mount Kisco, New York and grew up in Austin, Texas. He received his bachelors of science in Chemical and Biomoecular Engineering in 2012 from the University of California, Berkeley. During his time there, Charles worked on several research projects which included using diblock copolymers to template gold nanoparticles, developing novel screening assays for directed evolution in salmonella, smoking cessation and tracking sources of N_2O through isotopic tracing. He worked as an intern for the Alliance to Save Energy's Green Campus program (now PowerSave) to help reduce energy consumption on campus and also served in student government on campus. After graduation, Charles joined the lab of Professor Joelle Frechette as a graduate research assistant in the Department of Chemical and Biomoecular Engineering at the Johns Hopkins University. His research interests include the response of deformable and patterned materials to viscous forces.